博士論文

Generation and application of plasma-ice interfacial reaction field

（プラズマ／氷界面反応場の創製と応用）

榊原 教貴

CONTENTS

List of Figures

List of Tables

Chapter.1 Introduction

Plasma is an ionized gas abundant with charged particles and reactive species. Plasma plays a significantly key role in our lives. In industries, plasma provides fundamental and indispensable technologies that form the basis of the industry, such as fabrication of semiconductor devices [1, 2]. At the same time, in our nature, plasma influences on various phenomena on Earth and in the universe, such as lighting [3, 4], ionosphere [5], and solar wind [6].

Looking back on the history of the development of plasma science and technology, new types of plasma sources have been leading and established various innovative applications. Traditionally, by using low-pressure low-temperature plasmas, plasma science and technology has been established in a clean gas phase with high uniformity, such as in semiconductor manufacturing process [1, 2]. Recently, however, the emergence of non-equilibrium plasma sources under high-density environments, including room temperature and atmospheric pressure condition [7], has been realizing new areas of plasma processes, because it enables the introduction of condensed phases such as solid, liquid, and supercritical fluid into plasma processes [8, 9] without changing their state of matter by overheating. In particular, the development of plasma processes with liquid phase is remarkable, where the introduction of liquid phase provides unique liquid phase reaction field activated by plasma. This is opening various new and innovative applications for materials design and processing, environmental technologies, agriculture, and bio-medicals [8].

In general, gas temperature in plasma reaches several hundreds to thousands Kelvin (K) because much energy is necessary for ionization. However, our group has developed a novel plasma source called cryoplasma [10-13]. Cryoplasma is a non-equilibrium plasma source whose gas temperature can be controlled continuously at wide range of cryogenic temperatures lower than room temperature, by limiting the spatial (< 1 mm) and temporal (< 100 ns electrical or optical excitation) scales of the plasma. The most important property of cryoplasma is its temperature controllability at cryogenic conditions, which potentially extends the current applications of non-equilibrium plasma to wider range of applications.

In cryogenic environments, ice is one of the most universal solid components, which is a solid state of low molecular weight materials such as water. Ice provides a fascinating interfacial reaction field in terms of both science and engineering. For example, the ice surface reaction has a significant impact on the formation of active chlorine species, which is involved in the depletion of the ozone layer, because it is dominated by the adsorption of reactive species from gas phase [14]. On the other hand, many kinds of designs of biomimetic structural materials have been reported by using self-assembling structures associated with freezing phenomena [15]. Here, by focusing on ice surface as a reaction field unique to low and cryogenic temperature environment, and combining cryoplasma with ice surface, further development of plasma science and processes can be anticipated. However, there has been no research on plasma-ice interface as a reaction field, as far as I know.

In this dissertation, I have studied the generation and application of plasma-ice interfacial reaction field, for the purpose of creating a novel cryogenic reaction field with cryoplasma and opening a frontier research

area of plasma science and technology.

This dissertation is composed of five chapters. Background and purpose of this thesis are noted in chapter 1. In chapter 2, laser diagnostics of cryoplasma is demonstrated for evaluating gas temperature and investigating gas temperature dependence of chemical reactions in cryoplasma, prior to the generation and application of plasma-ice interfacial reaction field. Generation of plasma-ice interfacial reaction field with a good temperature control was established in chapter 3. Two applications of plasma-ice interfacial reaction field were studied in this dissertation, from science and engineering viewpoint, respectively. In chapter 4, as a scientific application, materials process in cryogenic astrophysical environment was simulated, and cryogenic-specific phenomenon which has never been reported before was discovered. In chapter 5, as an engineering application, a new method for thin film synthesis was developed by combining cryoplasma with freezing phenomenon. Finally, in chapter 6, this dissertation is summarized and concluded.

1-1. Cryoplasma

For the generation of plasma-ice interfacial reaction field, plasma that possesses lower gas temperature than the melting point of water is indispensable. Here, as one of such plasma, cryoplasma is overviewed.

1-1-1. What is cryoplasma

Cryoplasma represents a class of non-equilibrium plasma, which can control gas temperature (T_g) continuously below room temperature. Our group has developed cryoplasma for processing plasma source for the first time in the world [10–13] in the third gas temperature range below room temperature, which continues to the conventional temperature range of thermal plasma ($T_g \approx$ several thousands–millions K) and low-temperature plasma ($T_g \approx$ several hundreds–thousands K), as presented in Fig. 1.1. In general, in non-equilibrium plasma, electron temperature (T_e) is much higher than gas temperature, and electron temperature is thought to govern chemical reactions in plasma [16]. Therefore, in most studies only electron temperature has been regarded as a crucial parameter in the research area of non-equilibrium plasma. However, especially in high-density media including atmospheric pressure, gas temperature governs total enthalpy of the system, and might be considered to have an important influence on chemical reactions [17–19] in addition to electron temperature. In the research of cryoplasma, we focus on gas temperature as a crucial control parameter, and extended gas temperature range to cryogenic temperatures where the gas temperature can be changed in up to 2 order. Cryoplasma has been revealed to exhibit unique characteristics and dynamic variations depending on gas temperature, such as the formation of self-organization patterns [20, 21]. Moreover, from an engineering point of view, cryoplasma is a promising plasma source for cryogenic applications with low damage such as biomedicine [22, 23] and semiconductor fabrication [24]. For example, it has been demonstrated that cryoplasma can be used for photoresist removal with keeping the damage levels being lower than conventional ashing processes [25, 26].

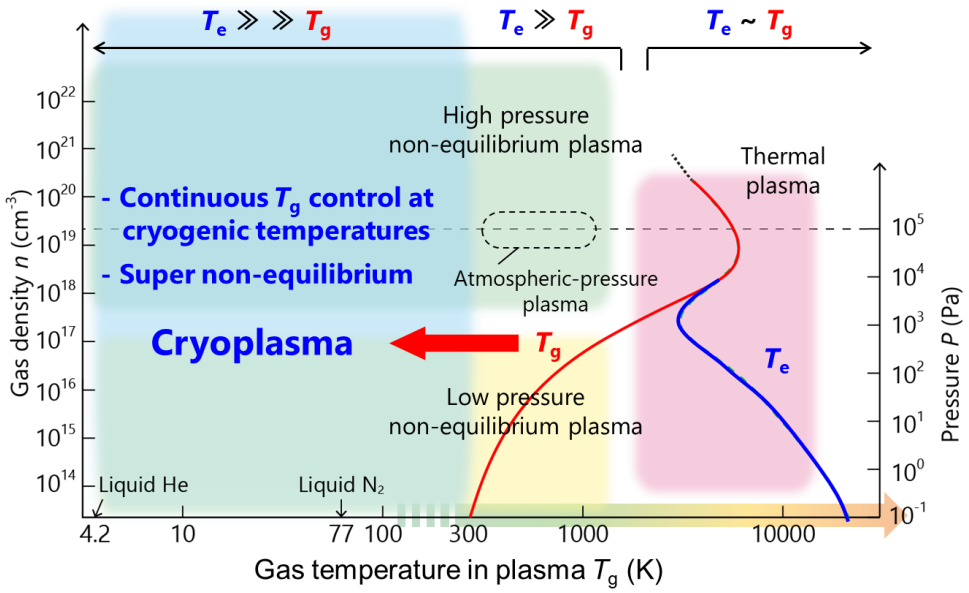

Figure 1.1 Cryoplasma, in the third range of gas temperature. Adopted from [10] with the permission of Institute of Physics Publishing.

1-1-2. Generation of cryoplasma

For the generation of cryoplasma, suppression of heating is indispensable because gas temperature has to be kept below room temperature. Especially at high pressure including atmospheric pressure, gas temperature is easy to increase due to the higher collision frequency between electrons and neutral species than at low pressure. To suppress the heating of plasma, there are mainly three strategies. One is temporal restriction of energy input, and the second is miniaturization of the size of plasma, and the last is the usage of thermally conductive carrier gas.

Temporal restriction of energy input is available with pulsed power supply. Dielectric barrier discharge (DBD) is often utilized, where dielectric barriers are inserted between electrodes. In DBD, accumulation of charge on a dielectric barrier cancels out the external electric field, resulting in the stop of discharges (Fig. 1.2(a), (b)). In this way, DBD spontaneously generates nanosecond pulsed discharges, which leads to temporal confinement of energy input. Therefore, DBD is one of the suitable methods to generate

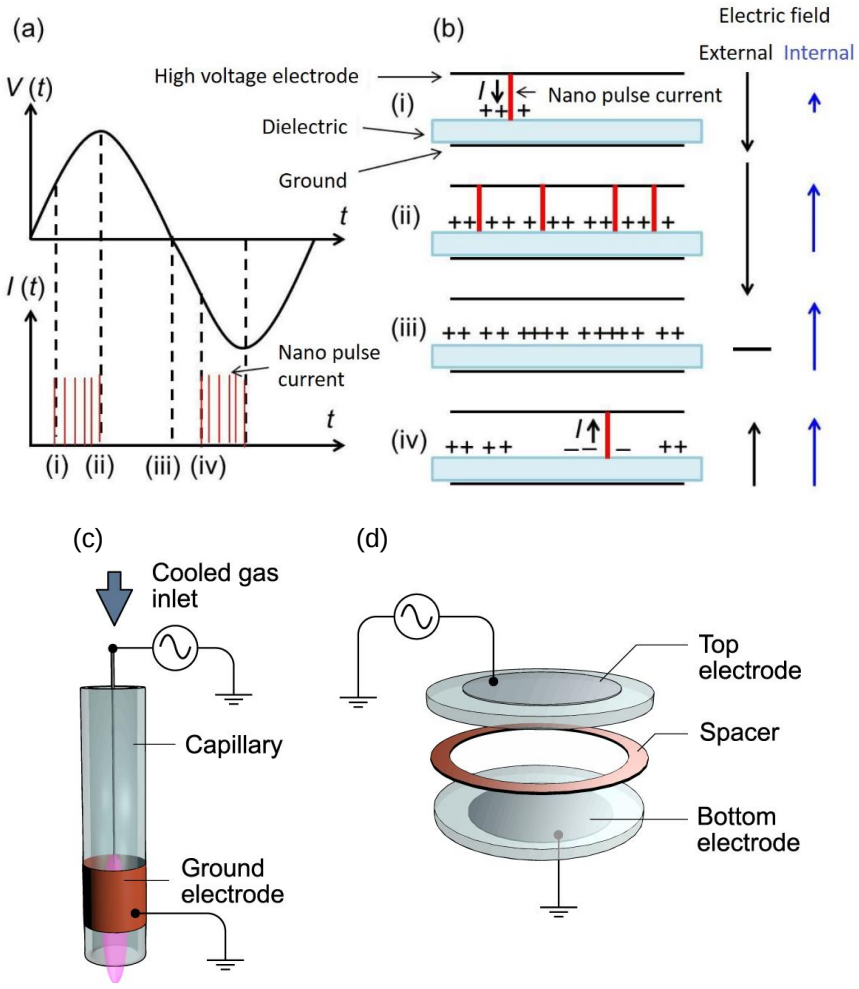

Figure 1.2 (a) Typical example of *I-V* characteristics of DBD, and (b) the schematic of discharge mechanism of DBD. Accumulation of charges on dielectric barrier forms internal electric field, which causes weakened external electric field and lead to the instantaneous disappearance of discharges. (c), (d) typical configurations for generating cryoplasma in this dissertation, jet type and coplanar type, respectively. Adopted from [10] with the permission of Institute of Physics Publishing.

cryoplasma. In Fig. 1.2, typical schematics of DBD configuration for the generation of cryoplasma are illustrated. One is jet type (Fig. 1.2(c)) and the other is coplanar type (Fig. 1.2(d)), which can be selected according to the purpose and application.

Miniaturization of the size of plasma makes microplasma, which is plasma spatially confined to the dimensions of 1 mm or less. Microplasma has large specific surface area owing to its small size. This leads to easy heat dissipation from plasma. Therefore, microplasma can prevent the heating when the gas density of the plasma is kept, which is advantageous for the generation of cryoplasma.

For better heat management of plasma, carrier gas is also significant. By using carrier gas with high thermal conductivity for the generation of plasma, such as helium gas (thermal conductivity is ~10 times higher than air), heat exchanged between plasma and ambient environment can be promoted. This is also advantageous for the heat control of plasma.

Based on these strategies, cryoplasma is generated by using a plasma cell equipped with a cooling system. As shown in Fig. 1.3, our group has developed two types of plasma cells: one is cooed by liquid nitrogen (Fig. 1.3(a), (b)), and the other is cooled by liquid helium (Fig. 1.3(c), (d)). The former allows temperature access to the liquid nitrogen temperature (77 K at 1 atm). This plasma cell was used in chapter

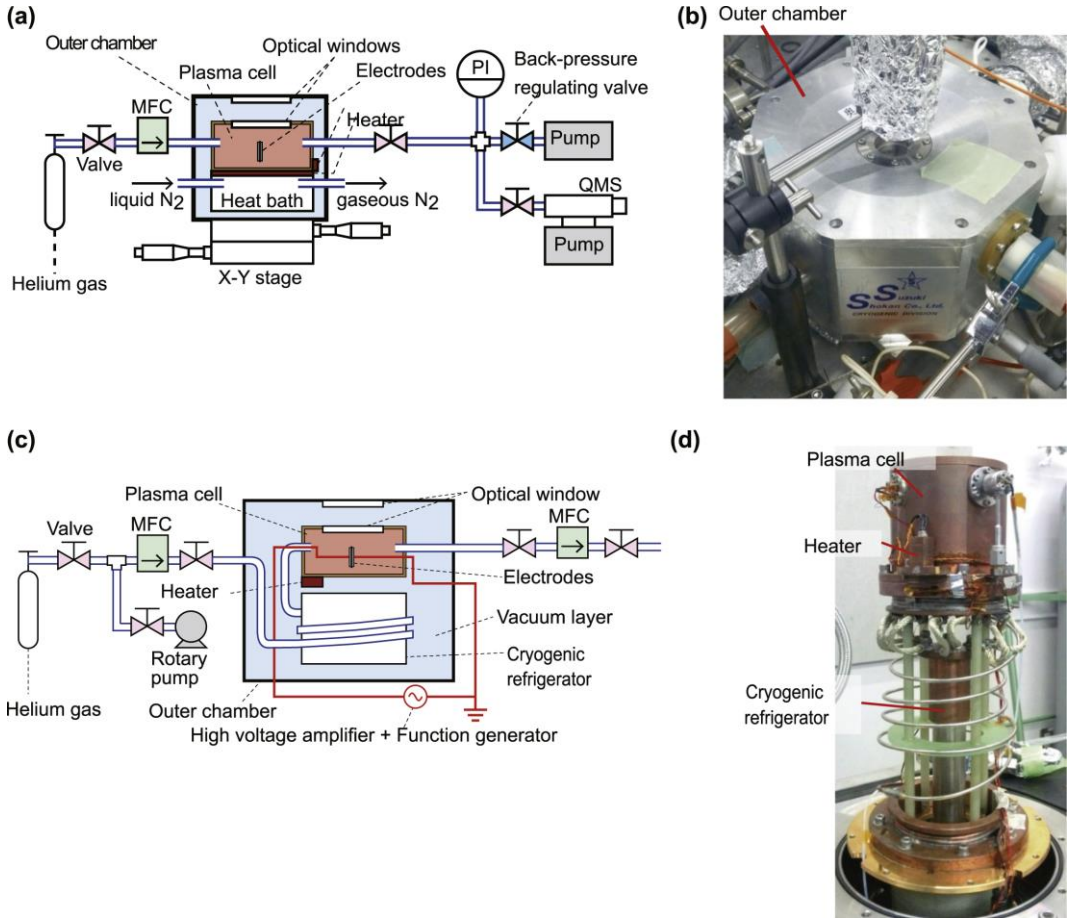

Figure 1.3 Schematic illustrations and photographs of plasma cells equipped with a cooling system for generating cryoplasma. (a), (b) a plasma cell cooled by liquid nitrogen. (c), (d) a plasma cell equipped with a cryostat by liquid helium. Adopted from [10] with the permission of Institute of Physics Publishing.

2. The latter consists of a cryostat, which often used in experiments of solid state physics. This plasma cell allows access to the liquid helium temperature (4.2 K at 1 atm) below room temperature, which was used in chapter 3 and chapter 4. Cryoplasma can be generated inside these plasma cells, with a continuous and precise control of gas temperature in plasma.

1-1-3. Gas temperature dependence of cryoplasma

In the previous researches of cryoplasma, various fundamental characteristics of cryoplasma depending on gas temperature have been revealed. In Fig. 1.4, variation of discharge mode of cryo-DBD in helium is shown according to gas temperature [27]. At 270 K, the discharge current was too weak for the discharge mode to be distinguished. This could be pseudoglow, Townsend or small filamentary mode, which is considered to be excited by direct ionization of helium atoms [28]. When decreasing gas temperature, the discharge mode changed to glow mode at 225 K, and was Townsend mode below 180 K.

Optical emissions have also been revealed to exhibit gas temperature dependence, as shown in the image of Fig. 1.4 [27] and in Fig. 1.5 [13]. The color of emissions changed from red to purple with decreasing gas temperature, corresponding to the increase in emissions of N_2^+ (first negative system) and

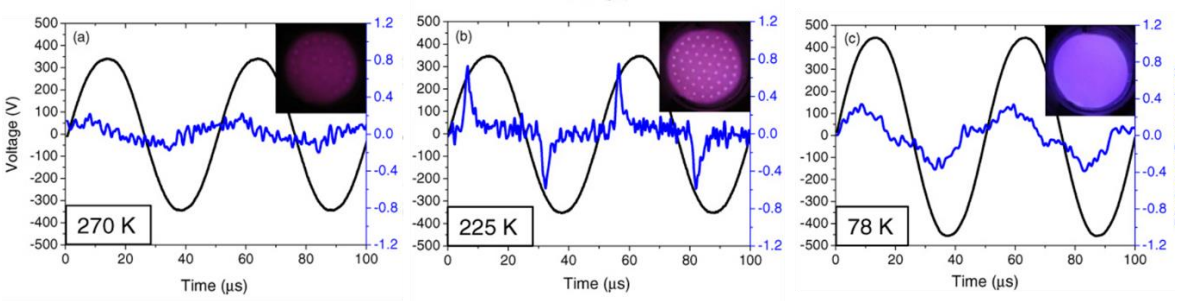

Figure 1.5 Variation of discharge mode of cryo-DBD in helium depending on gas temperature. Adopted from [27] with the permission of Institute of Physics Publishing.

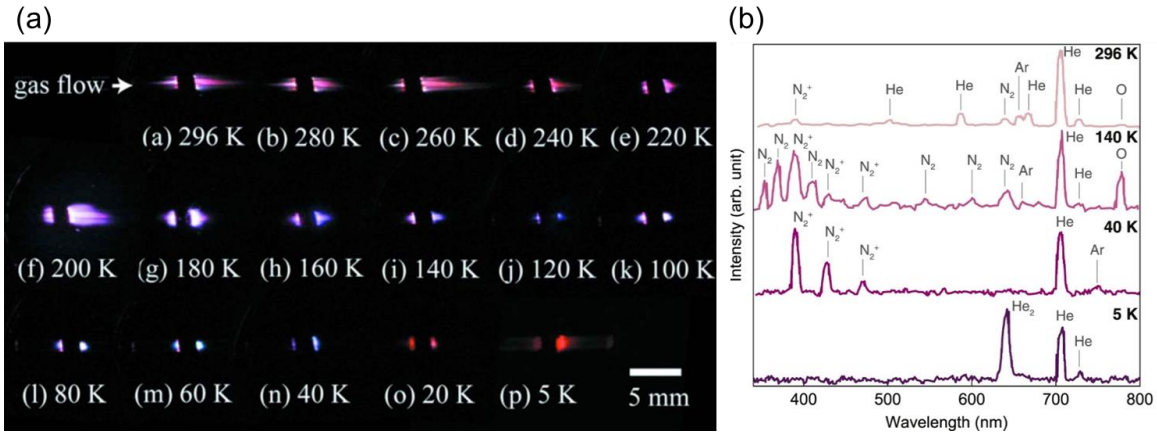

Figure 1.4 Images and optical emission spectra of helium cryoplasma jet generated in the plasma cell equipped with a liquid helium cryostat at gas temperatures between 296 and 5 K. Adopted from [13] with the permission of American Institute of Physics Publishing.

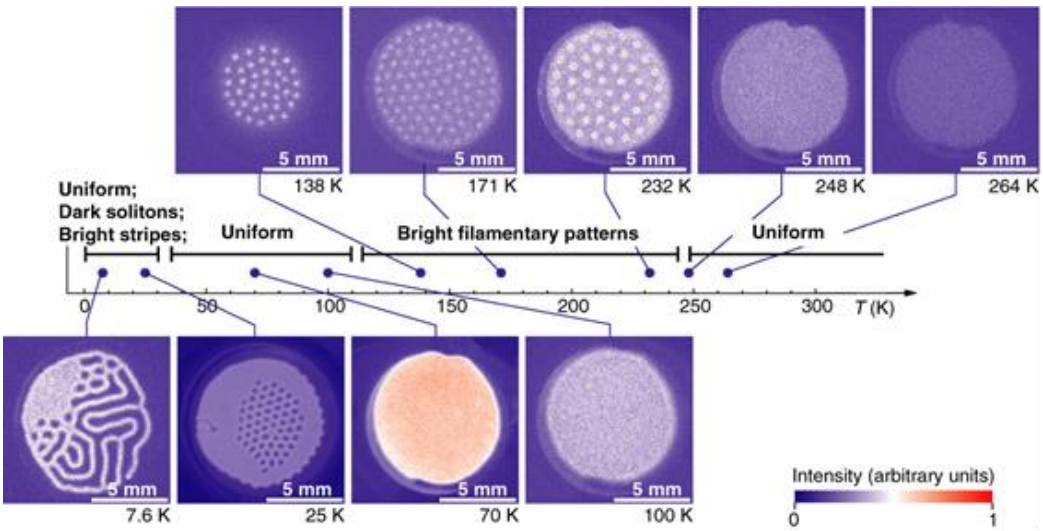

Figure 1.6 Formation of self-organized patterns depending on gas temperature. Adopted from [21] with the permission of Institute of Physics Publishing.

N_2 (second positive system). In general, helium metastable atoms in the 2^3S_1 level (He^m) generated by collision of electrons to helium atoms in helium discharges can diffuse independently of the applied electric field, and thus easily transfer their energy by collisions to impurity molecules such as N_2, as described in Eq. (1.1) and Eq. (1.2), which is referred to as Penning ionization.

$$He^m + N_2 \rightarrow N_2^+(B^2\Sigma_u^+) + He + e \qquad (1.1)$$

$$N_2^+(B^2\Sigma_u^+) \rightarrow N_2^+(X^2\Sigma_g^+) + hv \qquad (1.2)$$

Emissions of nitrogen ions are mainly attributed to Penning ionization. Here, metastable helium atoms play a key role in the chemical reactions in plasma. Increase in emissions of nitrogen ions below 220 K can be explained by the increase in the amount of helium metastable atoms due to longer lifetime of helium metastable atoms at lower temperature [29, 30]. Penning ionization induced by the abundant metastable helium atoms can prevent partial electron avalanches that induce filamentary discharge, and lead to the maintenance of a uniform glow discharge in Fig. 1.4 [27, 28]. When further decreasing the gas temperature below 180 K, ionization by two body collisions between metastable helium atoms (such as Eq. (1.3) and Eq. (1.4)) could become dominant due to further increase in metastable helium atoms.

$$He^m + He^m \rightarrow He^+ + He + e \qquad (1.3)$$

$$He^m + He^m \rightarrow He_2^+ + e \qquad (1.4)$$

This might cause the transition of discharge mode from glow mode to Townsend mode, which is shown in Fig. 1.4 [28].

On the other hand, when decreasing gas temperature below the melting and boiling point of nitrogen (T_b = 77 K, T_m = 63 K), N_2 becomes not to involve in reactions due to its absence by the lower sublimation pressure of N_2 at lower temperatures, and the appearance of He_2 emission is observed, as shown in Fig. 1.5. He_2^+ molecular ions can be formed by several reactions, for example, three body process as follows.

$$He^m + He + He \rightarrow He_2^+ + He + e \qquad (1.5)$$

In other words, super cryogenic temperature below boiling and melting points of nitrogen and other impurities provides further purified helium gas, which leads to the main excitation mechanism of helium

species without Penning ionization.

The formation of self-organized patterns has also investigated in helium cryoplasma [20, 21]. As shown in Fig. 1.6, cryoplasma formed self-organized patterns in according to gas temperature ranging from 264 to 7.6 K. This is attractive phenomenon in the research area of non-linear phenomena as well.

1-1-4. Advantage of cryoplasma

Cryoplasma holds promise for new plasma processing applications due to its advantages, mainly low gas temperature and controllability of gas temperature. Possible applications are the treatment of heat-sensitive materials or living cells in biomedical applications [22, 23] by using low heat damage of cryoplasma, and cryogenic semiconductor fabrication [24] by using controllability of gas temperature at cryogenic temperature. The extreme case of the heat-sensitive materials is a plasma processing to ice or frozen samples, which is thermodynamically stable below the melting point of the matter.

One example of the advantage of cryoplasma has been demonstrated in a plasma processing of nanoporous materials [25]. The reduction of gas temperature reduced the damage to the nanoporuos low-*k* materials during ashing process due to the suppressed penetration of oxygen radicals in nanoporous at lower temperature. Fig. 1.7 shows the distribution of the ration of carbon atoms to oxygen atoms and the density increase in nanoporous low-*k* substrates, which are monitored by scanning transmission electron microscope / electron energy loss spectroscopy (STEM/EELS) and X-ray refractivity (XRR), respectively. The low C/O and the large density increase mean the damage of low-*k* materials by oxygen plasma, and lower damage by oxygen plasma was accomplished at lower temperature. The confinement of radical species produced by plasma was mainly determined by the increase of sticking coefficient, recombination factors, and reaction factors. This means favoring of surface adsorption of radical species at lower gas temperatures.

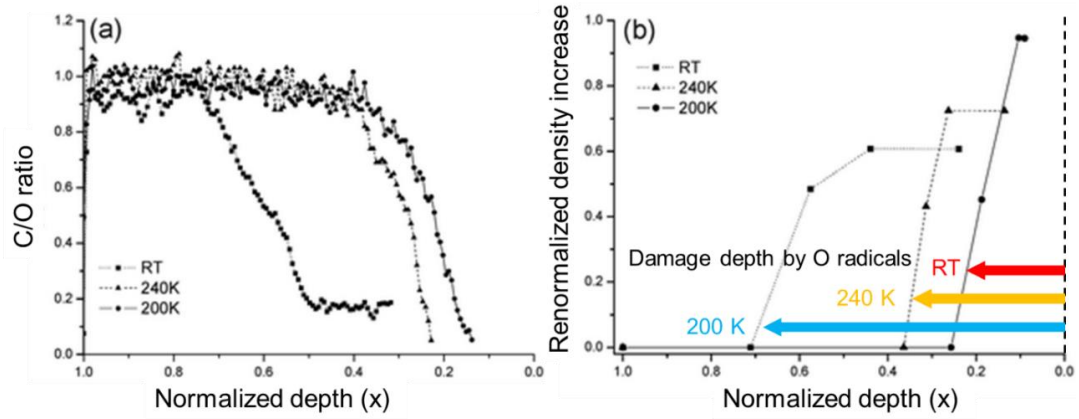

Figure 1.7 Distribution of (a) ratio of carbon atoms to oxygen atoms (C/O) and (b) density increase in the nanoporous low-*k* substrates treated by oxygen plasma [25]. The normalized depth represents the depth from the surface (dashed line at x=0) of the nanoporous low-*k* substrates. The damage depth by oxygen plasma at 200 K was one-third compared to that at room temperature (RT). Adopted from [25] with the permission of Royal Society of Chemistry.

1-1-5. Metastable atoms in plasma

Metastable atoms are atoms excited in a metastable level where optical transition to lower levels is forbidden or occurs only with very small probability. Metastable atoms have high internal energy up to 10 eV or more, and lose their internal energy only by collision with other species. For example, in the case of helium, helium atoms in the 2^3S_1 metastable level have 19.8 eV, as shown in Fig. 1.8. Therefore, metastable atoms generally involve in various ionization process and chemical reactions in plasma through collisions, as follows,

1. Cumulative ionization

$$X^m + e \rightarrow X^+ + e + e \qquad (1.6)$$

2. Penning ionization

$$X^m + Y \rightarrow X + Y^+ + e \qquad (1.7)$$

3. Two body collision

$$X^m + X^m \rightarrow X^+ + X + e \qquad (1.8)$$

where X and Y are gas atoms or molecules, X^m is X in a metastable level, and e is electron. Cumulative ionization can occur with lower energy electrons than the direct ionization, which results in easy generation and sustainment of plasma. Furthermore, other gas species and metastable atoms themselves can involve in ionization due to the high internal energy of metastable atoms, as described in Eq. (1.7) and Eq. (1.8). One example is the Penning ionization of He^m with N_2 molecules as shown in Eq. (1.1). In this way, metastable atoms play key roles in generation and sustainment of plasma.

1-1-6. Gas phase chemical reactions in cryoplasma

In recent years, gas temperature dependence of gas phase chemical reactions in helium cryoplasma has been investigated to understand further the gas temperature-dependent characteristics of cryoplasma. Two approaches have been conducted so far, investigation of time-dependent reaction dynamics with optical emission spectroscopy [29], and measurement of the density and lifetime of helium metastable atoms by laser absorption spectroscopy [30].

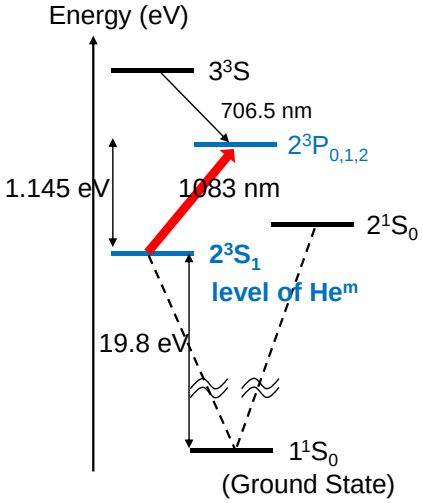

Figure 1.8 Energy levels of helium atoms, especially for metastable energy state.

In the time-resolved optical emission spectroscopy of cryoplasma at T_g = 28 K and 54 K, two time-dependent phenomena were observed as shown in Fig. 1.9. The first was a longer duration of the discharge current compared to that of helium emission at both gas temperatures, and the second was 8 μs delay of N_2^+ emission with respect to the emissions of atomic helium and helium dimers at 54 K. For the analysis of the phenomena, numerical simulation with 0-dimensional time-dependent global model was conducted, in which not only T_e but also T_g were taken into account. This analysis revealed that the both time-dependent phenomena can be explained by the long lifetime of metastable helium atoms at cryogenic temperatures, and the phenomena were reproduced by the numerical simulation. Therefore, metastable helium atoms, which have longer lifetime at lower temperature, are key species in chemical reactions in

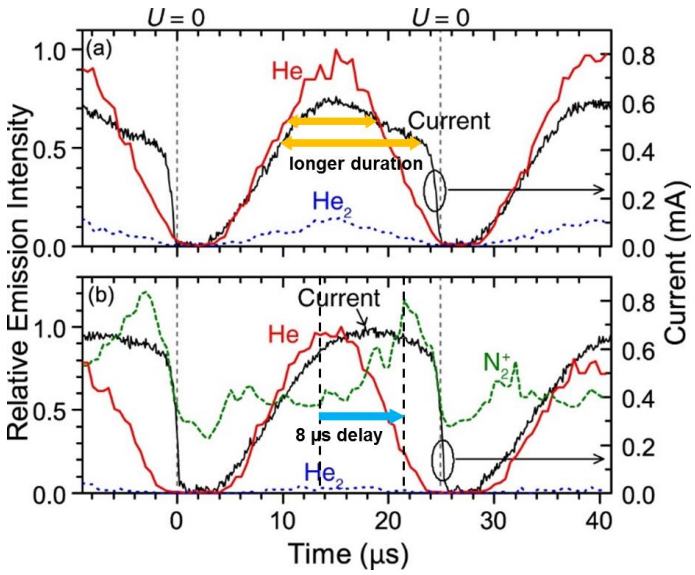

Figure 1.9 Time evolution of relative emission intensities of He (706.5 nm, solid red line), He_2 (640 nm, dotted blue line), and N_2^+ (391.4 nm, short dashed green line) at (a) T_g = 28 K and (b) T_g = 54 K. Adopted from [29] with the permission of Institute of Physics Publishing.

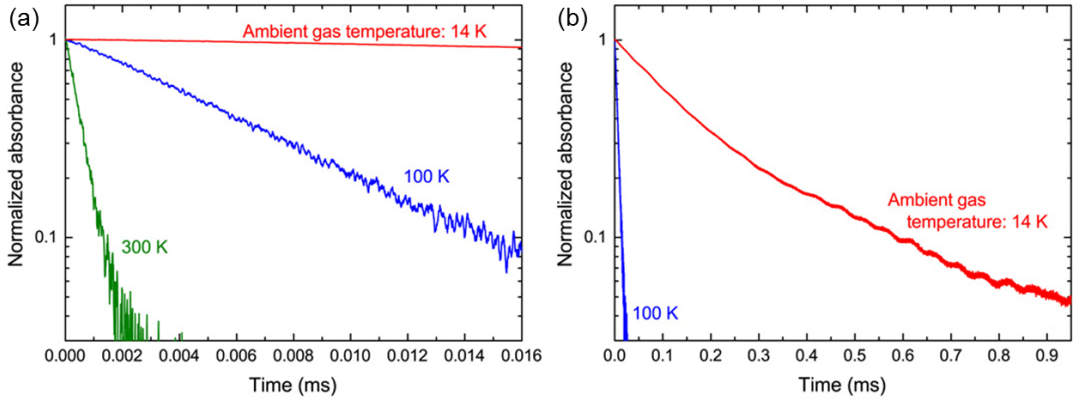

Figure 1.10 Time evolution of normalized absorbance in the afterglow of helium metastable atoms in cryoplasma at 300, 100 and 14 K (T_g = 307, 114, 31 K at the maximum, at each condition). (a) shows a short time range and (b) shows a long time range. Adopted from [30] with the permission of Institute of Physics Publishing.

helium cryoplasma.

In order to measure the density and lifetime of metastable helium atoms directly, laser absorption spectroscopy was conducted in helium cryoplasma. In the laser absorption spectroscopy, longer lifetime at lower temperature was observed, 0.59 μs at 300 K, 6.5 μs at 100 K, and 180 μs at 14 K, as shown in Fig. 1.10. Comparing the lifetime at lower temperatures with that at 300 K, it became 10 times longer at 100 K and 300 times longer at 14 K. This longer lifetime at lower temperature is attributed to slow quenching reactions of metastable helium atoms at lower temperature, where cryogenic temperature causes lower impurity level and lower collision frequency.

1-2. Ice

Ice might not be reactive enough at first glance to influence of reactions and phenomena in nature. However, ice, especially ice surface, is an important condensed phase that dominates chemical reactions at low temperatures. Here, the properties and reactivities of ice and its surface are overviewed.

1-2-1. Overview: Ice surface as a reaction field

Ice is a solid state of water or other low-molecular-weight molecules at low temperatures, and is one of the most important and abundant solid components both on earth and in astrophysical and planetary environments. At the temperature of ice, thermal reaction rate overcoming an Arrhenius activation barrier is much slower than at room temperature or more. In addition, diffusion rate of chemical species and reagent is lower by several orders of magnitude. As above, chemical reactions with an appreciable speed is considered to be doubtful, and this is generally the case in bulk ice. This might lead us to think that ice is not so important when considering chemical reactions. However, recent studies have shown that chemical reactions occur on the surface of ice even at cryogenic temperatures. For example, in the star-forming region in the dense regions of interstellar space which is known to be molecular clouds (with a typical temperature of ~10 K), abundances of gas phase H_2, NH_3 are enhanced, and the presence of alcohols such as CH_3OH has been observed. These observations cannot be explained only by gas phase processes. The origin of the enhanced abundances, and the presence of more complicated species, could be attributed to the combination of the ice surface chemistry of gas species and the desorption of molecular ices that have processed on the surface of dust grains [31]. Energetic radicals and charged particles produced by energetic radiation to ice could influence on both thermal and nonthermal ice surface processes such as diffusion and desorption of molecular species [32]. Therefore, ice surface plays a key role in chemical reactions in various natural phenomena at low temperatures [33] (Fig. 1.11).

One of the largest interests of ice surface chemistry is the destruction of ozone layer. In the field of atmospheric chemistry and environmental science, formation of ozone hole is a big issue [14]. As is widely

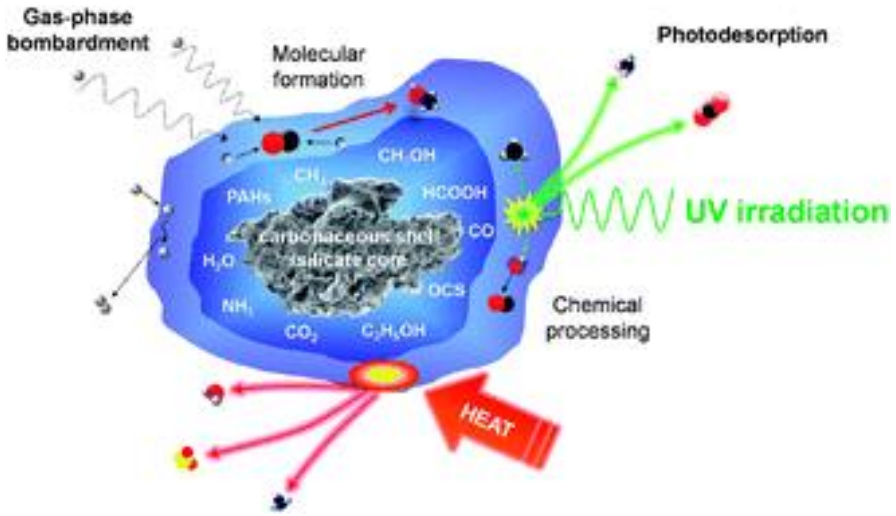

Figure 1.11 Schematic of the main routes of interstellar ice processing that occurs in astrophysical environments. Adopted from [31] with the permission of Royal Society of Chemistry.

known, the ozone layer is at the altitude of 10–50 km, and is indispensable for protecting the Earth from exposure to ultra-violet (UV) radiation. Active chlorine species are the cause for the generation of the ozone hole, which are generated in polar stratospheric clouds. In the clouds, where the temperature is about 200 K, active chlorine species are generated mainly on ice surface, as follows.

$$HCl\ (\text{on ice}) + ClONO_2\ (\text{gas}) \rightarrow Cl_2\ (\text{gas}) + HNO_3\ (\text{ice}) \quad (1.7)$$

$$H_2O\ (\text{ice}) + ClONO_2\ (\text{gas}) \rightarrow HOCl\ (\text{gas}) + HNO_3\ (\text{ice}) \quad (1.8)$$

$$HCl\ (\text{on ice}) + HOCl\ (\text{gas}) \rightarrow Cl_2\ (\text{gas}) + H_2O\ (\text{ice}) \quad (1.9)$$

These reactions produce 100 times more active chlorine species than in gas phase. Therefore, ice particles in the polar stratospheric clouds play catalytic roles in the depletion of the ozone layer, where ice surface governs the reactions. In the reactions on the surface of ice, adsorption, trapping and accumulation of chemical species are a key factor contributing to the high reaction rate on the ice surface.

Ice surface also provides an important reaction field in astrophysical environments. As a model of interstellar molecular clouds, where the temperature is as low as 10 K, quantum-tunneling diffusion of hydrogen atoms on the surface of polycrystalline ice was reported [34–36]. The tunneling diffusion allows much faster movements of hydrogen atoms than expected compared to the classical thermal hopping.

On the other hand, as essential molecular components of living organisms on Earth, the delivery of extraterrestrial organic molecules to Earth could account for the origin and early evolution of life. In interstellar ice analogue laboratory experiments, the formation of prebiotic organic compounds on ice surface [32], such as amino acids [37, 38], ribose [39], and nucleobase [40], has been reported. In the case of the amino acid synthesis, UV was irradiated on amorphous H_2O ice at 15 K with a small amount of ammonia, ethanol and hydrogen cyanide. Photochemical reactions proceeded on the ice surface, and as a result, the formation of serine, glycine, alanine and other organic compounds were identified by high-precision liquid chromatography [37].

1-2-2. Structural properties of H_2O ice surface

Among ices composed of many kinds of molecules, H_2O ice is a dominant component of various ices observed on Earth and in astrophysical environments such as comets, planetary objects, and interstellar dust [32]. Hence, chemical processes on H_2O ice surface is of fundamental importance to the understanding of many astrophysical and terrestrial processes. The structure of H_2O ice can be varied depending on temperature and pressure conditions. In the terrestrial environment and some bodies of the solar system, hexagonal crystalline ice (ice I_h) is the dominant stable phase of H_2O ice. On the other hand, in astrophysical environments, amorphous solid water (ASW) is known to be the most abundant phase of H_2O ice [31]. The unique chemical and physical properties of ice surface can be attributed to the modified structure of the surface of ice. The dangling O-H bonds as well as the relatively weaker hydrogen bonding at the surface contributes to the mobility of molecules on the surface [41]. Therefore, when investigating ice surface chemistry on Earth or in the universe by laboratory experiments, the structure and surface condition of ice should be carefully prepared and simulated according to the targeted environment.

The structure and properties of H_2O ice surface change significantly depending on its temperature. A schematic illustration of the change in ice surface structure is shown in Fig. 1.12. At low temperatures

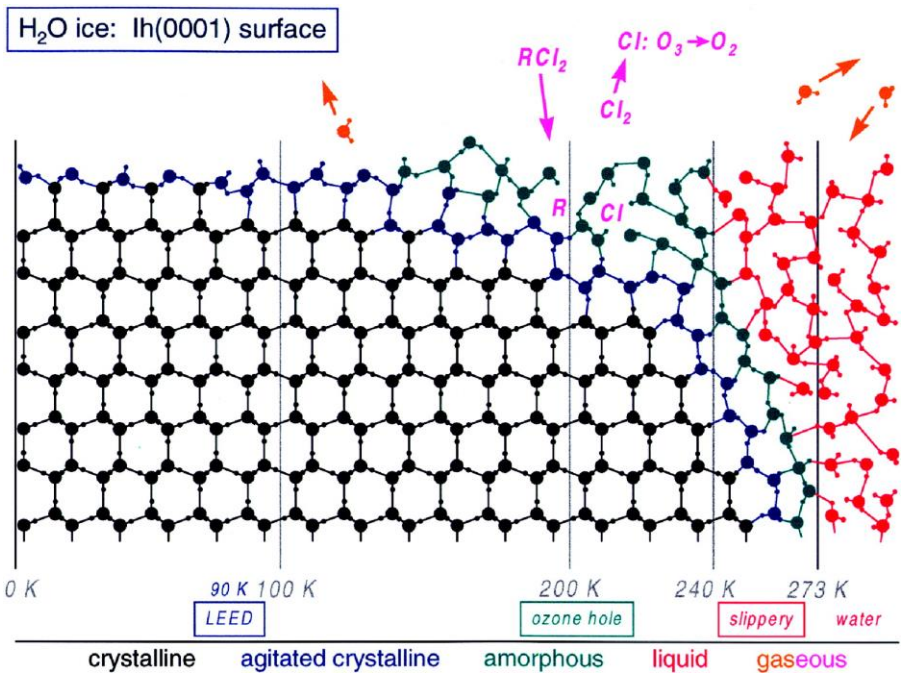

Figure 1.12 Schematic illustration of the evolution of the surface structure of ice as temperature rises from absolute zero (at left) to above the bulk melting point of water (273 K, at right). Adopted from [41] with the permission of American Chemical Society.

below 100 K, H_2O molecules on the surface remain in crystalline state, whereas H_2O molecules in the most top layer have large vibration (referred to as agitated crystalline in the figure) [41]. As the temperature increases at 100–200 K, the surface H_2O molecules gain more energy, resulting in the formation of more crystalline defects and some extent of amorphous state. When the temperature elevates at 200–240 K, such molecular disorders on the surface become larger, eventually forming quasi-liquid layer below the melting point of water [41, 42]. Even though the onset temperature of the amorphous structure and quasi-liquid layer are not yet clearly established and are reported to have a wide range between 180 K and 260 K, this molecular disorder on the H_2O ice surface has been known to enhance chemical reactions [43].

1-2-3. Mobility of H_2O molecules on ice surface

Self-diffusion of H_2O molecules enables the solvation of molecules and charged species adsorbed on the ice surface, resulting in the stabilization of them on the ice surface and their subsequent participation in chemical reactions. In addition, self-diffusion also controls the migration of molecules dissolved at the surface of ice. Therefore, self-diffusion is significantly relevant to the ice surface chemistry, by facilitating and controlling the rates of reactions at the surface [33].

At temperatures below 150 K, most H_2O molecules are fixed because H_2O molecules on the surface are in crystalline state, as illustrated in Fig. 1.12. However, on a long timescale, the relatively large vibrational amplitude of H_2O molecules at the most top surface can promote molecular (re)arrangement, which results in a high concentration of crystalline defects at the ice surface. Through the migration of the crystalline defects, self-diffusion of surface molecules, not only H_2O molecules but also molecules adsorbed or dissolved on the ice surface, can occur even at low temperatures [43, 44].

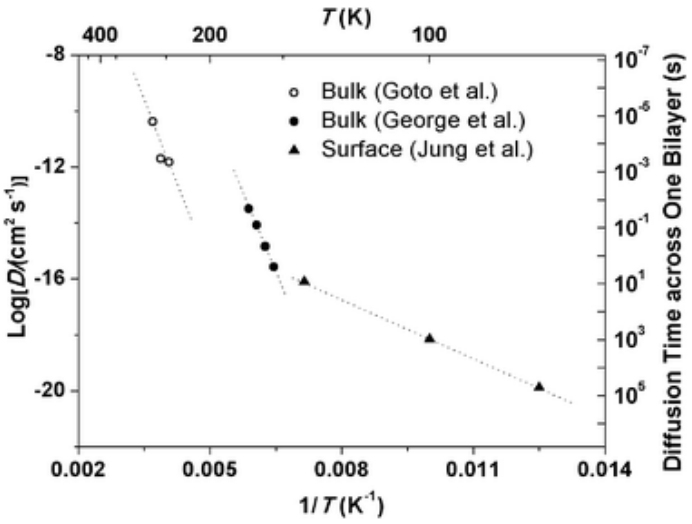

Figure 1.13 Arrhenius plots for the self-diffusion coefficients measured at ice surface and in ice bulk. Adopted from [43] with the permission of Royal Society of Chemistry.

Such dynamic characteristics of self-diffusion of H_2O molecules on the ice surface contribute to the relatively high reactivity of ice surface as compared to bulk ice at low temperatures. Figure 1.13 shows the Arrhenius plot of bulk and surface self-diffusion coefficients of H_2O molecules. From Fig. 1.13, it can be seen that the self-diffusion coefficient for surface diffusion is larger than that of bulk diffusion below 150 K. Hence, surface diffusion with a lower activation energy occurs faster than bulk diffusion, and this is the case especially at lower temperatures. This higher self-diffusion coefficient on the ice surface can be attributed to the weaker hydrogen bonding at the surface than in bulk. This means that less energy is required to break the hydrogen bonding at the surface. Furthermore, the high concentration of crystalline defects closer to the surface also enables migration of molecules to occur more easily than in bulk ice.

1-2-4. Reactions on H_2O ice surface

The primary factor that controls the ice surface reactions is the mobility of molecules, as described above. Because water molecules are more mobile on the surface than in bulk ice at temperatures lower than 150 K, chemical processes can occur on ice surface with appreciable speed and enhanced selectivity, though much more slowly than in liquid phase. Under such situation, chemical reactions are guided by kinetic constraints rather than thermodynamics [33]. The kinetic factors on ice surface is in the following: incomplete proton transfer between different donor and acceptor species, isolation of reaction intermediates, preferential stabilization of charged species, and various kinds of reaction products. In this way, ice surface provides heterogeneous reaction field specific to low and cryogenic temperatures.

1-2-5. Self-assembling structure on ice surface

Not only H_2O ice but also ice of aqueous solutions possess various fascinating properties. In the case of solutions, water ice and liquid water coexist in a eutectic binary system over a temperature range from several to some tens of degrees between the melting point of water and the eutectic point of the system, depending on the kind of aqueous solutions.

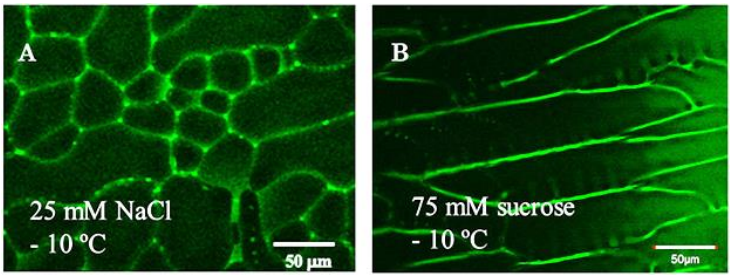

Figure 1.15 Ice grain boundary channels formed on frozen (A) NaCl and (B) sucrose solution. 1.0 μL fluorescein disodium was added into the solutions before freezing. The green and black areas represent liquid phase and ice, respectively. Adopted from [45] with the permission of Springer Nature.

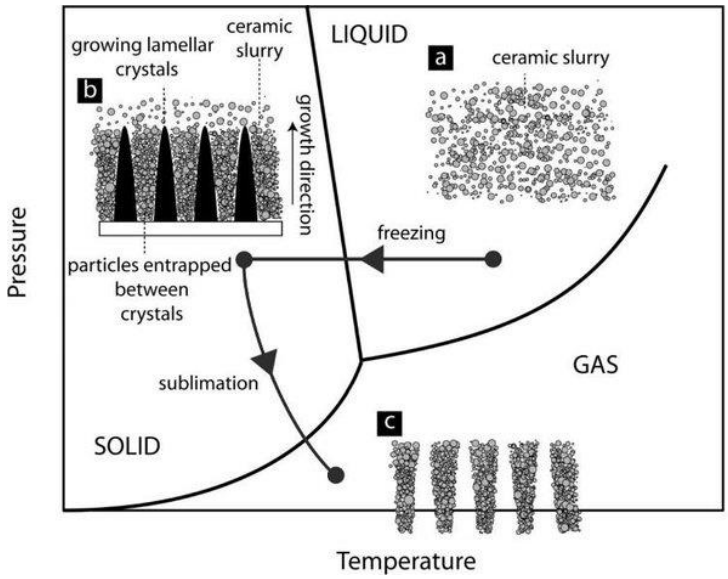

Figure 1.14 Schematic illustration of the procedure of freeze casting, depicted on phase diagram. Adopted from [49] with the permission of Elsevier.

When freezing an aqueous solution, the solute is expelled from the ice crystals and is accumulated inside the ice grain boundaries. Above the eutectic point, the solute remains dissolved in the liquid phase, resulting in concentration of solutes in liquid phase. The dense solution can exist on the ice surface or inside the ice grain boundaries. On ice surface, the dense solution forms thin liquid layer, whereas the dense solution inside the grain boundaries forms channels, the structure of grooves. Figure 1.14 exhibits the liquid thin layer and channels on the ice of NaCl or sucrose solutions [45]. The thickness of the self-assembled liquid layer or the width of channels are expected to be controlled by thermodynamic parameter when considering binary phase diagram. In previous studies, the size control of channel width has been reported, demonstrating the advantageous characteristics of channel as a micro- or nano fluidic device whose size can be tuned by temperature [43, 46].

On the other hand, in the case of freezing of colloidal dispersion that contains solid particles in liquid phase, lamellar structure of ice bulk is formed spontaneously. Solid particles are rejected from the moving solidification front and piled up between the growing solvent crystals [47]. This enables the usage of the self-assembling lamellar-structured ice body as a scaffold for designing a unique architecture of bioinspired

structural materials. This technique is known as freeze casting as shown in Fig. 1.15, which originates in the fabrication of strong and tough organic-inorganic hierarchical structural materials which mimicked the nacre structure [15, 44, 49]. The process of the freeze casting can be properly adjusted for a targeted purpose: the size of the lamellar structure and its morphology can be controlled by ice the growth velocity, while the porosity (the density of the lamellar structure) can be tuned by the concentration of colloidal dispersion.

These self-assembling structures accompanied by freezing of aqueous solutions or colloidal dispersion are highly attractive as a novel approach for materials design. However, there has been only a few studies which induce chemical reactions with the self-assembling structures [50, 51]. Here, I propose to exploit the cryoplasma to proceed chemical reactions with the self-assembling structures, which might promote further development of the self-assembling structures as a novel materials processing. In other words, plasma-ice interfacial reaction field might have potential advantages for engineering applications such as a novel technique of materials design. In this dissertation, by adding reactivity to the liquid layer on frozen aqueous solution by cryoplasma, novel technique for thin film synthesis was performed.

1-3. Plasma in contact with liquid

When considering the combination of plasma with ice, there could be liquid phase at plasma-ice interface, according to temperature and other conditions. Therefore, the knowledge on the plasma-induced chemical reactions in liquid is significant for the development of plasma-ice interfacial reaction field. As for the plasma processing in contact with liquid phase, many studies have been performed vigorously in the last decades. In this chapter, plasma in contact with liquid is briefly overviewed.

1-3-1. Overview of plasma in contact with liquid

Plasma in contact with liquid is recently gaining increasing attention in the field of plasma science and technology [8, 52–54]. Plasma in contact with liquid is opening various applications in wide research areas, such as nanoparticles synthesis [52–58], surface modification [59, 60], food and agriculture [61], sterilization [62], and biological and medical applications [63, 64]. Plasma processes in contact with liquid have been widely used in conventional applications such as arc spraying by thermal plasma [65], electric discharge machining in liquid, and chemical analysis by inductively coupled plasma (ICP). In recent years, the development of atmospheric-pressure non-equilibrium plasma allows the enhancement of chemical reaction processes in liquid due to their high reactivity without any marked temperature elevation of the environment.

Plasma in contact with liquid includes plasma in liquid (solution plasma) [52], plasma on liquid surface [53], plasma with aerosols [66] or microdroplets [67], and so on. In the liquid phase in contact with plasma, novel chemical reactions are induced by charged particles and reactive species from plasma, as shown in Fig. 1.16. In particular, short-lived species generated in liquid phase such as solvated electron (e_{aq}^-), hydroxyl radical (OH*), atomic hydrogen radical (H*), results in high and distinctive reactivity of the plasma-induced liquid phase reaction field. In addition, long-lived species such as hydrogen peroxide (H_2O_2) and nitrogen and oxygen reactive species (RONS), charging and adsorption of reactive species onto the liquid surface, heat transport, and photochemical reactions, also affects the liquid phase reaction. Therefore, plasma-induced liquid phase reaction field is generally highly complicated. In this way, plasma-liquid interaction system is very promising research area for next-generation applications.

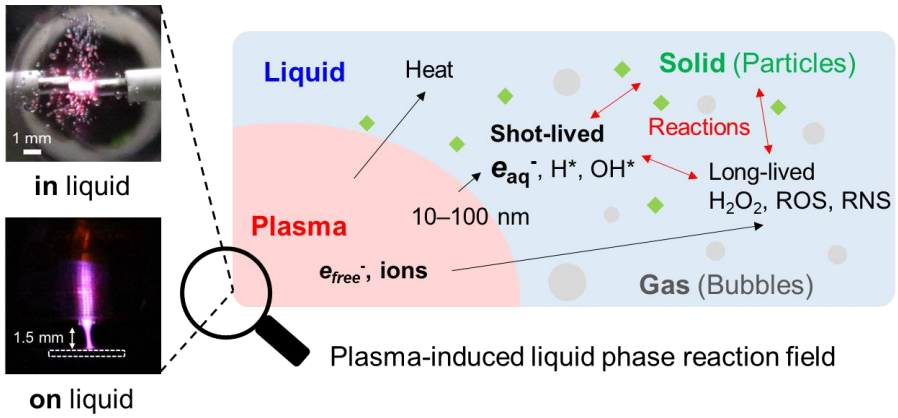

Figure 1.16 Schematic diagram of the interaction of reactive species produced by plasma in contact with aqueous solution.

1-3-2. Synthesis of metal nanoparticles with plasma in contact with liquid

Plasma in contact with liquid offers an enhanced reaction field in solution chemistry, being expected for the development of new nanomaterials and functional properties. As one typical example, many studies on synthesis of metal nanoparticles with plasma in contact with liquid are reported [55–58]. At the interfacial part between plasma and liquid, electrons penetrate into the liquid phase and generate a lot of solvated electrons, radicals, and other kinds of reactive species. Because of the solvated electrons or reactive species with high reducibility, metal ions can be reduced without any additional reducing agent. In addition, surfactant-free metal particle synthesis has also been achieved in some cases.

For example, during plasma processing in aqueous solution of gold ions, time-dependent growth of gold nanoparticles was reported as shown in Fig. 1.17 [57]. Hexagonal and dendrite-shaped nanoparticles were observed in the solution after 5 min discharge. Particles size decreased from about 50 to 30 nm and small new particles about 20 nm in size were formed. After that, particles size continued to decrease gradually, and gold nanoparticles around 20 nm were produced after 45 min discharge, which had various shapes, such as triangles, pentagons, and hexagons (left side of Fig. 1.17). The decrease in size of nanoparticles indicated dissolution of gold nanoparticles into the solution, being related to the pH decrease with increasing discharge time.

1-3-3. Control of plasma-induced liquid phase reaction field

For further advances of processing by plasma in contact with liquid, control of the reaction field is indispensable. One promising approach to achieve the controllability is the development of plasma with aerosols or microdroplets. By introducing microdroplets in sub-micron to micrometer size into plasma, the microdroplets can be used as a micro- or nano-scale reactor with enhanced reactivity by plasma. For example, in the case of zinc oxide spherical nanoparticle synthesis by plasma with aerosols, size control of the nanoparticles was achieved with exploiting one microdroplet with plasma for the synthesis of one

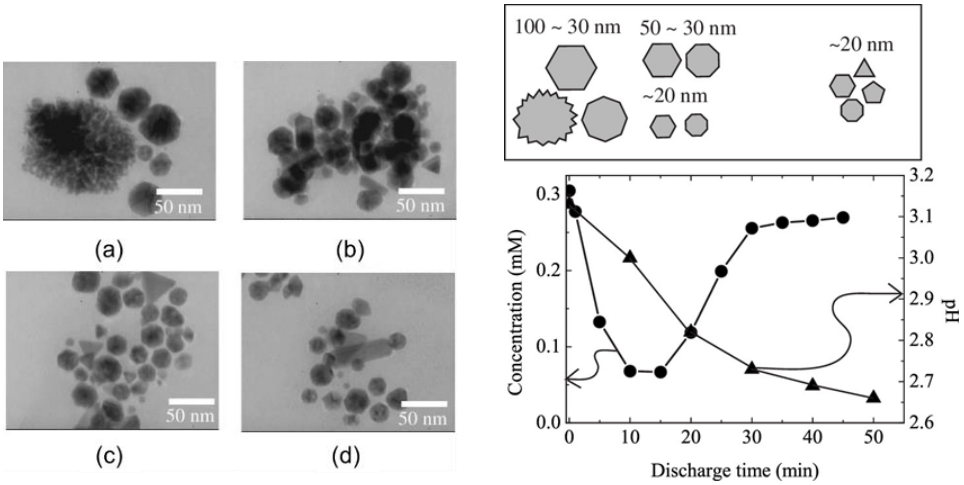

Figure 1.17 (Left side) TEM image of gold nanoparticles prepared by discharge in 0.3 mM $HAuCl_4$ solution after (a) 5 min, (b) 15 min, (c) 25 min, and (d) 45 min. (Right side) Time evolutions of shapes and size of gold nanoparticles, concentration of $[AuCl_4]^-$, and pH. Adopted from [57] with the permission of American Institute of Physics Publishing.

nanoparticle [66]. In addition, the confinement of liquid phase to nano- or micrometer scale could also enhance the effect of short-lived species, because the diffusion length of such species during the lifetime (typically from ns to ms) is in nano- to micrometer. At the same time, microdroplets have large surface area in contact with plasma, which could enhance the effect of novel reactivity at plasma-liquid interface. Therefore, control of the reactivity could also be achieved by control the size of the plasma-induced liquid phase reaction field. In this dissertation, nano- or micrometer scale plasma-induced liquid phase reaction field was developed by activating thin liquid layer on ice with cryoplasma. This could provide a new approach to control plasma-induced liquid phase reaction field.

1-4. Laboratory simulation of astrochemistry

Low and cryogenic temperature environments spread in the universe, which should contain icy grains and icy planetary bodies. In such an environment, ice bodies are subject to energetic radiations and chemical reactions are proceeded although the temperature is very low. To simulate and investigate chemical reactions under the low temperature environments, plasma is generally used as one of the reasonable techniques. Here, laboratory simulations of cryogenic astrophysical environments by plasma is overviewed, and one large problem in such previous studies is proposed. We mentioned more details in [Publication-1] in my achievement list.

1-4-1. Overview of astrochemistry

The origin of life on Earth remains a mystery, but the search for and knowledge of the origin of life on Earth gives us deep insights into what life is and what makes life like to be us. Our lives are based on the chemistry of carbon. One possible hypothesis is that the components of lives, such as amino acids and nucleobases, may have been directly delivered from outside of the Earth. Therefore, the formation and destruction of molecules in the universe are significant for understanding both the evolution of stellar and planetary systems and the origin of life.

Astrochemistry is concerned with understanding the chemical evolution in the universe. Active synthesis of organic substances are thought to occur in various astrophysical environments such as the follows: in the interstellar medium, where the stars are formed [68–70], in planetary systems [71, 72], and in comets, asteroids and icy bodies in the outer solar system [73, 74]. Note that most of the astrophysical environments are in low temperature or cryogenic conditions below the freezing point of water. For example, average temperature in the solar system is below the melting point of water outside of Mars, as shown in Fig. 1.18. The frost-line, which represents the distance from the Sun beyond which water and

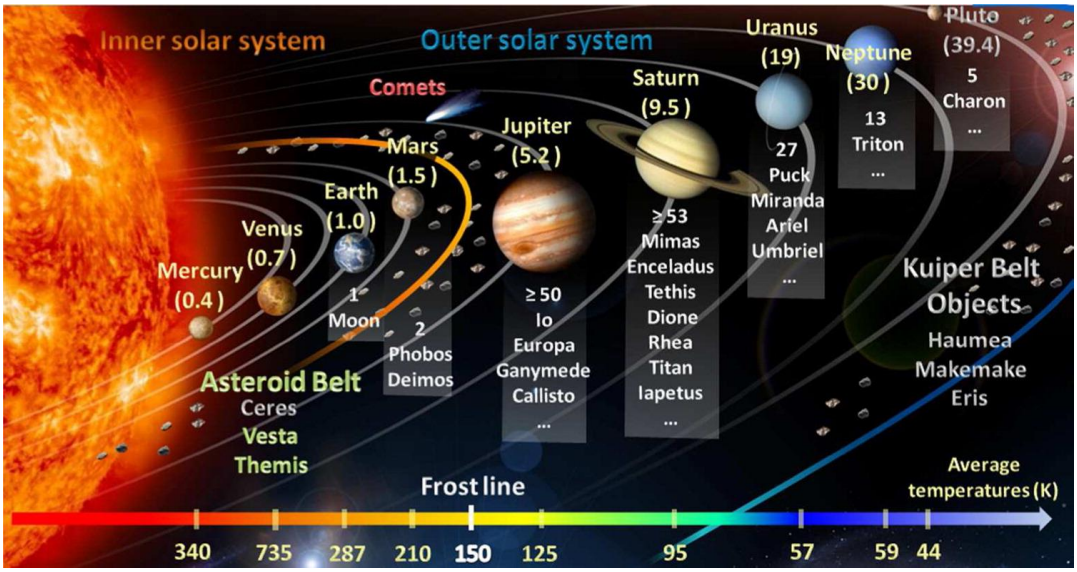

Figure 1.18 Planetary bodies, asteroids and tran-Neptunian objects in the solar system, with the temperature indication of the bodies. Adopted from [75] with the permission of American Chemical Society.

other volatiles are found predominantly in its condensed phase, is observed as well typically at 2.7–5 AU and at temperatures of 150–170 K [75]. AU means astronomical units where 1 AU represents the mean distance between Earth and the Sun of 149597871 km. A dominant driving force for the formation of organic molecules is considered to be the energy deposition from radiation sources such as ultraviolet (UV), cosmic rays, and solar wind, resulting in complex chemical processes in surface and atmosphere of the bodies (Fig. 1.19).

To investigate the nature and chemical processes in the astrophysical environment, the following three approaches are mainly used [72, 76, 77]: (1) remote observation or *in-situ* sampling of atmospheric and

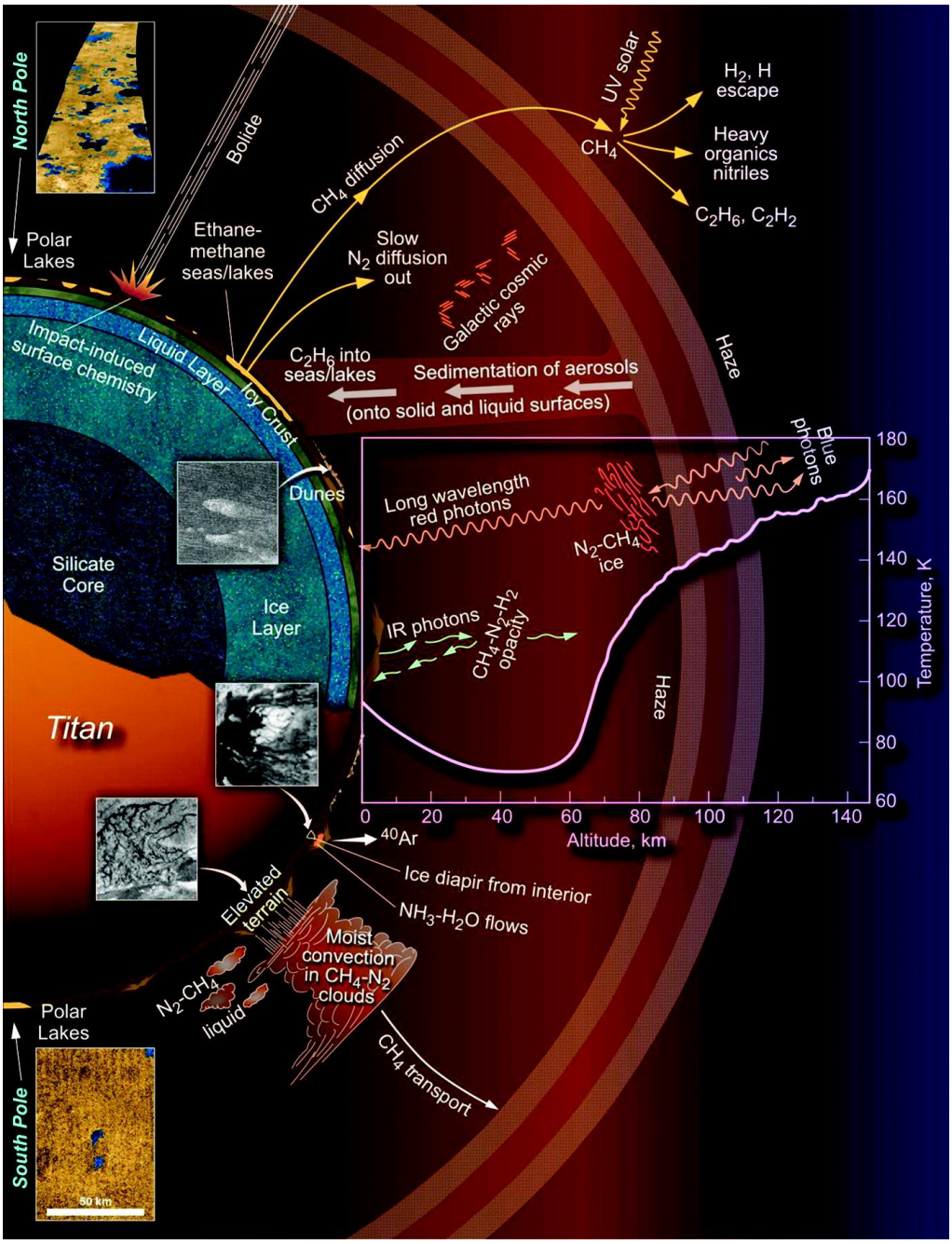

Figure 1.19 Diagram of the complex processes in the atmosphere, lakes and surface and subsurface of the Titan environment. Adopted from [72] with the permission of American Chemical Society.

surface materials, (2) theoretical modeling and analysis of the kinetics and dynamics of chemical reactions, (3) laboratory experiments to simulate the targeted environment. Not only observational and theoretical approaches but also laboratory simulations are very useful to improve our knowledge regarding chemical processes and abundances, because observational approaches might suffer from technical detection limitations and are time- and cost-consuming. Furthermore, laboratory simulation could provide a new guidelines and realistic constrains for both observational and theoretical approaches, by the demonstration of various organic molecules that have been observed in the universe, as well as potential species that have yet to be detected in the observations. Laboratory experiments have been extensively performed to investigate space weathering and chemical modifications induced by the energy deposition. In these experiments, many factors of conditions in the targeted astrophysical environment should be simulated, such as energy sources, physical parameters including temperature and pressure, and reactants.

1-4-2. Classification of energy sources for laboratory simulation

In laboratory simulations, various energy sources are used to induce chemical reactions, depending on the phenomena and environment to be studied. In astrophysical environment, interstellar ices, planetary bodies, and cometary bodies are constantly exposed to energetic particles including photons, electrons, and ions, that originate from various primary radiation sources such as cosmic rays, solar wind, magnetospheric particles, and UV radiation. These primary radiations often consist of highly energetic particles. For example, cosmic rays mainly comprise protons with kinetic energy in the GeV range [78], while solar wind mainly comprises protons with kinetic energy in the keV range [79]. To simulate such primary radiations, many studies have employed gamma radiation, high-energy charged particle beam such as ~MeV proton [80, 81] and ~keV He^+ ions [82], and high-energy electron beam [79]. On the other hand, the interaction of primary radiations with gaseous molecules and cosmic ices can produce secondary particles and induce subsequent chemical reactions. For example, low-energy secondary electrons less than 15 eV are known to be produced [72, 83, 84]. The effects of such secondary particles can be reasonably simulated by low-energy electron beams [84, 85], as well as non-equilibrium low-temperature plasma [72], with kinetic energy less than 10 eV. In particular, non-equilibrium low-temperature plasma can simulate chemical processes triggered by many kinds of charged particles and reactive species simultaneously.

1-4-3. Laboratory simulation by low-temperature plasma

One major advantage of low-temperature plasma in laboratory simulations is its non-equilibrium characteristics: the electron temperature typically reaches several thousand Kelvin (a few eV), whereas gas temperature in plasma is often slightly higher than room temperature because only a small fraction of the gas is ionized. This triggers chemical reactions much lower than thermal reactions at thermodynamic equilibrium, resulting in efficient generation of reactive species in mild conditions without thermal or equilibrium constraints [72].

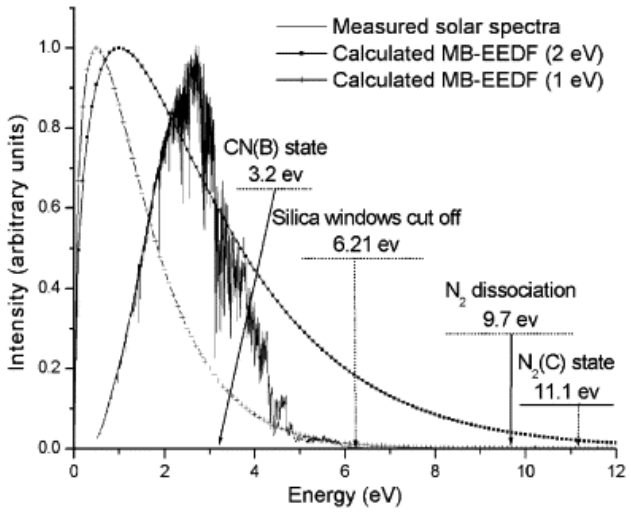

Figure 1.21 Solar spectrum compared with two Maxwellian EEDF of plasma at 1 and 2 eV. Adopted from [86] with the permission of Elsevier.

Figure 1.20 Images of (a) Titan (copyright NASA), (b) plasma equipment PAMPRE, and (c) synthesized organic aerosols with yellow color analogous to Titan. Images of (b) and (c) were adopted from [87] with the permissions of Springer.

For the laboratory simulation of planetary bodies in the solar system, low-temperature plasma is suitable energy source, because a Maxwellian electron energy distribution function (EEDF) of 1–2 eV has a similar broad spectrum to the solar radiation spectrum, as shown in Fig. 1.20. Although the EEDF of low-temperature plasma can deviate from a Maxwellian distribution practically, the energy range of electrons in low-temperature plasma can be approximated to be similar to that of solar photons [86].

Based on the EEDF of low-temperature plasma, the electrons in high-energy tail of the EEDF (> 10 eV) have sufficient energy to dissociate molecular bonds with high dissociation energies such as N_2 (9.76 eV). In contrast, UV radiation often cannot dissociate molecular nitrogen because of low cross-section of N_2 with far-UV wavelengths (115–200 nm, corresponding to 6.2–10.8 eV). Accordingly, in laboratory simulation with low-temperature plasma, almost all kinds of species (not only carbonaceous but also nitrogen-containing reactive species) can be involved in the chemical processes of organic synthesis. For example, in the mixture of methane and nitrogen gas, the analog of Titan's organic yellow aerosols was synthesized by using low-temperature plasma, as shown in Fig. 1.21, in many laboratories [87, 88].

1-4-4. Necessity of laboratory simulation at cryogenic temperatures

Although low-temperature plasma possesses advantages to simulate astrophysical environments as mentioned above, the gas temperature in plasma has not been controlled to the temperature of the targeted environment. Most experiments have been conducted at room temperature, which is considerably higher than that of various astrophysical environments. This is because the gas temperature of low-temperature plasma that is currently used widely in industrial processes remains slightly higher than room temperature. However, laboratory simulations at cryogenic temperatures are indispensable for further insight into the nature of the universe, because cryogenic temperatures are representative of astrophysical environments [89], as shown in the temperature distribution of various Solar System planets in Fig. 1.22, and temperature is a key parameter that highly influences on multiple properties of chemical reactions, such as thermodynamic stability of reactants and products, and reaction kinetics. For example, dicyanoacetylene (C_4N_2), which has been detected in Titan's atmosphere, is observed in the simulating experiment only when cooling a reactor to 100–150 K because of its thermal instability [76]. Therefore, laboratory simulations at cryogenic temperatures are significant for a more comprehensive understanding of chemical processes that occur in various environments in the universe.

In addition, temperature can also influence the phases in which the material can exist. Other than gaseous atmospheres, matters of different phases exist in the universe. In particular, at cryogenic temperatures, ice is ubiquitous and provides a dominant reaction field, as mentioned in chapter 1.2. For example, Pluto's surface is covered with ice composed of nitrogen, methane, water and other hydrocarbons [90] due to its surface temperature of ~40 K. Many other bodies and comets in the outer solar system, such as trans-Neptunian objects, are made up of significant amounts of ice [91]. These different phases of matter at different cryogenic temperatures can have significant influences on the radiation chemistry on such icy bodies. Therefore, laboratory simulations should be performed in the same phase of matter as that observed in the astrophysical environment.

Several studies have attempted to simulate cryogenic temperature conditions, mainly that of Titan, by cooling plasma reactor using liquid nitrogen [70, 76, 92–95]. These studies synthesized the analogs of

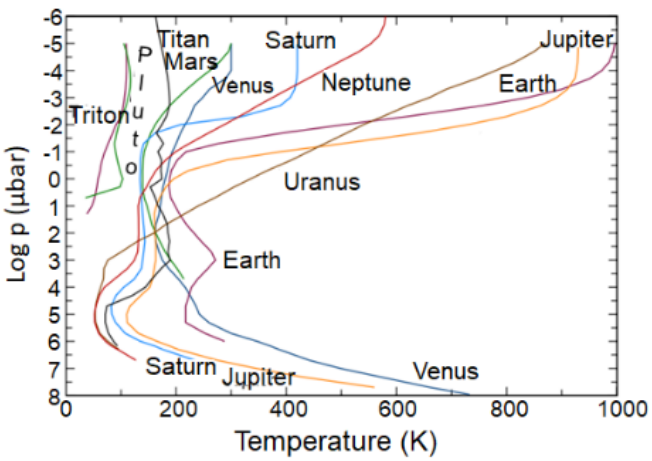

Figure 1.22 Temperatures versus pressure of the atmosphere of various Solar System planets and Pluto. Adopted from [89] with the permission of Springer.

Titan's organic aerosols to investigate the effect of low temperature and chemical pathways.

However, temperature control of the reaction system in a continuous way has not been performed in the previous studies. A continuous temperature control is necessary to simulate the temperature gradient that exist throughout the universe [72]. Furthermore, investigation of temperature dependence at cryogenic temperatures are indispensable to provide a more comprehensive understanding of chemical processes and temperature-dependent chemical evolutions that occur in the universe. To realize a laboratory simulation with a continuous temperature control by using low-temperature plasma, plasma-ice interfacial reaction field is exploited in this dissertation, as a novel approach to the chemistry and materials science in cryogenic astrophysical environment.

1-5. Purpose of this dissertation

In this dissertation, generation and application of plasma-ice interfacial reaction field was studied, with controlling gas temperature or temperature of the system, taking advantage of the knowledge of cryoplasma. Combination of high reactivity of plasma with distinctive reaction field of ice surface can be anticipated not only as a new approach to atmospheric chemistry and astrophysics but also as a novel reaction field for materials design (Fig. 1.23). The purpose of this research is the establishment of plasma-ice interfacial reaction field as a new research area.

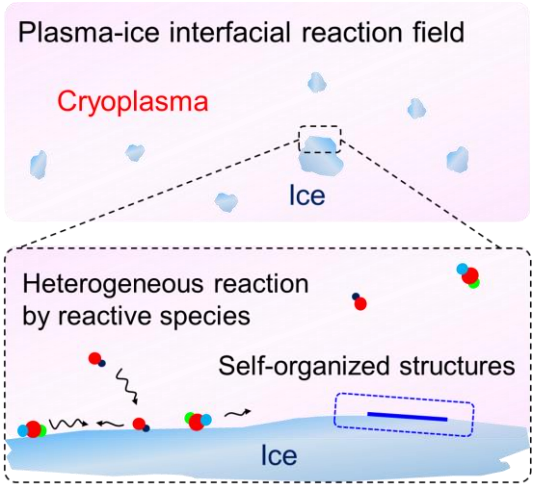

Figure 1.23 Concept illustration of plasma-ice interfacial reaction field, where the reactivity of cryoplasma is superposed onto the superior characteristics of ice surface as a reaction field.

Four approaches were performed in this research. At first, cryoplasma was diagnosed in terms of plasma chemistry, prior to the generation and application of plasma-ice interfacial reaction field. Evaluation of gas temperature and the density and lifetime of metastable helium atoms in cryoplasma was conducted with laser measurement, and the mechanism of quenching reactions of metastable helium atoms were investigated based on the result of the measurement. For the next step, dielectric barrier discharge in cryogenic environment which contains ice as a dielectric barrier, which is named as ice DBD, was generated at a wide range of gas temperature below the melting point of water (273 K) down to 6.5 K. Through this, a reproducible generation of plasma-ice interfacial reaction field was established. Furthermore, to explore the possible applications of the plasma-ice interfacial reaction field, simulation of cryogenic astrophysical environment and development of a new scheme of thin film synthesis were performed, in terms of science and engineering, respectively.

Chapter.2 Laser diagnostics of cryoplasma

Laser diagnostics of cryoplasma were conducted in this chapter to get better understanding the gas temperature dependence of chemical reactions in cryoplasma, prior to the generation and application of plasma-ice interfacial reaction field.

Cryoplasma exhibits various unique characteristics depending on gas temperature, and gas temperature dependence of chemical reactions in helium cryoplasma is now under investigation [29, 30]. However, the measurement of gas temperature in plasma is not straightforward, and gas temperature was only estimated by thermal simulations from the temperature outside plasma measured by a thermometer in our previous studies. For a better evaluation of gas temperature, near-infrared laser heterodyne interferometry (NIR-LHI) was conducted, which has recently been revealed to be promising for the evaluation of not only electron density but also gas temperature in non-equilibrium plasma in high density fluid conditions including atmospheric pressure [96, 97]. It is advantageous because of its non-contact measurement without disturbing plasma itself.

Furthermore, laser absorption spectroscopy (LAS) was conducted in the same plasma source to measure the density and lifetime of metastable helium atoms. From the result of the LAS and NIR-LHI measurements, gas temperature dependence of the mechanism of quenching reactions of metastable helium atoms was discussed by the calculation of reaction rates with taking evaluated gas temperature into account. For the plasma source, atmospheric pressure helium pulsed discharge plasma was generated for the laser diagnostics in room and cryogenic temperature environments, which was chosen for the reason of easy signals detection.

2-1. Experimental approach

2-1-1. Experimental setup for the generation of discharge plasma

The experimental setup for the generation of the discharge plasmas is shown in Fig. 2.1. For the electrodes, polished copper rods with a diameter of 2 mm were set in parallel with a gap distance of 530 ± 50 μm. The reactor (Suzuki Shokan) was set on an *XY* stage for ease of optical alignment and to allow space-resolved scanning for the laser measurements. The reactor comprised an inner chamber, an outer chamber, and a liquid nitrogen (LN_2) tank. Th e ambient gas temperature inside the inner chamber (T_a) was set to values of 340, 300, 250, 200, 150, and 100 K by proportional-integral-derivative (PID) control, using a temperature controller (DB1000, CHINO), cooling by LN_2, and heating by two heaters. A turbomolecular pump and a diaphragm pump (Hi Cube 80 Eco, PFEIFFER VACUUM) were used, respectively, for rough and main pumping. The inner chamber was filled with helium gas (purity > 99.99995%) keeping the pressure inside the inner chamber at atmospheric pressure for all six T_a conditions. Therefore, the helium gas number density was higher at lower T_a. The outer chamber was evacuated by a scroll pump (nXDS15i, EDWARDS) and worked as a vacuum heat insulating layer. T_a was measured by a platinum resistance thermometer, which was set at a distance of about 20 mm from the region of discharge plasmas. Sapphire optical windows on the upper side of the reactor allowed optical access to the inner chamber. Probing laser beams for laser measurements were introduced through these windows.

The helium pulsed discharge plasmas were generated using a function generator (WF1974, NF) and a high voltage amplifier (HVA4321, NF) with a frequency of 10 kHz. Typical waveforms of an applied voltage and a discharge current are shown in Fig. 2.2. The current was a unipolar pulse with a pulse width of about 500 ns. The averaged power consumptions at each T_a condition in pulse cycle were calculated to be 248, 282, 297, 524, 662 and 831 mW for T_a = 340, 300, 250, 200, 150 and 100 K, respectively, by time integration of the product of the discharge current and the applied voltage. A higher power was necessary at lower T_a to sustain discharges because of the higher gas number density at lower T_a. The input of the voltage was alternately turned on and off, with voltage on in 1.8 ms and off in 1.2 ms, in order to relax T_g. A 10 Ω non-inductive resistance (FHN60, PCN) was connected to the grounded electrode to measure the

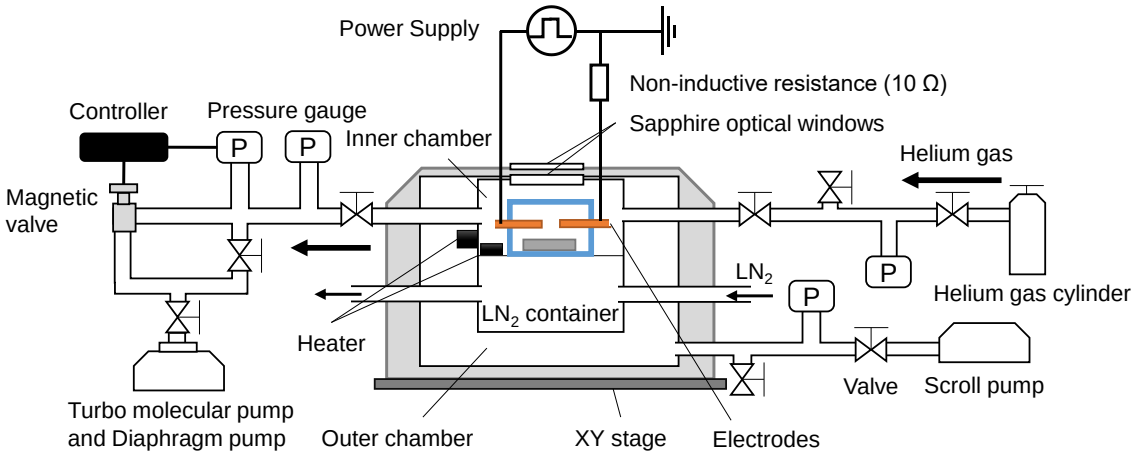

Figure 2.1 Setup for the generation of the helium pulsed discharge plasmas.

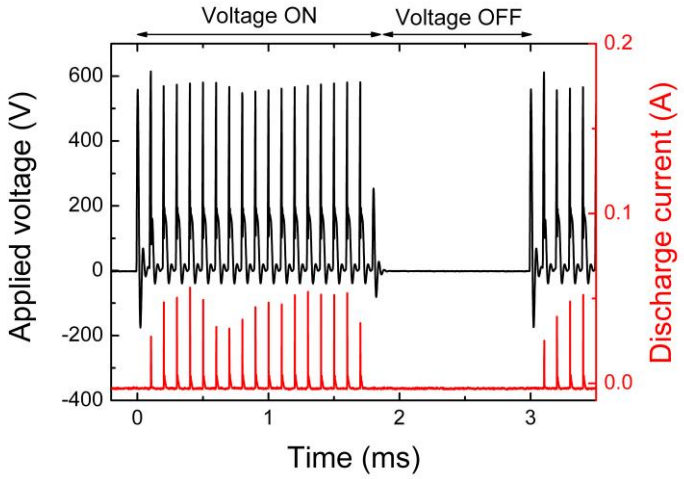

Figure 2.2 Voltage and current at T_a = 300 K. The applied voltage and the discharge current in one cycle of voltage-on (1.8 ms) and voltage-off (1.2 ms) are presented.

discharge current. A high-voltage 100:1 passive probe (400 MHz, ss-0170R, IWATSU) and a low-voltage 10:1 probe (500 MHz, N28 90A, Agilent) which were both connected to a 1 GHz oscilloscope (WaveRunner 610Zi, Teledyne LeCroy) were used to measure the voltages between the gap of the electrodes and between the non-inductive resistance, respectively.

2-1-2. Theoretical description of near-infrared laser heterodyne interferometry

Laser interferometry is a method for measuring the change in refractive index of a tested plasma source by detecting the phase shift ($\Delta\theta_{plasma}$) of the probing laser beam passing through the plasma [98]. $\Delta\theta_{plasma}$ is generated by the change in electron and gas number densities (n_e and n_g) due to plasma generation. Whereas this method has been widely used to measure electron density in plasma science and technology research [99–101], we used NIR-LHI to measure the variation of the n_g (Δn_g) and evaluate the variation of T_g ($\Delta T = T_g - T_a$) due to plasma generation. The NIR probing laser allows the detection of both n_e and Δn_g in high-density medium including at atmospheric pressure [96, 97]. $\Delta\theta_{plasma}$ can be expressed as follows, with $\Delta\theta_{ele}$ and $\Delta\theta_{gas}$ being related to n_e and n_g, respectively [98].

$$\Delta\theta_{plasma} = \Delta\theta_{ele} + \Delta\theta_{gas} = -\frac{e^2\lambda}{4\pi\varepsilon_0 m_e c^2}\int_0^L n_e dl + \frac{2\pi}{\lambda}A\left(1+\frac{B}{\lambda^2}\right)\int_0^L \frac{\Delta n_g}{n_{go}}dl \quad (2.1)$$

Here, e is the elementary charge, λ is the wavelength of the probing laser beam, ε_0 is the permittivity of a vacuum, m_e is the electron mass, c is the speed of light, L is the total plasma length along the probing laser path, A and B are constants depending on the gas species [102], n_{go} is the gas number density when a plasma is not generated, and l is the position along the path of the probing laser beam in the discharge plasmas. In this study, we regarded the l integral of Δn_g as the product of L and Δn_g, i.e., the calculated Δn_g is an averaged value along the laser path. Thus, $\Delta\theta_{plasma}$ is expressed as follows.

$$\Delta\theta_{\text{plasma}} = \Delta\theta_{\text{ele}} + \Delta\theta_{\text{gas}} = -\frac{e^2\lambda}{4\pi\varepsilon_0 m_e c^2} n_e L + \frac{2\pi}{\lambda} A\left(1+\frac{B}{\lambda^2}\right)\frac{\Delta n_g}{n_{go}} L. \qquad (2.2)$$

ΔT due to plasma generation can be calculated from the measured Δn_g, using the equation of state and assuming an ideal gas. Just after a discharge pulse, the detected signals will contain both n_e and Δn_g components. For example, when $n_e = 2.0 \times 10^{15}$ cm^{-3}, $\Delta n_g = 8.0 \times 10^{17}$ cm^{-3}, and $L = 1.65$ mm, where Δn_g corresponds to $\Delta T = 10$ K at $T_a = 298$ K at atmospheric pressure under the assumption of an ideal gas, and L corresponds to the experimental condition of this study, $\Delta\theta_{ele}$ and $\Delta\theta_{gas}$ are = −0.83° and = −0.43° (corresponding to = -2.15×10^{-6} and = -1.13×10^{-6} changes in the refractive index), respectively. Since n_e decays more rapidly in a few μs than n_g after a discharge pulse [97], only the Δn_g signal is detected a few μs after a discharge pulse. In almost all of the time regions except within10 μs or so just after the discharge pulse, it is appropriate to assume that the detected $\Delta\theta_{plasma}$ is attributable to $\Delta\theta_{gas}$. Therefore, in this study, $\Delta\theta_{plasma}$ was approximated by Eq. (2.3), except within about 10 μs just after a discharge pulse:

$$\Delta\theta_{\text{plasma}} \approx \Delta\theta_{\text{gas}} = \frac{2\pi}{\lambda} A\left(1+\frac{B}{\lambda^2}\right)\frac{\Delta n_g}{n_{go}} L. \qquad (2.3)$$

From the $\Delta\theta_{plasma}$ data detected by the NIR-LHI measurements, ΔT was calculated based on Eq. (2.3) under the assumption of an ideal gas. In Eq. (2.3), the term of $A(1 + B/\lambda^2)\Delta n_g/n_{g0}$ corresponds to the change in the refractive index of helium gas by ΔT due to the generation of discharge plasmas, and the change in refractive index is the square root of the change in permittivity, with the permeability assumed to be a constant value of 1. Referring to the REFPROP [103] database for the temperature dependence of the permittivity of helium gas, Δn_g was calculated and subsequently ΔT was evaluated using the equation of state of an ideal gas.

2-1-3. Optical setup for near-infrared laser heterodyne interferometry

The optical system for the NIR-LHI measurements was constructed as shown in the left-hand side of Fig. 2.3. The fundamental setup of the system was the same as that described in [97], except for the wavelength of the probing laser and no usage of a microscope. For the probing laser, an external cavity diode laser with a wavelength of 1550 nm (TEC150, Sacher Lasertechnik) was used in this study.

In what follows, the detail of the optical setup is described, which is same as in [97]. The optical 110 MHz modulation of the phase of the NIR-LHI system was conducted by an acousto-optic modulator (AOM, TEM-110-25-890, Brimrose), and the laser light was split in two lights, 0th and 1st order light. In the AOM, a traveling sound wave acts as a moving diffraction grating and the frequency of the shifted beam is displaced by the sound wave frequency. While the 0th order light was for reference light, the 1st order light was for the probing beam and passed through the tested discharge source. The 1st order beam was introduced to the reactor, reflected by the mirror behind the electrode and returned in the reverse direction. Therefore, the beam passed through the discharge region twice before and after the reflection. This reflective configuration was adopted because the reactor had only one optical window in the upper part. In the whole system, the polarization of the beam was controlled, by suppressing the attenuation of the

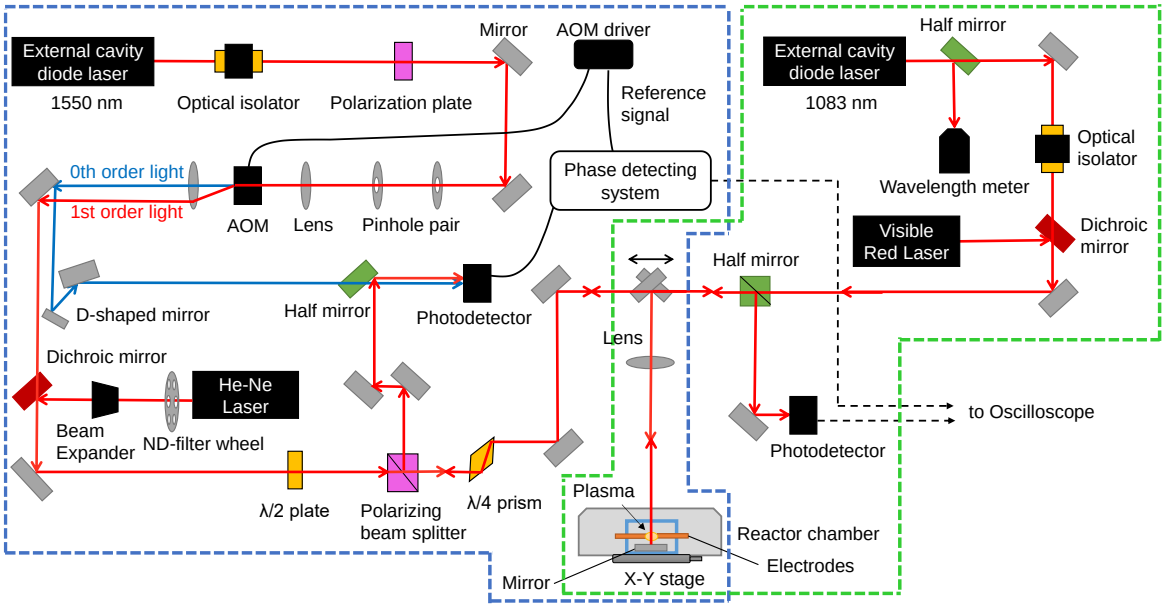

Figure 2.3 Schematic of the optical setup for the NIR-LHI and LAS measurements. The left side (inside blue dash lines) indicates the optical setup for the NIR-LHI measurements and the right side (inside green dash lines) for LAS measurements. The red arrows indicate the path of the probing laser beams. In the NIR-LHI setup, after passing through an acousto-optic modulator (AOM), the blue arrow represents the 0th order light beam and the red arrow is 1st order light beam with a He-Ne visible laser. Because the reflective configuration was adopted, the probing lasers passed through the discharge plasmas twice. The mirror above the reactor chamber was turned over according to the NIR-LHI or LAS measurements. The details of each element are same as those in [30, 97].

beam by using a polarization plate (LPVIS050-MP, Thorlabs), a half-wavelength plate (AHWP05M-980, Thorlabs), a polarization beam splitter (PBS, CM1-PBS252, Thorlabs) and a quarter-wavelength Fresnel rhomb prism (FR600QM, Thorlabs). The 0th and 1st laser beams were merged at the half mirror and formed a beat with the frequency of 110 MHz, and this beat signal was measured by an amplified silicon photodetector (PDA10A-EC, Thorlabs) with a 150 MHz. The phase of the detected signal was compared with that of an AOM driving reference signal in a phase detecting system (Fig. 2.4). The outputs of the phase detecting system, sine and cosine of the phase, were recorded by a digital oscilloscope (WaveRunner610Zi, Teledyne LeCroy).

NIR-LHI is very vulnerable to environmental disturbance because they also change the refractive index along the laser path. Therefore, removal of environmental disturbance is very critical to obtain better signal to noise ration. In this experiment, the NIR-LHI setup was constructed on a vibration isolation table and covered with plastic plates to prevent from environmental disturbance such oscillation and ambient air flow. Furthermore, the vacuum pumping system was stopped during the measurement of NIR-LHI.

2-1-4. Experimental approach for laser absorption spectroscopy

In the same helium pulsed discharge plasmas where ΔT was measured by the NIR-LHI measurements, LAS measurements were conducted at each T_a condition. LAS is a method for measuring the number of

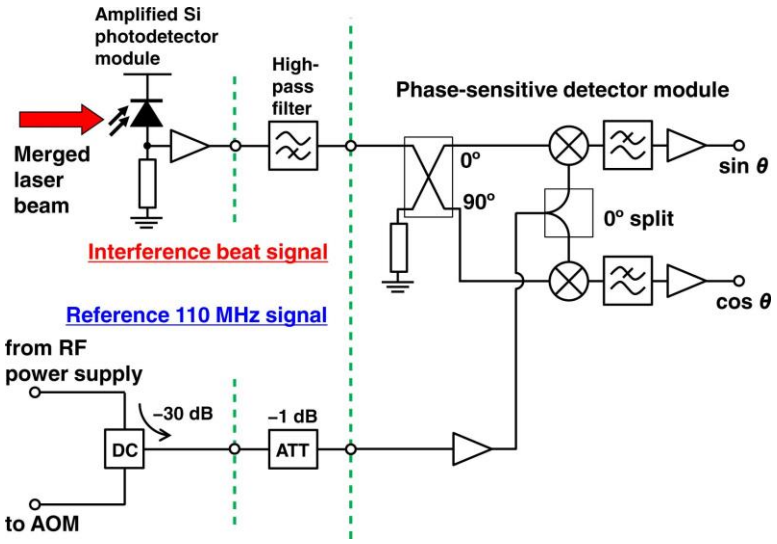

Figure 2.4 Signal flow diagram of phase detecting system. DC, directional coupler; ATT, attenuator. Adopted from [97] with the permission of Institute of Physics Publishing.

non-emitting excited species by passing a probing laser through a plasma source. In this study, the LAS measurements were performed to measure the density (n_m) and the lifetime (τ_m) of metastable helium atoms in the 2^3S_1 level (He^m), which make a large contribution to chemical reactions in plasmas.

In the LAS measurements, a diode laser beam with a wavelength of 1083 nm, which corresponded to the 2^3S_1–2^3P_J (J = 0, 1, 2) transition, was used for the probing laser beam (Fig. 1.8). The optical setup for the LAS measurements is shown in the right-hand side of Fig 2.3, which is same as in [30]. The absorbance $-\ln[I(\nu)/I_0(\nu)]$, where $I(\nu)$ and $I_0(\nu)$ are respectively transmitted and incident intensities of the probing laser beam and ν is the frequency of the probing laser beam, is proportional to n_m as a line-averaged value along the laser path, as described below in detail. The time evolution of n_m was calculated by that of the absorbance, and τ_m was calculated in the afterglow as the time for 1/e decay. τ_m is discussed in terms of gas temperature.

2-1-5. Theoretical description for the calculation of the density of metastable helium atoms in laser absorption spectroscopy

The details of the n_m calculation from the LAS measurements are described here, which are fundamentally same as described in the previous study [30]. In the measurements, a diode laser beam with a wavelength of 1083 nm, which corresponded to the 2^3S_1–2^3P_J (J = 0, 1, 2) transition, was used. The details of the wavelengths and the corresponding frequencies are 1082.909 nm and 276840 GHz for J = 0, 1083.025 nm and 276810 GHz for J = 1, and 1083.034 nm and 276808 GHz for J = 2 [104]. The beam was absorbed in the discharge in response to the excitation of He^m to 2^3P_J levels. The absorbance, which was measured by the LAS measurements, are expressed in Eq. (2.4) by Lambert-Beer Law,

$$-\ln\left(\frac{I(\nu)}{I_0(\nu)}\right)=\int_0^L k(\nu,l)dl \qquad (2.4)$$

where $I_0(\nu)$ is the incident laser beam intensity, $I(\nu)$ is the intensity of the transmitted one, ν is the frequency of the probing laser, l is the position along the path of the probing laser beam in the discharge plasmas, and k is sum of the three absorption coefficients $k_J(\nu,l)$ corresponding to each 2^3S_1–2^3P_J (J = 0, 1, 2) transition. This $k_J(\nu,l)$ is proportional to the statistical weight $g_{2,J}$ of the 2^3P_J (J = 0, 1, 2) level, $g_{2,J}$ = 1, 3 and 5 for J = 0, 1 and 2, respectively. Therefore, for any J,

$$\int k_J(\nu,l)d\nu = \frac{g_{2,J}}{\sum_{J=0,1,2} g_{2,J}} \int k(\nu,l)d\nu \tag{2.5}$$

By scanning the absorbance with changing ν, $n_m(l)$ was calculated as Eq. (2.5), using Eq. (2.4).

$$n_m(l) = \frac{8\pi\nu^2}{c^2}\frac{g_1}{g_{2,J}}\frac{1}{A_{21}}\int k_J(\nu,l)d\nu = \frac{8\pi\nu^2}{c^2}\frac{g_1}{\sum_{J=0,1,2} g_{2,J}}\frac{1}{A_{21}}\int k(\nu,l)d\nu \tag{2.6}$$

$n_m(l)$ is the density of He^m at the position of l, g_1 = 3 is the statistical weight of the lower (2^3S_1) level and A_{21} = 1.0216×10^7 Hz is the Einstein A coefficient related to the rate of spontaneous emission from the upper to the lower level [104]. Integrating both sides of Eq. (2.6) with l, and using Eq. (2.4),

$$\int_0^L n_m(l)dl = \frac{8\pi\nu^2}{3c^2}\frac{1}{A_{21}}\int\left[-\ln\left(\frac{I(\nu)}{I_0(\nu)}\right)\right]d\nu. \tag{2.6}$$

The absorbance was scanned by changing the wavelength of the probing laser from 1082.80 nm to 1083.25 nm. Under the assumption of an ideal situation where the gas composition is uniform and the absorption line profile does not change along the laser path, the ratio of the absorbance at specific ν to the integral of the measured absorbance can be expressed as $C(\nu)$, as a function of ν [105].

$$\int\left[-\ln\left(\frac{I(\nu)}{I_0(\nu)}\right)\right]d\nu = C(\nu)\left[-\ln\left(\frac{I(\nu)}{I_0(\nu)}\right)\right]. \tag{2.7}$$

$C(\nu)$ was determined from the absorbance measured by scanning with ν. As shown in Eq. (2.7), $n_m(l)$ can be calculated with an absorbance measured at any arbitrary ν, and the absorbance is proportional to the line integral of $n_m(l)$ along the laser path.

In the LAS measurements, similar to the case of the NIR-LHI measurements, we regarded the l integral of $n_m(l)$ as the product of L and n_m, i.e., n_m is a line-averaged He^m density along the laser path. Thus, n_m can be regarded as being proportional to the measured absorbance.

$$n_m = \frac{8\pi\nu^2}{3c^2A_{21}L}C(\nu)\left[-\ln\left(\frac{I(\nu)}{I_0(\nu)}\right)\right]. \tag{2.8}$$

In this study, the absorbance profile at t = 1.225 ms, which was the time corresponding to the beginning of the second He^m decrease, was fitted by a Voigt function, and the composition of the Gauss broadening at the same time was assumed as solely Doppler broadening calculated by the T_g estimated from the NIR-LHI measurements. As an example, the experimental wavelength-scanned absorbance data and the fitted profile at T_a = 300 K are shown in Fig 2.5. Subsequently, on the assumption that $C(\nu)$ was constant relative to time,

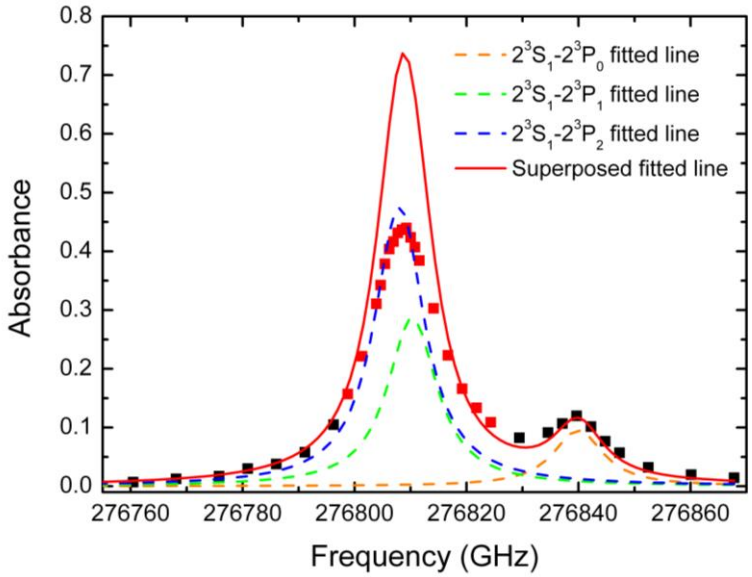

Figure 2.5 Absorbance and the fitted Voigt profile at T_a = 300 K. The measured data (black and red square dots) at t = 1.225 ms and the fitted red line are shown. The red dots were ignored in the fitting because of the saturation of the absorption. The red fitted line is superposition of three fitted lines corresponding to each 2^3S_1–2^3P_J (J = 0, 1, 2) transition. The broadening of the Gaussian and Lorentzian ($\Delta\nu_G$ and $\Delta\nu_L$) of the fitted Voigt function are 1.83 GHz and 10.4 GHz, respectively.

the time evolution of n_m was obtained by temporal absorbance as shown in Eq. (2.8).

The saturation of the absorption occurred at the peaks of J = 1 and 2 in all T_a conditions, resulting in the deviation of a superposed fitted line from the scanned data, shown as red squares in Fig 2.5. Two causes can be considered for this saturation: an excessively high intensity of the probing laser beam or an excessively high n_m. Since no difference of the absorbance was observed when decreasing the laser power, the cause of the saturation was not the high intensity of the probing laser. On the other hand, the degree of the saturation decreased in accordance with the decrease in n_m over time. Therefore, in our case, the saturation was attributed to an excessively strong absorption because of an excessively high n_m. The long laser path resulting from the reflective configuration of the LAS system (Fig. 2.3) was also a factor of too much absorption. In order to avoid inaccuracies due to the saturation of the absorption, the absorbance data at the wavelength of 1082.870 nm (corresponding to 276857 GHz), which is near the non-saturated peak at J = 0, were chosen to calculate the time evolution of n_m.

2-2. Results

2-2-1. Generation of pulsed discharge plasma

At each T_a between 100 and 340 K, helium pulsed discharge plasmas were generated. A photograph of the discharge plasmas is presented in Fig. 2.6. The probing laser beams for the NIR-LHI and LAS measurements were introduced at the center of the discharge gap. In all T_a conditions, the shape of the discharge plasmas was almost the same. The discharge plasmas were axially symmetric with respect to the electrodes, but the diameters were not uniform, having a wider diameter on the anode side and a narrower diameter on the cathode side. At the middle of the discharge plasmas where the probing laser for the laser measurements passed, the diameter was evaluated to be 825 μm as described below, therefore L = 1.65 mm was used in the calculation of ΔT_g and n_m.

2-2-2. Evaluation of the diameter of pulsed discharge plasma

The information obtained directly by laser measurements was the line-integrated values along the laser path. At the NIR-LHI measurements, $\Delta\theta_{gas}$ corresponded to the product of Δn_g and L, and the absorbance was related to that of n_m and L at LAS measurement. Therefore, in order to calculate Δn_g or n_m, the laser path L, or the diameter of the discharge D ($D = L / 2$), had to be decided as can be seen in Eq. (2.3) and Eq. (2.8). In what follows, D in the middle of the gap (along the white arrow in Fig. 2.6), where the probing laser beams of the NIR-LHI and LAS measurements were introduced, was estimated.

At first, the diameter was estimated from the radial distribution of the emission intensity of the photograph. The distribution of the emission intensity was fitted by a Gaussian function. The full width at half maximum was 825 μm, and we chose this value as D.

This estimated D was in good agreement with the result of the space-resolved scanning measurements of NIR-LHI and LAS along the radial direction in the middle of the gap. The Abel inversion shown in Eq. (2.9) can transform an experimentally observed line-integrated value $I(y)$ to the local value $g(r)$ at each position r, in the case that the quantities are cylindrically symmetric [106].

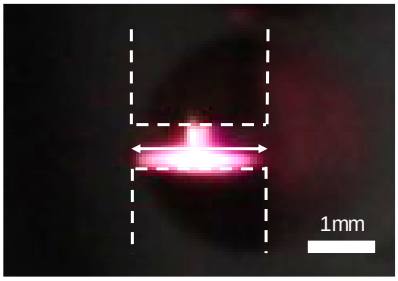

Figure 2.6 Photograph of the helium pulsed discharge plasmas at T_a =300 K. The white dashed lines indicate the outlines of the copper rod electrodes. The probing laser beams were introduced at the center of the gap. The space-resolved scanning measurements of NIR-LHI and LAS were also conducted at T_a =300 K at the middle of the gap along the y-axis indicated by the white arrow.

$$g(r) = -\frac{1}{\pi}\int_r^R \frac{dI(y)}{dy}\frac{1}{\sqrt{y^2 - r^2}}dy \qquad (2.9)$$

Here, R is the cylindrical radius where $I(y)$ converges to zero. In order to know the radial distribution of Δn_g and n_m at the middle of the gap, the Abel inversion was applied to the scanning data of the NIR-LHI and LAS measurements at T_a = 300 K, and the results are shown in Fig. 2.7. For D = 825 μm (radius was 412.5 μm), the normalized signals of the Abel inversion of $\Delta\theta_{gas}$ and the absorbance were small enough for the defined diameter D to cover almost all of the discharge range where ΔT_g and the He^m generation occurred. This means that the defined D value was reasonable for the calculation of Δn_g or n_m.

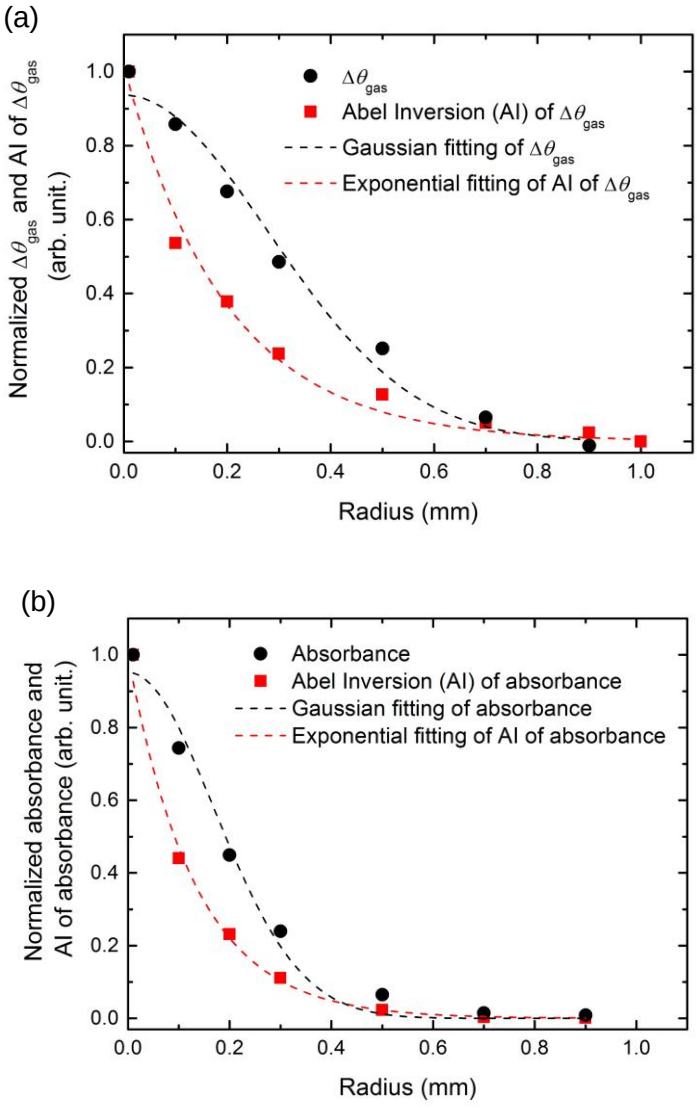

Figure 2.7 (a) Radial distribution of normalized signals of the $\Delta\theta_{gas}$ and its Abel inversion and (b) Radial distribution of normalized signals of the absorbance and its Abel inversion. The black dots are scanning measurement values of (a) $\Delta\theta_{gas}$ or (b) absorbance, and the red dots are the Abel inversion of the measured dots. As a guide, Gaussian and exponential fittings are added to the measured data and the results of Abel inversion, respectively.

In this study, we calculated Δn_g and n_m using $L = 2D = 1.65$ mm. Since the shape of the discharges was similar for all T_a, D at $T_a = 300$ K was estimated, and the estimated D value was used for all T_a conditions.

2-2-3. Fundamental interpretation of measured signals

With regard to the generated discharge plasmas, changes in refractive index and absorbance were obtained by the NIR-LHI and LAS measurements, respectively, as shown in Fig. 2.8. In what follows, when discussing the measurement results for one pulse, we chose the results of the pulse at t = 1.20–1.30 ms after the voltage was turned on, as a typical example. After the breakdown of a pulsed discharge plasma, a voltage of about 200 V was sustained for 20–25 μs and a small discharge current around 10 mA was maintained. In the same region, generation of He^m was sustained due to the sustained voltage and small current, which can be seen as sustaining absorbance. This sustainment was longer at higher duty ratios, i.e., higher power consumption. As mentioned in chapter 2-1, a higher power was necessary to maintain the discharge plasmas at lower T_a, and this led to n_m being sustained for linger at lower T_a.

In the change in refractive index measured by the NIR-LHI measurements, small oscillations were observed over the entire measurement period. They were noises that were not related to the signals and not removable, resulting in an error of 5 K at the maximum. One possible way to remove the noises is to use a lock-in amplifier. At the beginning of the discharge pulse there were also a few strong oscillations. It was

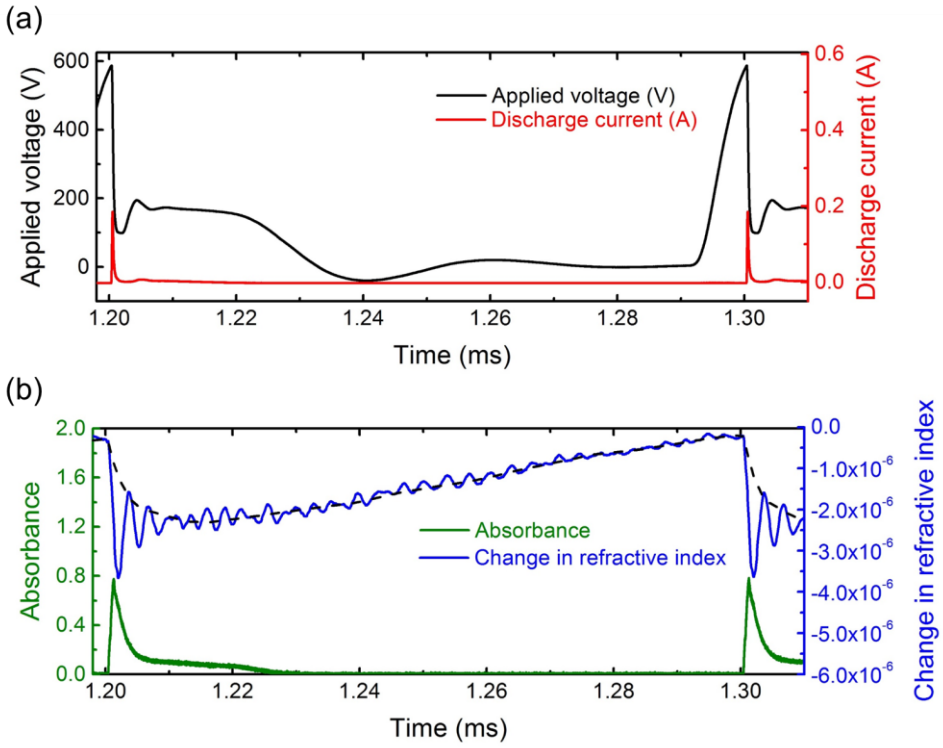

Figure 2.8 Typical results for (a) applied voltage and discharge current and (b) absorbance and change in refractive index, at T_a = 300 K. The typical data for one pulse obtained by the measurements are exhibited. The voltage was sustained at t = 1.205–1.225 ms, resulting in n_m being sustained. The dashed curve added on to the change in refractive index indicates a rough guide of the signals due only to ΔT, subtracting the contribution from n_e.

suspected that they were caused by the n_e signal in addition to ΔT because electrons are generated during the discharge pulse, as shown by the current peak, and they decay in a time scale of less than 10 μs [97]. In this study, because we compared the decay of He^m in the afterglow region, the overlap of the n_e and ΔT signals at the time of the pulsed discharge does not directly affect the following results. Of course, the n_e and ΔT signals have to be divided when using the data in the pulsed discharge region. To give an indication, a change in the refractive index of -2.0×10^{-6} corresponds to $n_e = 1.9 \times 10^{15}$ cm^{-3}, calculated by Eq. (2.3). A rough guide of the signals due only to ΔT, subtracting the n_e contribution and the noise, are also presented in Fig. 2.8.

2-2-4. Evaluation of gas temperature

The time evolution of ΔT at each T_a was evaluated from the result of the NIR-LHI measurements, and ΔT at T_a = 100, 200 and 300 K is shown in Fig. 2.9 and Fig. 2.10. Note that in the calculation all $\Delta\theta_{plasma}$ signals were regarded to be a result of ΔT (i.e., the exhibited ΔT was calculated using Eq (2.3)), while n_e signals were also composed just after the discharge pulse, as mentioned above. At an arbitrary time, T_g was defined as the sum of T_a and ΔT ($T_g = T_a + \Delta T$). Fig. 2.9 shows ΔT for about one cycle of voltage on (1.8 ms) and off (1.2 ms). While the voltage was on, ΔT relaxed to a certain ΔT value of ΔT_1, and ΔT can be divided into ΔT_1 and ΔT_2, which is further temperature increase from ΔT_1 ($\Delta T_2 = \Delta T - \Delta T_1$). ΔT_1 is temperature change from T_a to the steady temperature during voltage on, and ΔT_2 is further temperature change corresponding to the pulse. ΔT_2 for one discharge pulse at T_a =100, 200 and 300 K is shown in Fig. 2.10. In this way, $T_g = T_a + \Delta T_1 + \Delta T_2$. For example, the maximum ΔT was 47 K at T_a = 300 K with a power consumption of 282 mW.

Strictly, T_g at ΔT = 0 K (dashed baseline at ΔT = 0 K in Fig. 2.9) was not T_a but a steady temperature (T_a') in the system of voltage on and off. Decay of T_g in a period of voltage off was considered to be driven by the temperature difference between T_g and T_a. If the next voltage signal were not turned on, T_g would relax to T_a. While T_g did not completely relax in a period of voltage off as can be seen in Fig. 2.9, T_g decayed exponentially, and the difference between T_a and T_a' was estimated less than 0.5 K by exponential

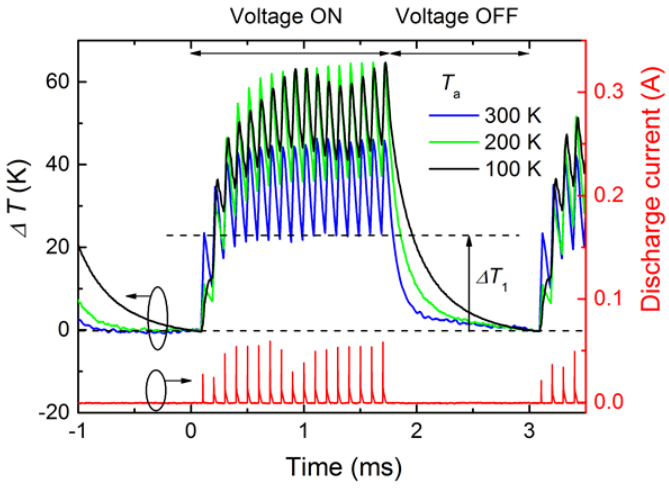

Figure 2.9 ΔT at T_a = 100, 200 and 300 K. The discharge current and ΔT_1 at T_a = 300 K are also shown.

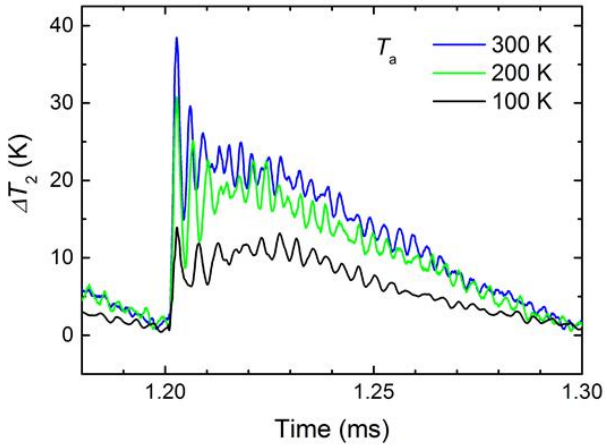

Figure 2.10 ΔT_2 at T_a = 100, 200 and 300 K. This figure indicates ΔT_2, a detail of one discharge pulse in Fig. 2.9. ΔT_2 = 0 K corresponds to $T_g = T_a + \Delta T_1$.

fitting of the T_g decay in a period of voltage off. This difference was within an error of T_a by PID control. Thus, in this study, we conducted evaluation of T_g under the assumption that T_g at ΔT = 0 K (T_a') was regarded as T_a within an error of 0.5 K.

2-2-5. Evaluation of density and lifetime of metastable helium atoms

The time evolution of n_m was obtained by the LAS measurements as shown in Fig. 2.11. At T_a = 300 K n_m reached the maximum, i.e., 1.2 × 10^{14} cm^{-3}, then showed a steep decrease, a period of stability and a second decrease. The stable n_m was caused by sustained generation of He^m generation due to the sustained voltage and small current at this time region, as described in the chapter 2-2-3. After the period of sustainment, in the second decrease there was supposed to be almost no He^m generation. Here, the lifetime of He^m (τ_m) was defined as the decay time during the second decrease from the beginning of the decrease to the 1/e decay time, compared with the sustained n_m. The results of n_m and τ_m are shown in Fig. 2.12. τ_m was a reasonable value compared with that from [30], but a slightly longer τ_m was observed in this study. One

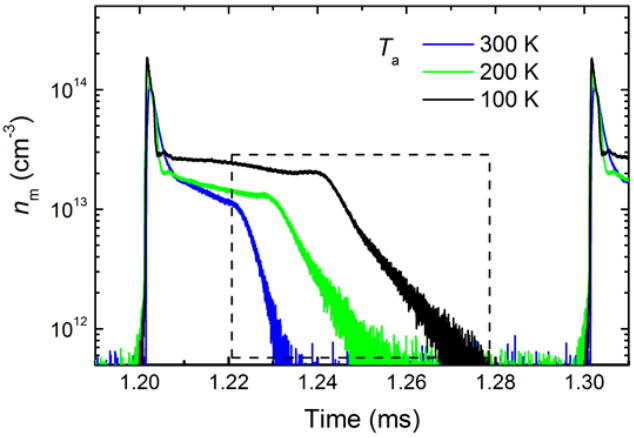

Figure 2.11 Time evolution of n_m at T_a = 100, 200 and 300 K. τ_m was obtained from the slope of the second He^m decrease, as shown inside the dash lines.

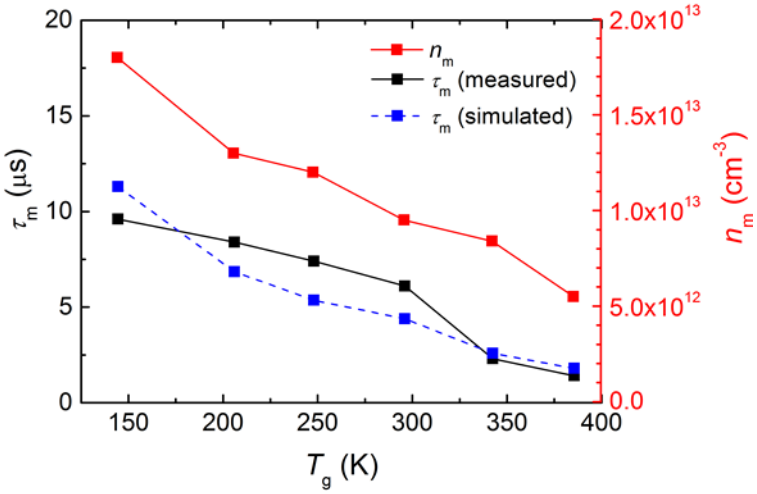

Figure 2.12 T_g dependence of n_m and τ_m. The data points labelled n_m were the values at the beginning of the second He^m decrease. The measured and simulated τ_m are indicated by black points and a line and by blue points and a dotted line, respectively.

possible cause of this difference was considered to be the difference in impurity levels due to the use of different reactors. In our results, τ_m was longer at lower T_g, i.e., τ_m at T_g = 145 K (9.6 μs) was seven times longer than τ_m at T_g = 386 K (1.4 μs). This T_g dependence of τ_m indicated that T_g is a key parameter for chemical reactions involving He^m at around room and cryogenic T_g of 145–386 K, in addition to lower cryogenic T_g [29, 30]. The T_g dependence of the He^m quenching reactions is discussed later in the same manner as in [29, 30].

τ_m, and T_g and n_m at the beginning of the second He^m decay are summarized in Table 2.1 for each T_a conditions.

Table 2.1 Summary of measurement results for each T_a condition

T_a (K)	ΔT_1 (K)	ΔT_2 (K)	ΔT (K)	T_g (K)	n_m (cm^{-3})	τ_m (μs)
340	20	26	46	386	5.5×10^{12}	1.4
300	22	21	43	343	8.4×10^{12}	2.3
250	28	18	46	296	9.5×10^{12}	6.1
200	34	14	48	248	1.2×10^{13}	7.4
150	44	12	56	206	1.3×10^{13}	8.4
100	39	6	45	145	1.8×10^{13}	9.6

Note: the exhibited ΔT_1, ΔT_2, ΔT, T_g and n_m are values at the start of the second He^m decrease.

2-3. Discussion

2-3-1. Gas temperature dependence of quenching reactions of metastable helium atoms

To further investigate the dependence of τ_m on T_g observed in the experiment, a numerical analysis of τ_m was conducted by calculating the mass balance of He^m given by Eq. (2.10), based on our previous studies of helium cryoplasmas [29, 30]:

$$\frac{dn_m}{dt} = \sum_{j=1}^{7} S_{jR} - \sum_{j=1}^{7} L_{jR} - L_W \quad (2.10)$$

where S_{jR} is the He^m generation term for the j-th reaction, L_{jR} is the He^m loss term by j-th reaction, and L_w is the term for other losses. In the af terglow region where τ_m was experimentally calculated, there was assumed to be much less He^m generation compared with collisional quenching reactions, and the main mechanism of loss of He^m is collisional reactions when T_g is around or below room temperature [29]. Thus, we ignored the first and third terms of the right side of Eq. (2.10) and simulated τ_m by assuming only the second term, the loss term for collisional reactions. The effect of T_g was introduced into the reaction rate coefficients, considering collisional factors. Table 2.2 lists the elementary He^m quenching reactions and the dependence of T_g on the reaction rate coefficients assumed in the simulation. For T_g values, the experimentally evaluated T_g from the NIR-LHI measurements was used. The T_g values were those at the starting time of the second decrease in He^m. In this study, phase transitions of impurities in the discharge

Table 2.2 Elementary He^m quenching reactions and corresponding reaction rate constants including T_g terms.

Index	Reaction	Rate constant	Ref.
R1	$He^m + He + He \rightarrow He_2^m + He$	$0.41\times10^{-36}\times\boldsymbol{T_g}\times\exp(-200/\boldsymbol{T_g})$ $+8.7\times10^{-36}\times\boldsymbol{T_g}\times\exp(-750/\boldsymbol{T_g})$	[107]
R2	$He^m + He^m \rightarrow He + He^+ + e$	$1.1\times10^{-19}\times(\boldsymbol{T_g}/10)^{0.167}$ [a]	[108]
R3	$He^m + He^m \rightarrow He_2^+ + e$		
R4	$He^m + N_2 \rightarrow He + N_2^+ + e$	$5\times10^{-11}\times(\boldsymbol{T_g}/300)^{0.5}$	[109]
R5	$He^m + N_2 \rightarrow He + N + N^+ + e$	$1\times10^{-10}\times(\boldsymbol{T_g}/300)^{0.5}$	[110]
R6	$He^m + O_2 \rightarrow He + O_2^+ + e$	$2.6\times10^{-10}\times(\boldsymbol{T_g}/300)^{0.5}$	[108]
R7	$He^m + H_2O \rightarrow He + H_2O^+ + e$	$1\times10^{-10}\times(\boldsymbol{T_g}/300)^{0.5}$	[110]

[a] This reaction rate is the total rate of R2 and R3.

Note: R1 is a three-body collision reaction, R2 and R3 are two-body collisions between He^m species, and R4–R7 are Penning ionization reactions. With regard to the rate constants of the Penning reactions (R4–R7), because only the room temperature rate constants could be found in previous literatures we assumed that rate constants were proportional to $T_g^{1/2}$ because the collision frequencies of two-body reactions are generally proportional to $T_g^{1/2}$ when their collisional cross sections are not dependent on thermal energy [111].

space, such as N_2 and O_2, did not occur except for H_2O because T_a changed over their boiling points (T_a = 100–340 K). Thus, unlike in [30], we can discuss the He^m quenching reactions on the assumption of constant level of impurities, although impurity levels were actually considered to change slightly with T_a. The impurity concentration was chosen so as to enable the best fit of the simulated τ_m to the experimental values. For small amounts of impurities, a 5 ppm air impurity (N_2 and O_2 at a 4:1 density ratio) was considered for all T_a conditions. The H_2O vapor impurity was only considered at T_a = 300 and 340 K, as small amounts of water molecules initially adsorbed on the inner wall of the inner chamber at 50 ppm and 100 ppm, respectively.

The results of the numerical simulation are shown in Fig. 2.13, where the simulated τ_m is plotted along with the experimental ones. Although there were certain differences between experimental and simulated τ_m values, the T_g dependence of the experimental τ_m could be reproduced by numerical simulation. The detailed variations of the mechanism of the He^m quenching reaction are shown in Fig. 2.13, indicating the change in the ratio of elementary reaction rates to the total reaction rate in accordance with T_g. Although three-body collision (R1) was the main quench reaction and He was the main quencher for all T_g, which is consistent with [29], two-body collisions between He^m species and Penning ionizations by N_2 and O_2 occurred more frequently at lower T_g. When T_a was above room temperature, H_2O was a critical quencher. These results indicate that the dependence of τ_m on T_g can be attributed to a change in the total quenching reaction rate due to change in each elementary reaction rate in response to T_g. In this manner, the T_g dependence of He^m quenching reactions was revealed directly by combining the NIR-LHI with the LAS measurements.

2-3-2. For further improvement of near-infrared laser heterodyne interferometry

Time evolution of T_g was not taken into account in this numerical analysis. However, further investigation of chemical reactions by considering time evolution of T_g is possible and desirable. On the other hand, highly accurate control of T_g on the order of 1 K will be required in some cases of plasma

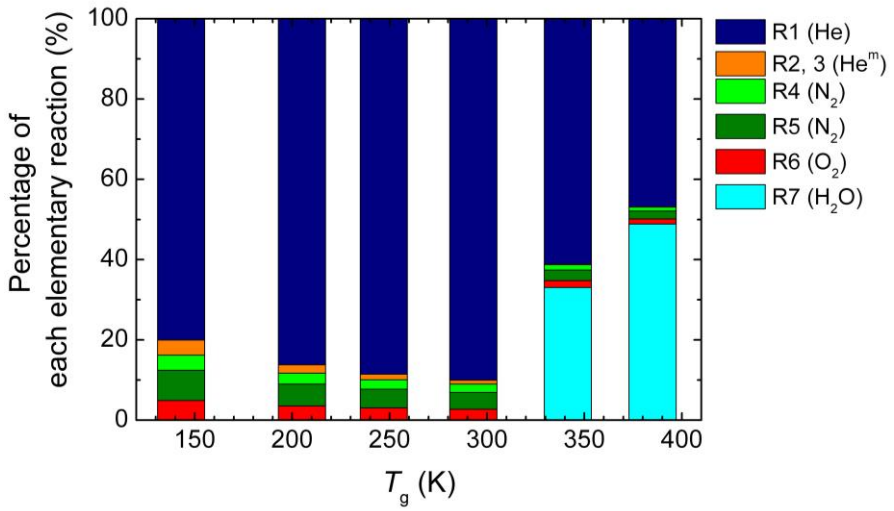

Figure 2.13 Percentage of elementary quenching reactions at each T_g. The quenchers of each reaction are also shown in brackets.

application to biomedicine, because biomolecules such as proteins and DNA will change their structures and lose their functions even a few Kelvin above a thermal denaturation temperature [112, 113]. The accuracy achieved in this study was better than 5.5 K, but this is not sufficient for the evaluation of T_g for elaborate biomedical applications. The resolution of laser interferometry can be theoretically less than 1 K [99], and it is necessary to decrease noise and improve the signal to noise ratio. Furthermore, for better validity of the NIR-LHI measurements as the method of evaluating T_g, comparison with conventional methods such as evaluation of T_g from rotational lines of optical emission spectra [114, 115] should also be performed in the future research.

2-4. Summary

For a better evaluation of T_g and to investigate plasma chemical reactions related to He^m around room and cryogenic temperatures, two types of laser measurements, NIR-LHI and LAS, were conducted in helium pulsed discharges for T_a = 100–340 K. The NIR-LHI measurements were performed to evaluate T_g. The time evolution of T_g was evaluated with an accuracy of 5.5 K, and the maximum ΔT was 47 K at T_a = 300 K for a power consumption of 282 mW. For the same discharge plasma sources in which NIR-LHI measurements were executed, the time evolution of the He^m density was measured by LAS measurements. The He^m density reached 1.2×10^{14} cm^{-3} under the same condition. The He^m lifetime was calculated, and longer lifetimes were found at lower T_g, seven times longer at T_g = 145 K (τ_m = 9.6 μs) than T_g = 386 K (τ_m = 1.4 μs). To investigate the T_g dependence of the He^m lifetime, the He^m lifetime was numerically calculated by assuming elementary He^m quenching reactions and reaction rates that depended on T_g. T_g evaluated by NIR-LHI measurements were employed in the numerical simulation. As a result, the T_g dependence of the He^m quenching reactions in helium pulsed discharge plasmas was quantitatively revealed around room and cryogenic ambient temperatures of T_a = 100–340 K, even though the main quenching reaction was a three-body collision for all T_g. By combining the T_g evaluation from the NIR-LHI measurements with the LAS measurements and numerical calculation, the T_g dependence of He^m-related plasma chemistry was exhibited directly. Therefore, NIR-LHI was revealed to be a promising non-contact measurement method for evaluating T_g in novel non-equilibrium plasma sources such as atmospheric pressure low-temperature plasmas. By improving the setup and signal to noise ratio, NIR-LHI is expected to be used for highly accurate evaluation of T_g in various plasma sources, contributing to further understanding and application of novel non-equilibrium plasmas.

Chapter.3 Generation of plasma-ice interfacial reaction field

Ice is one of the most abundant and important solid components both on earth and in the universe. In particular, the surface of ice provides a unique reaction field and plays a key role in wide research areas of atmospheric environmental chemistry, astrophysics and astrobiology, such as the generation of the ozone hole, formation of amino acids from UV irradiation and quantum-tunneling reactions mediated by hydrogen atoms, as introduced in the chapter 1.2. In these research studies, several kinds of reactive species were generally supplied by light irradiation or discharges away from ice. In atmospheric and astrophysical environments, not only particular species but also electrons, ions and various reactive species could also be totally involved in reactions on ice surface. By placing ice directly in contact with plasma, a plasma-ice interfacial reaction field would provide analogies to such complicated environment, where further reactivity can be achieved by bombardment and adsorption of energetic charged species accelerated electrostatically to the ice surface. Furthermore, self-assembling structures, such as concentrated liquid layer and lamellar structure of ice body, could also be exploited for the development of a novel material processing. Therefore, plasma-ice interfacial reaction filed is expected to provide unique applications in a wide range of scientific and engineering research areas, such as atmospheric science, astrochemistry, material processing, plasma-assisted cryosurgery, and so on. Although a few studies on plasma coexisting with ice were conducted in the research area of dusty plasmas [116, 117], there is no research focusing on plasma-ice interface as a reaction field, as far as we know. It is noteworthy that plasma-ice interfacial reaction field would also provide a new perspective to plasma in contact with liquid and plasma-induced liquid phase reaction field, which have been considerable attention recently. In this chapter, as a first step for developing the plasma-ice interfacial reaction field, we aimed to realize and establish the coexistence system of ice and plasma without melting of ice by controlling plasma gas temperature, as a platform for investigating the plasma-ice interfacial reaction field.

3-1. Experimental approach

In order to realize plasma in contact with ice, plasma with cryogenic gas temperature is indispensable. Here, one suitable plasma source is cryoplasma. A cryo-dielectric barrier discharge (cryo-DBD) was adopted as a plasma source because it can suppress the increase in gas temperature and allows comparatively easy control of gas temperature. H_2O ice was installed as a dielectric barrier, and named the cryo-DBD as "H_2O-ice DBD."

The experimental setup and the electrode for the generation of H_2O-ice DBD are shown in Fig. 3.1. The setup was basically the same as the previous studies of cryoplasma [10]. We used a custom-made cryogenic chamber equipped with a 4 K Gifford McMahon refrigerator (CKW-21, Sumitomo Heavy Industries) [10, 13, 21], as shown in Fig. 1.3. The cryogenic chamber consists of an inner and an outer chamber. Helium gas (purity > 99.99%) was introduced into the inner chamber with 70 sccm flow, keeping the gas number density at $2.4(\pm0.4)\times10^{19}$ cm^{-3}, which corresponds to atmospheric pressure at room temperature. The ambient temperature in the chamber was cooled down to 285–5 K by the refrigerator using the outer chamber as a heat-insulating layer, where the outer chamber was evacuated to 10^{-3} Pa by a dry pumping system. The temperature at a distance of 30 mm from the center of the plasma region was monitored by a silicon diode temperature sensor (DT-470-CU-13-1.4L, Lakeshor), and it was used as an indicator of gas temperature. An electrode with a configuration similar to our cryoplasmas [20, 21] as shown in Fig. 3.1(b) was set in the inner chamber. H_2O-ice was put on a copper ground electrode with a diameter of 15 mm and a thickness of 1 mm, and an indium tin oxide (ITO)-coated glass with a diameter of 10 mm and a thickness of 150 µm was set as a top electrode with a gap distance of 500 µm. ITO-coated glass allows optical observation of plasma through a Sapphire window equipped on the top side of the cryogenic chamber. The H_2O-ice was prepared by cooling purified water (electrical conductivity < 5 µS/cm, 161-08247, Wako Pure Chemical Industries., Ltd.). The purified water was poured onto the copper electrode, and cooled gradually from room temperature to targeted cryogenic temperatures. Thus, H_2O ice in this study was considered to be hexagonal crystalline ice, not amorphous solid water (ASW). A sinusoidal AC voltage of 1–2 kV_{pp} was applied at 10 kHz to the top electrode to generate H_2O-ice DBD.

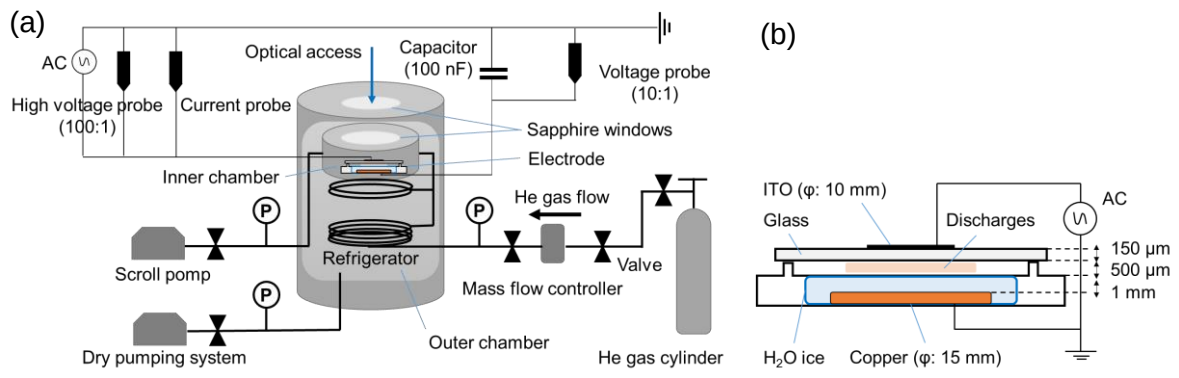

Figure 3.1 (a) Setup for the generation of H_2O-ice DBD, and (b) schematic of the electrode for H_2O-ice

3-2. Results and Discussion

3-2-1. Generation and optical characteristics of H_2O-ice DBD

H_2O-ice DBD was generated reproducibly with a wide range of cryogenic T_g down to 6.5 K, showing color and brightness variations with changing T_g. Figure 3.2 shows photographs of the generated H_2O-ice DBD at T_g = 200, 100, and 40 K. The color change can be explained by optical emission spectra obtained using a spectrometer (USB2000+, Ocean Optics), which exhibited drastic variations with changing gas temperature, as shown in Fig. 3.3. At all gas temperature conditions, there were emissions of He atoms. In addition, emissions of N_2 (second positive system) and emissions of N_2^+ (first negative system) due to residual air impurities became prominent at T_g = 200–100 K. When T_g became below the boiling and melting points of air impurities, emissions of He_2 were observed below 40 K. This gas temperature

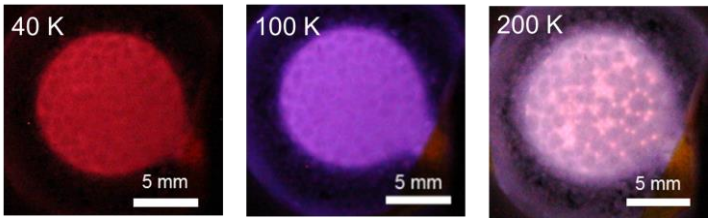

Figure 3.2 Photographs of H_2O-ice DBDs observed through the top electrode at T_g = 200, 100, and 40 K. The applied voltage was 1.85 kVpp operated at 10 kHz. The brightness of the photographs was adjusted at the same rate for clear exhibition. Small dark spots observed all over the discharges represent frozen dew drops on the surface of ITO-coated glass. The glass surface of the top electrode was considered to be covered with ice as well below T_g = 273 K.

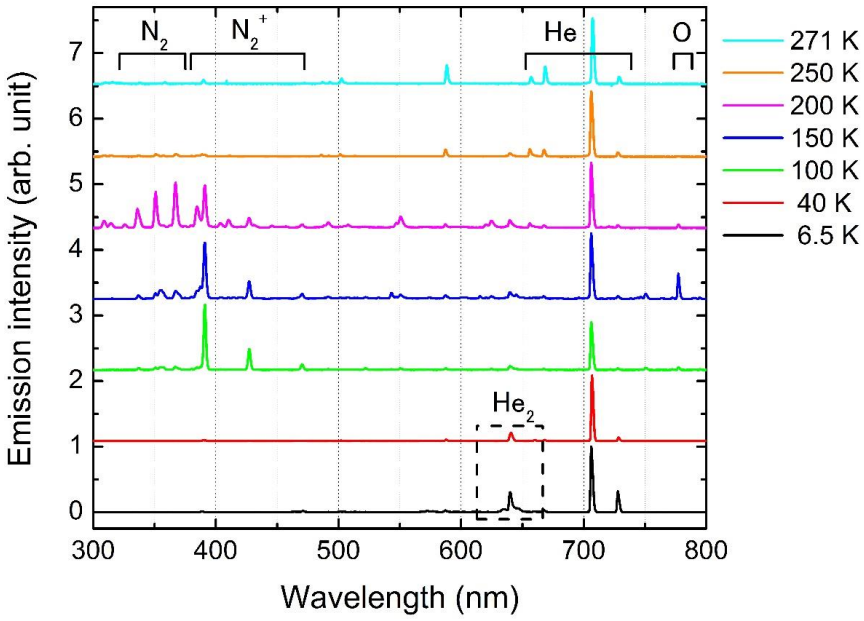

Figure 3.3 Optical emission spectra of H_2O-ice DBD depending on gas temperature. The spectra are normalized by the peak of atomic helium at 706.5 nm.

dependence of the emission spectra has been already reported in our previous studies on helium cryoplasma [13, 21, 118], and is consistent with those results. Therefore, with regard to the plasma gas phase of the discharge, the H_2O-ice DBD was considered to achieve basically the same chemical reactions as in helium cryoplasma without H_2O-ice as a dielectric barrier.

3-2-2. *I-V* characteristics of H_2O-ice DBD

For investigating current–voltage (*I-V*) characteristics of H_2O-ice DBD, current and voltage between the discharge gap were measured by a high voltage probe (ss-0170R, IWATSU) and a current probe (P6022, Tektronix), respectively. Charge was also obtained by measuring the voltage between a probe capacitance of 10 nF, which was inserted between the copper electrode and the ground. At first, transition of discharge mode with changing gas temperature was observed around the melting point of water (273.1 K). The current measured by the current probe is shown in Fig. 3.4(a). Filamentary discharge [119], with a few discharge spikes of 10–60 mA, was observed in a half cycle at T_g = 285 K, in which case, the dielectric barrier of the ground electrode was not solid ice but liquid water. When the gas temperature reached below the melting point of water, thus freezing of the H_2O dielectric barrier, the discharge spikes became drastically weaker, with 5–15 mA at T_g = 270 K, and were no more detected below T_g = 265 K. Power consumption was traced as well around 273 K between 263–297 K, with keeping 1.85 kV_{pp} at 10 kHz as shown in Fig. 3.4(b). Surprisingly, power consumption presented drastic decrease in the vicinity of 273 K, corresponding to the liquid-solid phase transition of water. Although a cause of the decrease in power consumption has not been specified yet and further research is necessary, the temperature response of power consumption around the melting point of water was an evidence of good temperature controllability of H_2O-ice DBD. This result also infer that the control of gas temperature and the temperature of the system could be a valuable new approach for investigating plasma-liquid system as well as plasma-ice system.

On the other hand, to investigate the *I-V* characteristics below T_g = 265 K, discharge current was deduced by measuring charge transfer due to discharges [120], as shown in Fig. 3.5. Below T_g = 200 K, the discharge current had one broad width in one half cycle and became smaller at lower gas temperature down to 6.5 K. The waveform of this discharge current is similar to that of atmospheric pressure Townsend discharge [121]. On the contrary, discharge currents had one or a few continuous spikes with narrow width at T_g = 225 and 250 K, respectively. These discharge currents were similar to atmospheric pressure glow and pseudoglow modes [121–123]. Briefly, filamentary, pseudoglow, glow, and Townsend discharges were observed in this order with decreasing gas temperature.

The transitions of discharge mode depending on gas temperature between 285 and 200 K exhibited basically the same tendency as the helium cryoplasma in our previous studies [21, 27, 28] except for the appearance of filamentary discharge over T_g = 270 K, and the difference in gas temperature of transition from glow to Townsend discharge. The gas temperature dependence of optical emission and discharge mode of H_2O-ice DBD might be attributed to the variation of gas phase plasma chemistry in helium cryoplasma [28], as described in chapter 1.1. Therefore, the existence of H_2O-ice as a dielectric barrier does not seem to have a critical influence on the gas temperature dependence of chemical reactions in plasma

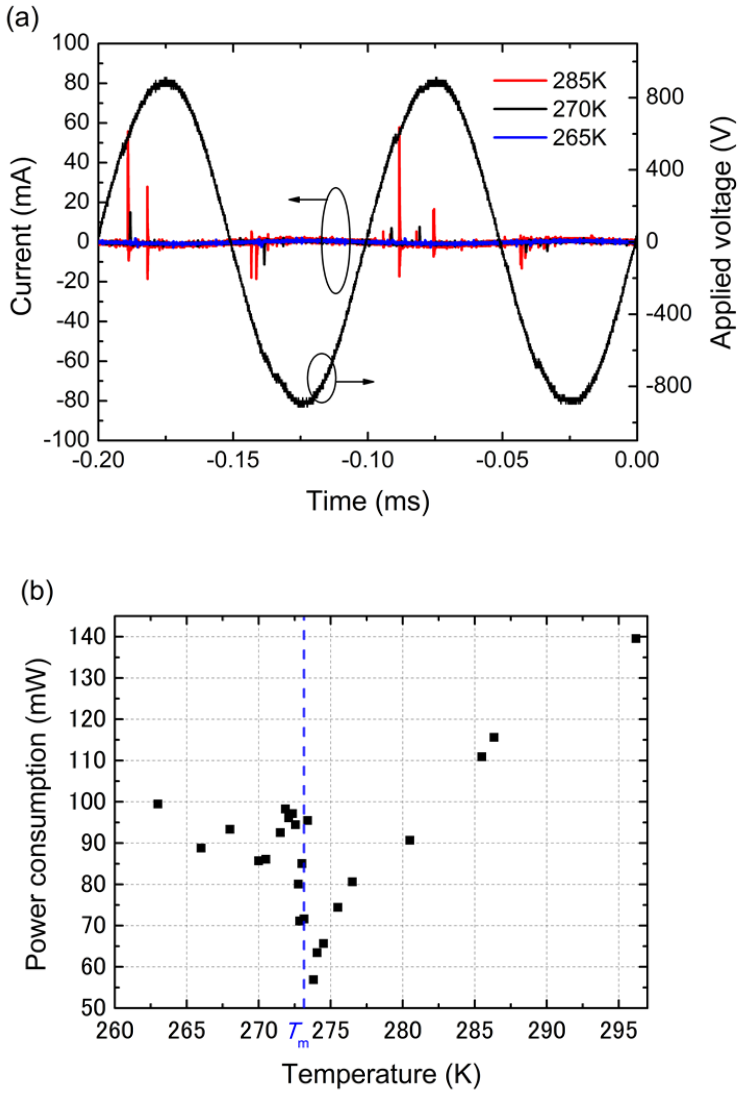

Figure 3.4 (a) Current and applied voltage at T_g = 285, 270, and 265 K with 1.85 kV_{pp} and 10 kHz. The applied voltage is the waveform at T_g = 285 K. (b) Power consumption of H_2O-ice/water DBD with changing T_g in the vicinity of the melting point of water (T_m = 273 K).

gas phase, as in the case of the temperature dependence of the optical emissions. However, as we revealed the drastic variation of the power consumption in the vicinity of the melting point of water, which could provide a new approach to the research of plasma-liquid interface, H_2O-ice DBD should have other uniqueness in plasma gas phase, in bulk ice, or especially on the ice surface interacting with plasma.

3-2-3. Evaluation of reactivity of H_2O-ice DBD

In order to evaluate the reactivity of H_2O-ice DBD as a reaction field, we evaluated electron temperature (T_e), electron density (N_e), and electron flux (Γ_e) because electrons generally govern the reactivity of plasmas [98]. Their values were estimated from the *I-V* characteristics with using the following equations [124].

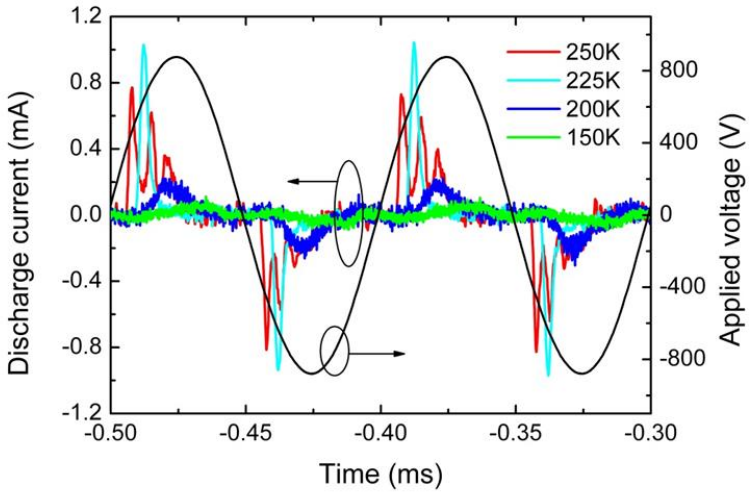

Figure 3.5 Discharge current at T_g = 250, 225, 200, and 150 K with 1.75 kVpp and 10 kHz.

$$\frac{E}{N} = \frac{V_g}{d_g N} \qquad (3.1)$$

$$N_e = \frac{j}{eW} \qquad (3.2)$$

$$\frac{D_e}{\mu_e} = \frac{k_B T_e}{e} \qquad (3.3)$$

Here, E is the electric field between the discharge gap, N is the gas number density, V_g is the voltage between the discharge gap, d_g is the discharge gap (500 μm), j is the current density, W is the electron drift velocity, D_e is the coefficient of electron free diffusion, μ_e is the coefficient of electron mobility and k_B is the Boltzmann constant. Γ_e is defined as division of current density by elementary charge, indicating electron flux going through the electrodes. The electron drift velocity, the coefficient of electron free diffusion and the coefficient of electron mobility were obtained from electron swarm parameters [118, 125, 126], which are functions of the reduced electric field (E/N). The estimation was conducted on the assumption of pure helium, in the case of T_g = 200 K with an applied voltage of 1.75 kV_{pp} as a typical example. In the estimation, peak values of discharge current and the voltage between the discharge gap at that time was used, and permittivity of ice under the applied voltage of 10 kHz was assumed to be a constant value of 3 [127], although permittivity of ice significantly depends on its own and surrounding conditions [127–130]. The nominal reduced electric field, which is the spatially averaged value, was applied as shown in Eq. (3.1), although its distribution is not uniform between the discharge gap. Measuring the distribution of the electric field, which is critical for better estimations, remains to be investigated. For the electron swarm parameters, temperature-dependent simulated values in our previous study [118] were utilized, which were calculated from the two-term approximated Boltzmann equation.

As a result, T_e, N_e and Γ_e were estimated to be 9.1 eV, 8.0 × 10^7 cm^{-3}, and 1.6 × 10^{15} cm^{-2} s^{-1} at T_g = 200 K. The calculated N_e on the order of 10^7–10^8 cm^{-3} is in good agreement with N_e on the order of 10^8–

10^{11} cm^{-3} for a general helium DBD in atmospheric pressure [131–133], when taking account of small current values on the order less than 1 mA and lower pressure at lower gas temperature in this study.

The calculated parameters of H_2O-ice DBD were compared with the study of the formation of amino acids by UV irradiation. We used the energy and flux of UV source in the case of [37] as an example, with the energy of 10 eV for the Lyman α line at 121.5 nm, and the mean flux of photons of 2×10^{15} $cm^{-2}s^{-1}$. In comparison, both T_e and Γ_e of H_2O-ice DBD had comparable values, with higher energy and a little bit smaller or same flux than those in the case of formation of amino acids by UV irradiation. Therefore, H_2O-ice DBD is expected to have sufficient reactivity to provide a unique reaction field on ice surface.

3-3. Summary

H_2O-ice DBD was generated at wide range of cryogenic temperatures down to 6.5 K, with controlling gas temperature as a control parameter. Generation of H_2O-ice DBD was demonstrated with a good temperature control without melting of ice. This was confirmed by the observation of the same temperature dependence of optical emissions and discharge modes as helium cryoplasma. When changing the temperature in the vicinity of the melting point of water, drastic decrease in power consumption corresponding to the phase transition of water was observed. Although the reason of the drastic change has not been understood, it also demonstrates the good temperature control in the generation of H_2O-ice DBD. On the other hand, the H_2O-ice DBD was evaluated to have sufficient reactivity for a novel unique reaction field on the ice surface. Through these observations and evaluations, reproducible generation of plasma-ice interfacial reactions field by controlling gas temperature in plasma was established, which should be a platform for the further development of plasma-ice interfacial reaction field.

Chapter.4 Laboratory simulation of cryogenic astrophysical environment

Although reaction rates are considered to be slow below the melting point or at cryogenic temperature, the ice surface provides the efficient and unique reaction field, as described in the chapter 1-4. By combining the unique reaction filed of the ice surface with the high reactivity of plasma, we can expect the plasma-ice interaction as a novel reaction field at cryogenic environments. To explore possibility of plasma-ice interfacial reaction field as a novel cryogenic reaction field, cryogenic environment in our solar system was simulated by plasma-ice interfacial reaction field.

Low and cryogenic temperature environments spread in the universe, which should contain icy grains and icy planetary bodies. In such an environment, ice bodies are subject to energetic radiations such as cosmic rays, solar wind, and UV, and chemical reactions are proceeded although the temperature is very low. To simulate and investigate the low temperature environments, non-equilibrium plasma is generally used as one of the reasonable techniques. Especially, non-equilibrium plasma can simulate chemical reactions induced by low-energy secondary particles on the order of 1–10 eV which are produced by the interaction of high-energy primary radiations with atmosphere and surface of icy bodies. Although plasma has been widely used to simulate astrophysical environments, gas temperature in plasma was not controlled in most cases. Of course, there were some studies in which gas temperature was cooled by liquid nitrogen for better simulation of temperature. However, continuous control of temperature at low temperatures has not been performed, because there has not been non-equilibrium plasma in which gas temperature is controlled continuously at cryogenic temperatures, even though temperature conditions should have large influence on chemical reactions and phase of substances. To overcome this limitation, plasma-ice interfacial reaction field realized as described in chapter 3 was exploited for further precise experimental simulation of temperature environment of icy bodies in outer solar system.

4-1. Background

4-1-1. Reddish coloration of icy bodies in the outer solar system

Outer solar system, which is the solar system region beyond the asteroid belt, holds many kinds of icy bodies owing to the low temperature condition. As recent advances in exploration technologies, far region of the solar system, including the outer solar system, is attracting much attention for further understanding of the formation of the solar system and the origin of our life. One of the most distinctive features widely observed in some of the outer solar system objects is reddish coloration and its diversity, which is prominent at larger heliocentric distances [90, 134–137]. Figure 4.1(a) shows the reddish coloration of Pluto, Charon, 2014 MU_{69}, and 2007 OR_{10}, as examples of such coloration in the outer solar system. As shown in the histogram of the color index of objects at different regions of the outer solar system in Fig. 4.1(b), ultra-red objects are observed only relatively far from the Sun such as some Centaurs and trans-Neptunian objects (TNOs), whereas Jupiter-family comets (JFCs) such as cometary nuclei and dead comets closer to the Sun lack the reddish coloration [134, 135, 138]. Because there is color diversity among the objects despite both Centaurs and JFCs supposedly originating in TNOs [139, 140], ultra-red color materials have been explained to be sublimated or destroyed according to the change in environmental conditions, as the objects approach from the trans-Neptunian region to the inner solar system [135].

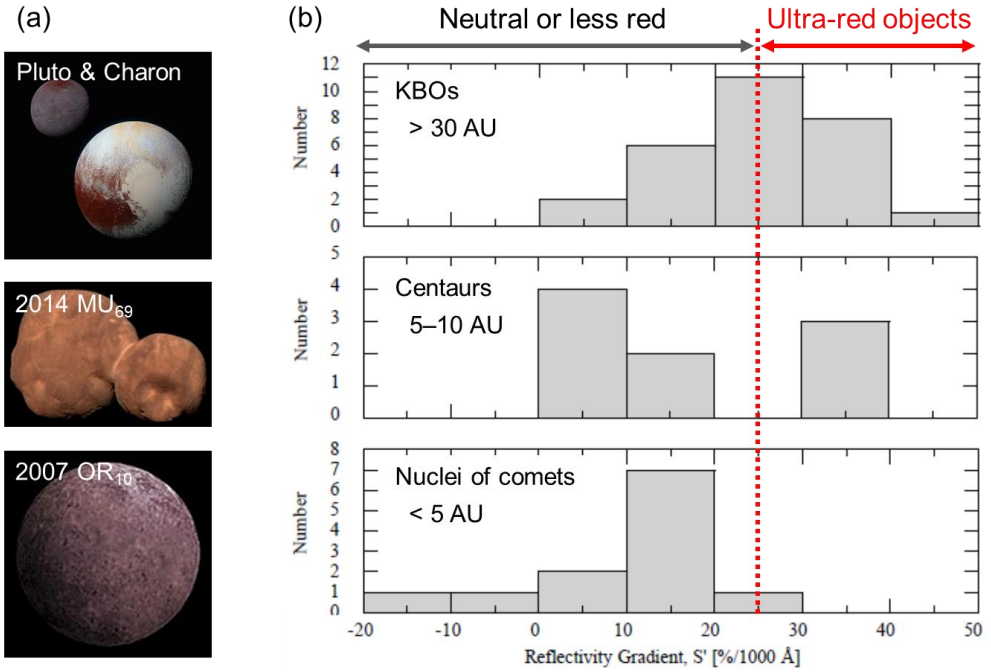

Figure 4.1 (a) Images of some example of Trans-Neptunian objects appearing ultra-red color, Pluto, Charon, 2014 MU_{69}, and 2007 OR_{10}, adopted from NASA. (b) Histograms of reflectivity gradient, *S*' [% $(1000\ Å)^{-1}$], for the different groups of objects in the outer solar system: Kuiper belt objects (KBOs), Centaurs, and comet nuclei. *S*' represents the degree of reddish coloration, where higher *S*' means redder color. Ultra-red objects were defined ones having *S*' > 25 [131]. Adopted from [131] with the permission of Institute of Physics Publishing.

Accordingly, the reddish coloration and its distribution are significant indicator for understanding the formation process of the solar system. Furthermore, it provides astrobiological insights into the origin of life [141, 142].

4-1-2. Explanation for the reddish coloration

The reddish color has been studied extensively in laboratory experiments for the last 40 years or more. For the laboratory simulation of the reddish coloration, many kinds of energetic sources have been used, such as discharge plasma in N_2/CH_3 gas mixture, and irradiation of ice samples by high-energy electron beam, ion beams, and UV photolysis. These laboratory experiments have demonstrated the synthesis of ultra-red solid mixtures. The ultra-red material is highly complicated refractory organic compounds, which is called tholins. The reddish coloration observed in the outer solar system is attributed to the tholins [143–146]. However, the tholin-type materials that have been studied are not volatile even when heated to room temperature. Due to this, explanation of the reddish color distribution is not straightforward. Although some alternative explanations for the reddish color distribution have been suggested [147–149], the color distribution is not fully elucidated and remains debatable [150].

In this chapter, reddish coloration specific to cryogenic temperature in a laboratory experiment is demonstrated, that is distinct from the well-known reddish coloration of the previously reported tholins. For the coloration, cryoplasma was radiated at 85 K on methanol (CH_3OH) and water (H_2O) containing ice by feeding helium (He) with 3% nitrogen (N_2). This study roughly simulated energetic processes in the outer solar system via low-energy secondary species such as UV radiation and charged and/or excited species, which can be formed by primary energetic radiations such as cosmic rays and solar winds [144, 151]. Although ultra-red coloration of TNOs has been experimentally reproduced by ion irradiation of methanol [152], in our study, reddish coloration that is stable only at cryogenic temperatures was obtained, as described below, which is definitively different from the previous study.

4-2. Experimental approach

4-2-1. Cryoplasma irradiation of CH_3OH/H_2O ice

In a custom-made cryogenic chamber equipped with a 4 K Gifford McMahon refrigerator (CKW-21, Sumitomo Heavy Industries), CH_3OH/H_2O ice grown on the top and bottom sides of the electrodes were irradiated with cryoplasma for 12 hours, as shown in Fig. 4.2. The setup for cryopolasma generation is basically same as the H_2O-ice DBD in the last chapter. The top and bottom side of electrodes were composed of 150 μm thick indium tin oxide (ITO; 10mm in diameter) coated glass and stainless steel (16 mm in diameter), respectively, with a gap distance of 500 μm. The CH_3OH/H_2O ice was used as a dielectric barrier to generate the cryoplasma in a dielectric barrier discharge configuration. Experimental procedure is illustrated in Fig. 4.3. To prepare CH_3OH/H_2O ice, a mixture of 200 μL of water (electrical conductivity < 5 μS cm^{-1}, Wako pure chemical industries) and 200 μL of methanol (infinity grade, Wako pure chemical industries) was poured onto the ground electrode. The mixture was cooled at around 0.6 K/min from room temperature to 80 K by lowering the ambient temperature in the chamber. Although the initial mixture had the same volume of CH_3OH and H_2O, the ice on the top electrode might be enriched in the more volatile CH_3OH than H_2O. Three percent N_2 gas (G1 grade) diluted with He gas (G1 grade) was pumped into the inner chamber at a 30 standard cubic centimeters per minute (sccm) flow rate as carrier gas, and the inner chamber was kept at 2×10^3 Pa. To generate the cryoplasma, 1.75 kV_{pp} sinusoidal AC voltage was applied at 10 kHz to the top electrode with a function generator (WF1974, NF) and a high voltage amplifier (HVA4321, NF). The bottom electrode served as a ground electrode. He gas was utilized to stabilize the discharge and to offer better heat dissipation. The gas temperature of plasma was monitored by a silicon diode temperature sensor (DT470CU131.4L, Lakeshore) at 30 mm from the center of the cryoplasma, and it was maintained with proportional integral derivative (PID) control at 85 K with an accuracy of a few Kelvin, as already demonstrated in the last chapter. During the irradiation, optical emission spectroscopy (OES) was performed to monitor the cryoplasma and the transmittance of CH_3OH/H_2O ice. The temperature, chemicals, and energetic radiation process chosen here are within the plausible range of current conditions of the outer solar system [75, 90, 156–158]. For example, as an example of outer solar system objects, Pluto has an atmospheric temperature of 40–110 K, surface pressure

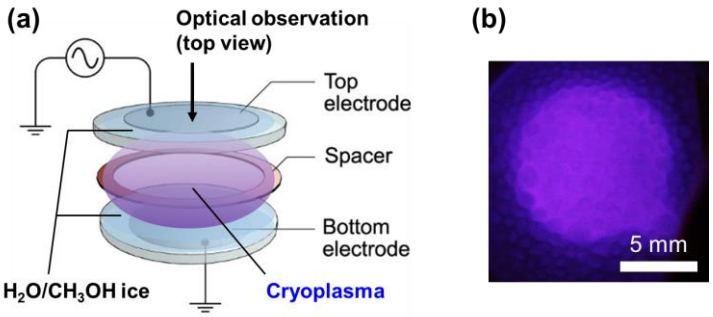

Figure 4.2 (a) Schematic illustration of the electrodes of the cryoplasma. (b) Top view photograph of the cryoplasma at 85 K, taken in a dark room through the transparent (ITO) top electrode.

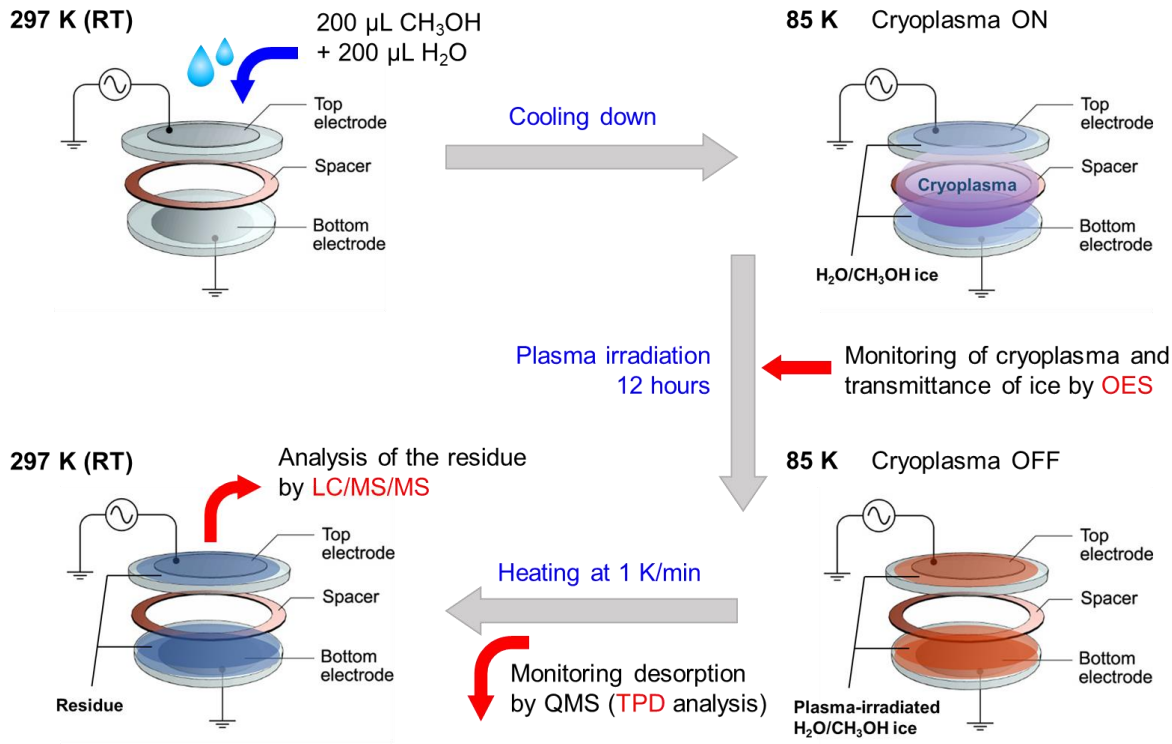

Figure 4.3 Illustration of the experimental procedure, which depicts the preparation of CH_3OH/H_2O ice sample, cryoplasma irradiation of CH_3OH/H_2O ice with monitoring cryoplasma and the transmittance of ice by OES, TPD analysis of the post-plasma-irradiated ice with heating, and the analysis of the residue at room temperature by LC/MS and LC/MS/MS.

of 1 Pa, and a surface covered by N_2 and hydrocarbon ice [90]. The higher N_2 partial pressure than actual environment was considered to accelerate reactions without change in reaction pathways.

4-2-2. TPD analysis of the plasma-irradiated ice

After the plasma irradiation of CH_3OH/H_2O ice, temperature programmed desorption (TPD) experiments were carried out with a quadrupole mass spectrometer (QMS) with electron impact ionization (Prisma Plus QMG 220M1, Pfeiffer Vacuum) to monitor the desorption from the post-plasma-irradiated ice, as shown in Fig. 4.3. Mass spectroscopy is generally used to detect and quantify products and their fragments during and after radiation experiments in astrochemistry, where TPD provide a simple and sensitive approach to analyze final products of radiation experiments [159, 160]. In TPD experiments, the QMS was attached to the outer side of the inner chamber and evacuated by a turbo molecular pump. Mass spectra were obtained as a function of temperature by heating post-irradiated ice sample with keeping the heating rate in constant. The temperature in the chamber was increased at a linear heating rate of 1 K/min from 85 to 230 K, and the desorption of fragments from the plasma-irradiated reddish colored ice was monitored. The TPD analysis was performed up to 230 K in this study, because the melting point of CH_3OH/H_2O (1:1 by volume) is approximately 230 K [161]. During the heating, the inner chamber was evacuated by the pumping system at 1×10^{-1} Pa while the mass spectrometer was operated around

3×10^{-5} Pa. To facilitate the analysis of the post-plasma-irradiated ice sample, isotope-labeled experiments were also performed. For the analysis for isotopic ice samples, 99% $^{13}CH_3OH$ (Wako pure chemical industries), 99.8% CD_3OD (Wako pure chemical industries), and 99.8% D_2O (Wako pure chemical industries) were utilized as purchased without further purification. The isotopic ice samples were prepared by cooling $^{13}CH_3OH/H_2O$, CD_3OD/H_2O, or CH_3OH/D_2O in 1:1 by volume from room temperature to 85 K, and then irradiated by the cryoplasma for 12 hours under the same conditions as the case of CH_3OH/H_2O ice sample. In all isotope-labeled experiments, the same appearance and disappearance of the reddish color were observed.

4-2-3. LC-MS and LC-MS/MS analysis of the residue

To further analyze the post-plasma-irradiated ice samples, liquid chromatography mass spectroscopy (LC-MS) spectroscopy was performed for the reside of the ice sample at room temperature. After the TPD analysis, the plasma-irradiated CH_3OH/H_2O ice was heated to room temperature, and the residue was collected for LC–MS and the subsequent tandem mass spectroscopy (LC–MS/MS). Liquid chromatography was performed by an ultra-performance liquid chromatography system (Acquity UPLC,Waters Co., Ltd.) with a hydrophilic interaction chromatography (HILIC)-type column (Acquity UPLC BEH Amide, 2.1×150 mm, 1.7 μm, Waters Co., Ltd.). The column was kept at 40°C. The mobile phase was composed of two components: 0.1% formic acid and acetonitrile (5:95 by volume for the first 15minutes and 50:50 by volume later). 10 μL of the residue was injected as picked up and flown at a speed of 0.2 ml/m. Mass spectrometry was performed by a time-of-flight type mass spectrometer (Xevo QTof MS, Waters Co., Ltd.). Ionization of the sample was conducted by electrospray ionization at 3.0 kV capillary voltage and 30 V cone voltage. The mass spectrum range was 50–1000 *m*/*z*. The chemical formula of fragment ions from the mass spectra was estimated by their accurate masses. For peaks with strong intensity, subsequent tandem mass spectroscopy was conducted. Chemical structures in the mass spectra were estimated from both their accurate masses and the mass spectra of their peaks.

4-3. Results

4-3-1. Energetic radiation by cryoplasma

From *I-V* characteristics of the cryoplasma, the power consumption of the cryoplasma was calculated to be 1.8 mW as shown in Fig. 4.4. This indicates that the total energy transferred to the ice was 1.2×10^{-3} J cm^{-2} s^{-1} assuming that all of the energy consumed by plasma was transferred to the ice. For the 12 hours of plasma irradiation, total energy dose was calculated to be 50 J cm^{-2}. This energy dose corresponds to between 10^3 and 10^4 years of energetic radiation such as solar wind in the assumption of 1 keV energies with between 10^9 and 10^{10} particles m^{-2} s^{-1} [153]. Other energetic radiations fluxes such as cosmic rays are relatively low far from the heliopause [154], although the energies delivered by the particles could be enormous and they could contribute to the chemistry in longer time scale, too [155]. The 10^3–10^4 years are very short when comparing to the timescale of the formation and evolution of the solar system (~10^9 years), and slightly longer than the Pluto's orbital period (~248 years).

4-3-2. Reddish coloration of the CH_3OH/H_2O ice during plasma irradiation

During the irradiation of the cryoplasma, photographs of ice were taken from the upper side of the electrode for color monitoring, and the optical emission from the cryoplasma was observed through the top electrode coated with transparent ITO (Fig. 4.2(a)). We found that reddish coloration appeared on the ice and became more prominent with longer plasma irradiation (Fig. 4.5). On the other hand, the intensities of the optical emission lines from the cryoplasma decreased with time in the UV and visible range (Fig. 4.6). In other words, transmittance of the ice at UV and visible wavelengths decreased, assuming constant emission intensity of the cryoplasma during the irradiation. This assumption is reasonable as the power consumption of cryoplasma during the irradiation was nearly constant (Fig. 4.4(b)). Therefore, the reddish color was attributed to the absorption by the product synthesized through the plasma irradiation. When using cryoplasma without N_2 gas flow as a control experiment (the total pressure in the inner chamber was

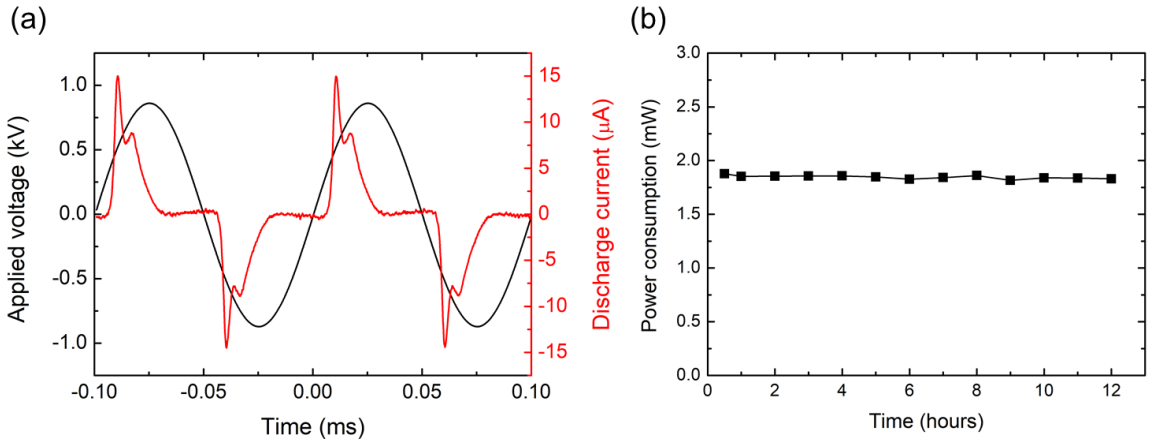

Figure 4.4 (a) *I–V* characteristics of the cryoplsama. The black and red curves indicate the applied voltage to the electrode and the discharge current of the cryoplasma, respectively. (b) Temporal change in power consumption of the cryoplasma.

kept at 2×10^3 Pa), the reddish color was not observed visually (Fig. 4.7). Thus, reactive nitrogen species from plasma, such as those identified in the emission spectrum of N_2^+ ions and excited N_2 molecules (as shown in the optical emission spectra in Fig. 4.6), should play a key role in the appearance of the reddish color.

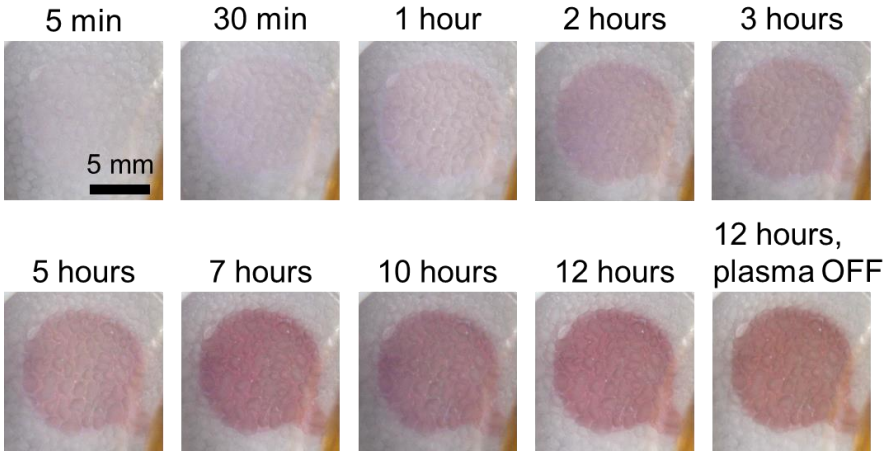

Figure 4.5 Photographs showing the changes in the reddish coloration of the CH_3OH/H_2O ice during plasma irradiation. The reddish color was not the color of the plasma itself, as shown in the photograph taken after the plasma was turned off. The color was not degraded even after three days.

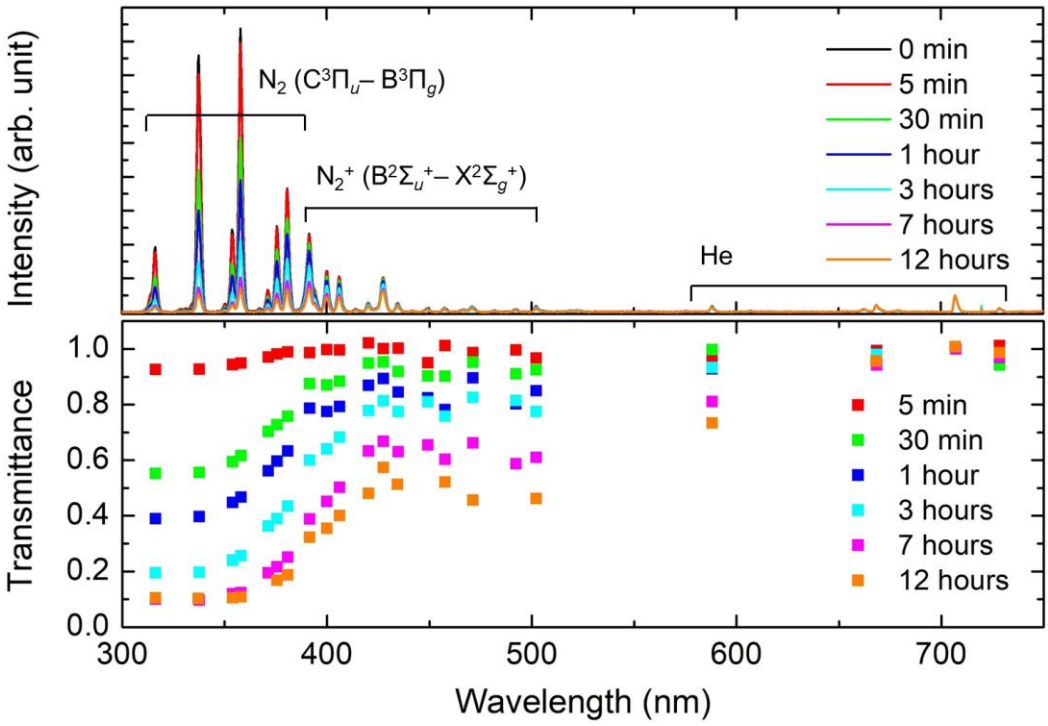

Figure 4.6 Optical emission spectra of the plasma (top panel) and transmittance of the ice (bottom panel) at different plasma irradiation durations. The transmittance at a given wavelength was calculated using the rate of decrease of the plasma emission intensity.

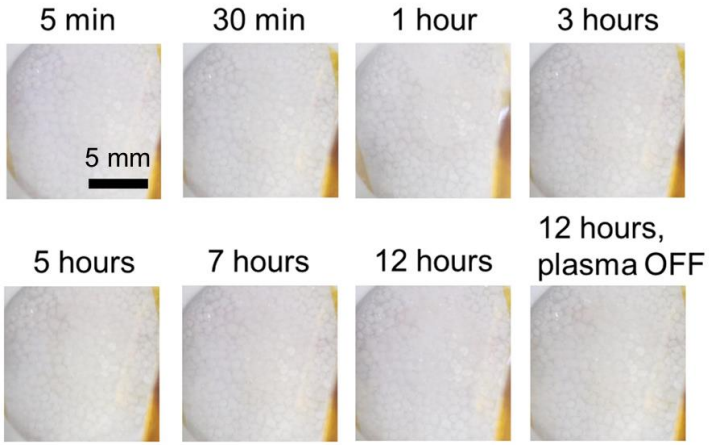

Figure 4.7 Photographs of the CH_3OH/H_2O ice during the cryoplasma irradiation without nitrogen gas flow at 85 K. Photograph of the post-irradiation ice with the plasma turned off after 12 hours of irradiation is also illustrated. The plasma-irradiated ice did not show any visible color change when nitrogen gas was not introduced.

4-3-3. Heating of the post-plasma-irradiated CH_3OH/H_2O ice

To further analyze the reddish coloration, TPD experiments were performed. The post-plasma-irradiated ice was heated at 1 K/min from 85 to 230 K at 1×10^{-1} Pa. The reddish color started fading at 120 K and subsequently disappeared at 150 K, as shown in Fig. 4.8. The reddish color was not reproduced when the temperature was conversely lowered from 165 to 85 K. It was still not reproduced when the same ice sample was subjected to 12 hours of the plasma irradiation at 170 K (Fig. 4.9). In contrast, the reddish color was sustained when cooling the post-plasma-irradiated ice from 85 to 20 K (Fig. 4.10). Therefore, the reddish color was specific to cryogenic temperatures. Since the disappearance of the reddish color was not reversible with respect to temperature, it might be due to the desorption of reddish substances and/or an irreversible chemical change of the reddish substance into colorless materials.

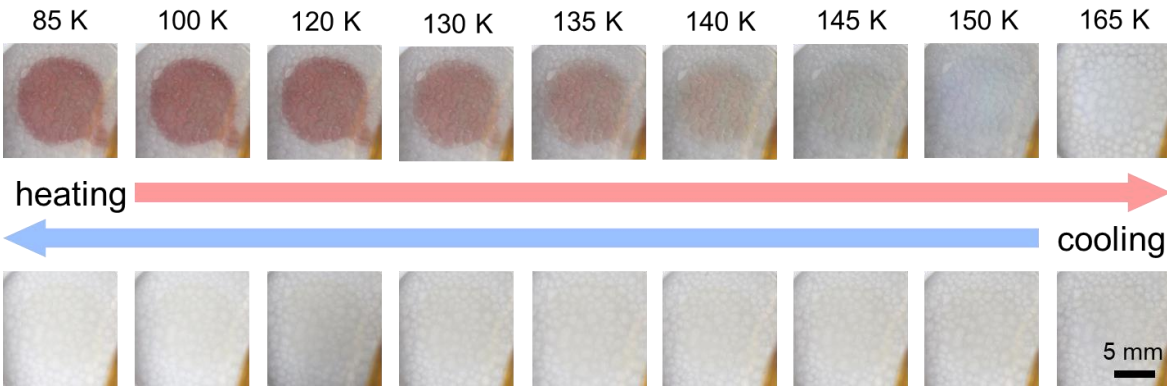

Figure 4.8 Photographs showing the disappearance of the reddish color during the heating of the post-plasma-irradiated CH_3OH/H_2O ice.

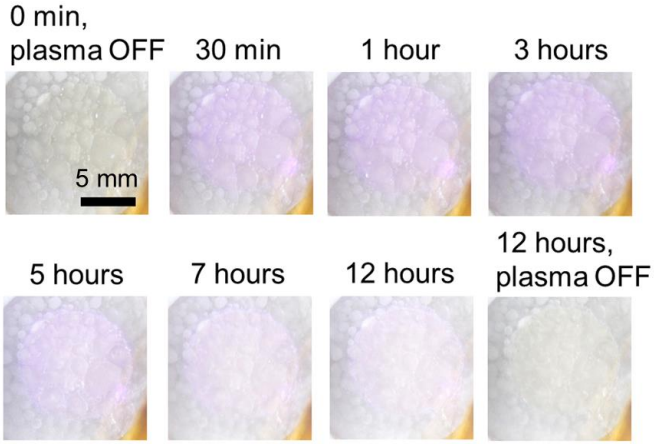

Figure 4.10 Photographs of the CH_3OH/H_2O ice during the cryoplasma irradiation at 170 K. Photographs of the pre-irradiation and post-irradiation are also shown. The plasma-irradiated ice did not show any visible color change when irradiated at 170 K.

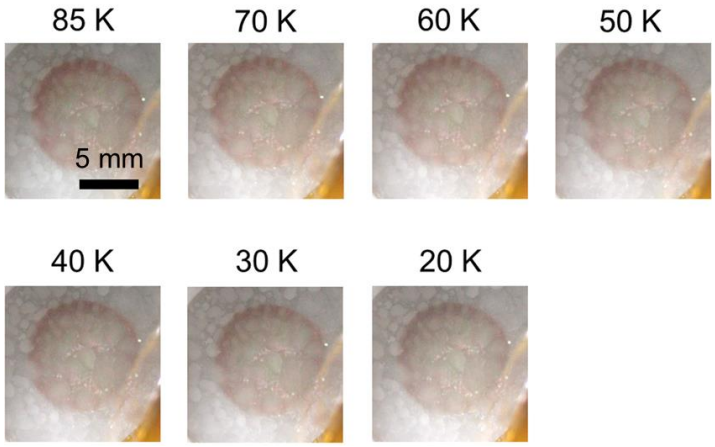

Figure 4.9 Cooling of the post-plasma-irradiated CH_3OH/H_2O ice. Photographs show that the reddish color was visibly maintained throughout the cooling to 20 K. The nonuniform reddish color was attributed to the nonuniform plasma generation at this time. The plasma was produced more strongly near the edge of the top electrode during this experiment.

4-3-4. TPD analysis of the post-plasma-irradiated CH_3OH/H_2O ice

A quadrupole mass spectrometer was used to measure the desorption from the post-plasma-irradiated ice simultaneously with the reddish color disappearance. An increase in the intensity of the mass spectra signals was detected at some mass-to-charge ratio (m/z) in accordance with the disappearance of the reddish color. In particular, m/z = 30, 46, 60, 61, 72, and 73 showed noticeable increases, as shown in the TPD spectra in Fig. 4.11. These m/z signals could correspond to fragments of desorbed reddish materials or byproducts derived from the transformation of reddish to colorless materials. To further investigate the desorption of substances that accompanied the color disappearance, TPD analysis for isotopic ice samples was also conducted. $^{13}CH_3OH/H_2O$ ice, CD_3OD/H_2O ice, and CH_3OH/D_2O ice were irradiated with the

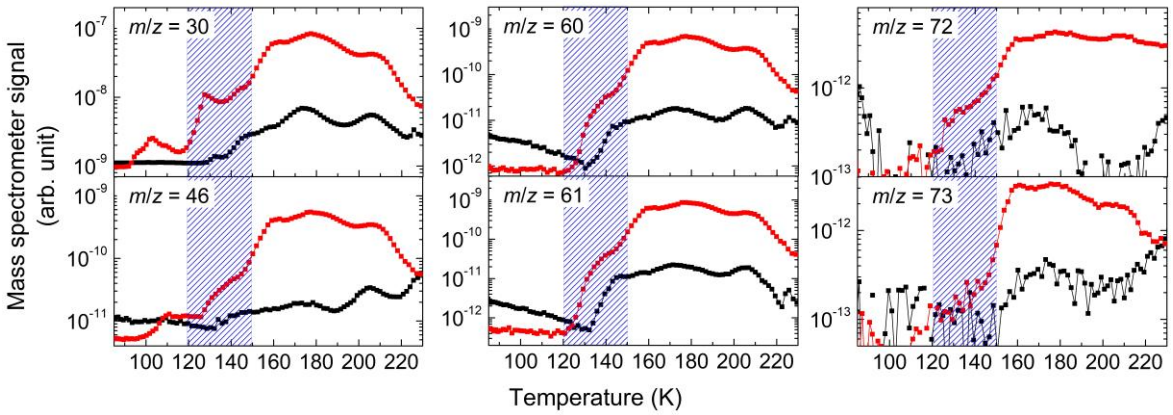

Figure 4.12 TPD spectra indicating desorption of fragments from the post-plasma-irradiated ice. The red and black lines represent plasma irradiation with and without N_2 gas input, respectively. The blue shaded regions indicate the temperature range where the reddish color was seen to be disappearing. In the spectra of m/z = 73, signals less than 10^{-13} are in the noise level.

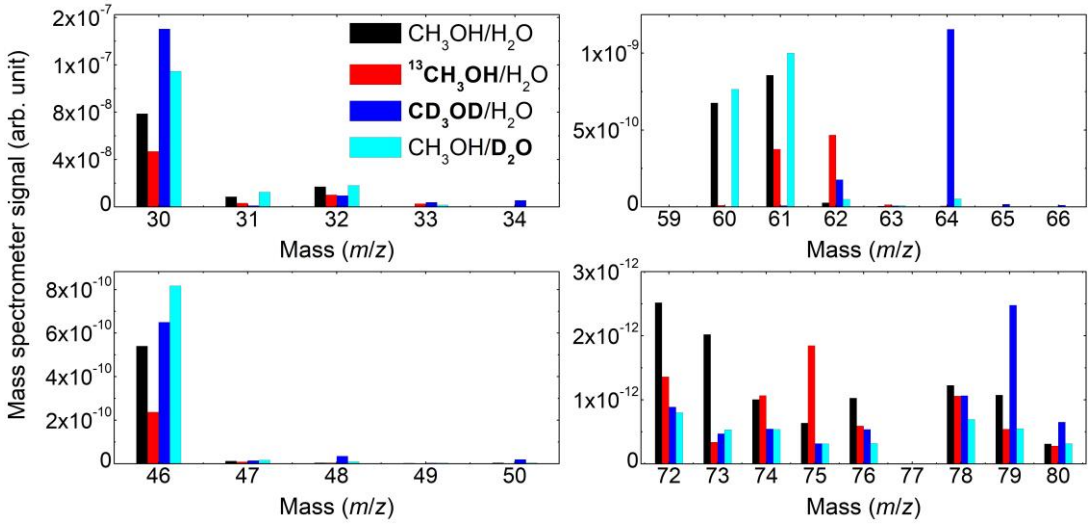

Figure 4.11 Mass spectra of the isotope-labeled analysis of the post-plasma-irradiated ice. Mass spectra at 180 K are shown here. The black, red, blue, and cyan indicators represent the post-plasma-irradiated ice of CH_3OH/H_2O, $^{13}CH_3OH/H_2O$, CD_3OD/H_2O, and CH_3OH/D_2O, respectively.

cryoplasma under the same conditions as described above. The m/z shifts between labeled and unlabeled methanol- and water-containing ice allowed estimation of the number of C or H atoms in the monitored substances.

Initially, signals at m/z = 60 and 61 showed clear shifts to higher m/z when methanol or water ices were isotopically labeled (top-right panel of Fig. 4.12). Carbon-13 labeling of methanol revealed that substances at m/z = 60 and 61 contained one methanol-derived C atom, while D labeling of methanol revealed two or four methanol-derived H atoms for m/z = 60 and three methanol-derived H atoms for m/z = 61. D labeling of water ice showed that both m/z = 60, 61 contained no water-derived H atom. Some possible molecular formulas of the substances that satisfy the isotopic analysis results are CH_2NO_2 or CH_4N_2O for m/z = 60 and CH_3NO_2 for m/z = 61. Both of these are nitrogen-containing unsaturated compounds that could possess

C = N, N = O, or amide bonds, as shown in the possible chemical structures in Fig. 4.13. Although the situation is more complicated, substances at *m*/*z* = 72 and 73 could possess unsaturated groups and/or nitrogen as well, as can be seen in Fig. 4.12, Fig. 4.13, and Fig. 4.14.

This assignment of the fragments was consistent with the TPD and isotopic analysis for *m*/*z* = 30 and 46. The spectra at *m*/*z* = 30 and 46 did not show any shift in the peak positions when any of the isotopic labeled

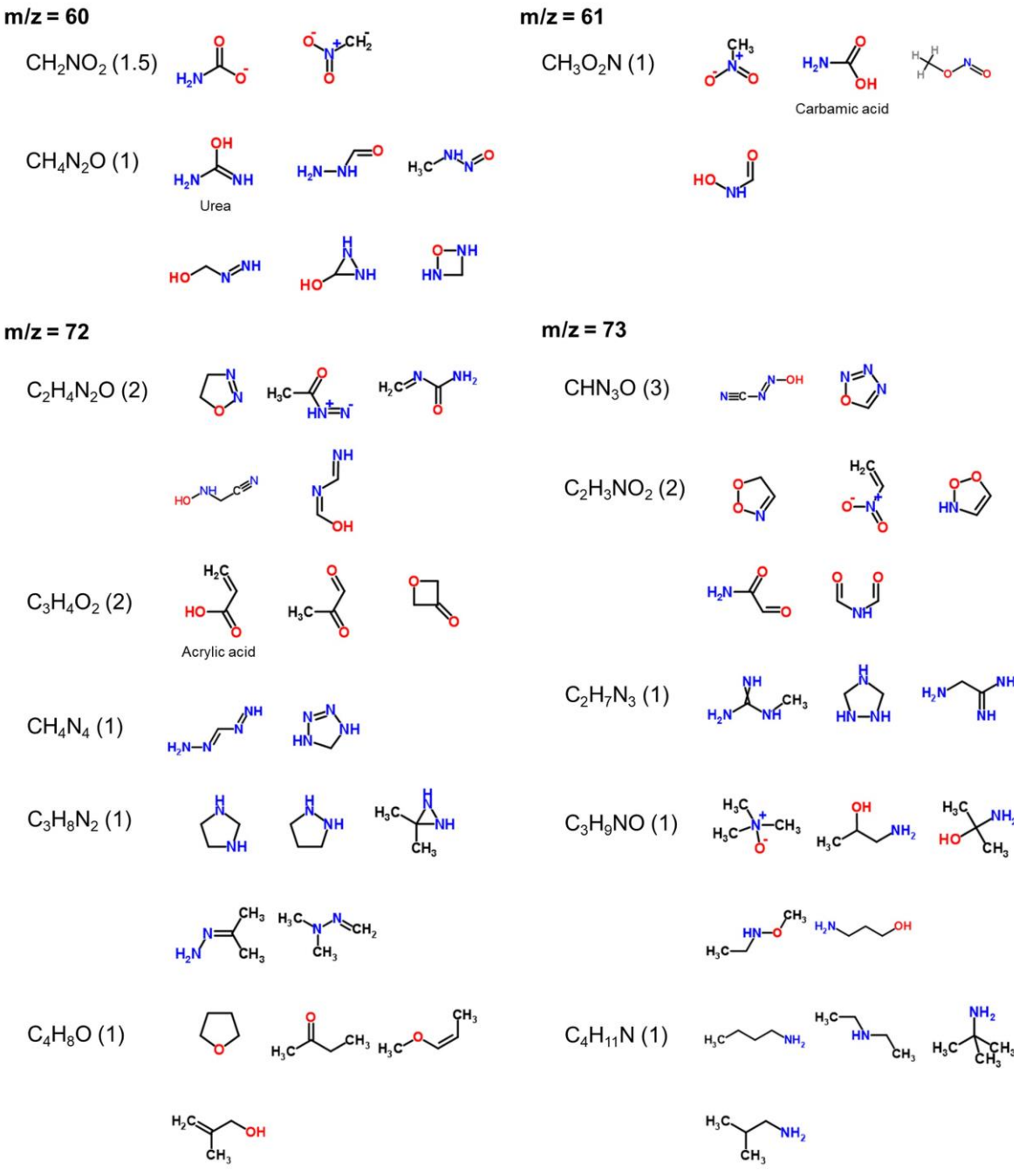

Figure 4.13 Examples of various molecular formulae satisfying the molecular masses. For *m*/*z* = 60 and 61, the molecular formula suggested above are also in good agreement with the results of isotopic analyses. The chemical structures are cited from a free chemical structure database ChemSpider (www.chemspider.com/). Numbers inside the parentheses indicate the degree of unsaturation.

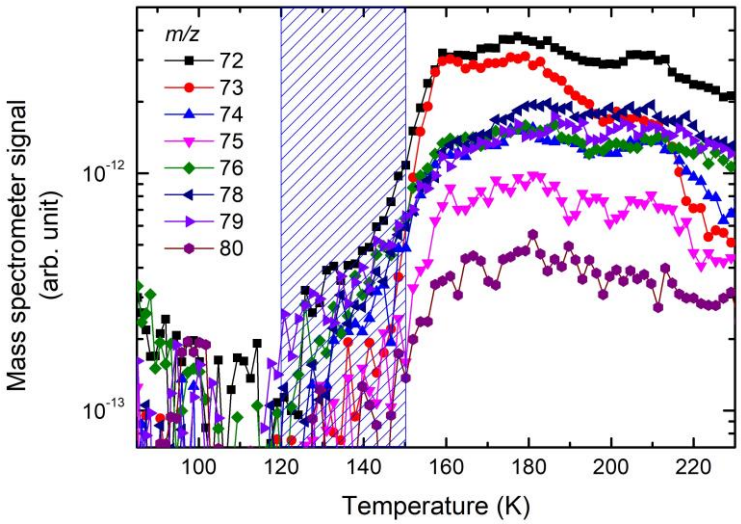

Figure 4.14 TPD spectra of the post-plasma-irradiated CH_3OH/H_2O ice for m/z = 72–80. The spectra for m/z = 77 could not be monitored correctly because of an inevitable noise from the QMS equipment.

ice was used (left panels of Fig. 4.12). This implies that fragments at m/z = 30 and 46 do not contain any C or H atoms derived from methanol and water ice. Therefore, peaks at m/z = 30 and 46 likely stem from molecules composed entirely of N and O atoms, such as nitric oxide (NO) and nitrogen dioxide (NO_2), respectively. However, NO is colorless, and NO_2 converts to colorless dinitrogen tetroxide (N_2O_4) at lower temperatures below the melting point of N_2O_4 (261.9 K), although NO_2 appears to be reddish in color. Although NO_2 might be formed directly at cryogenic temperatures, the cryogenic presence of NO_2 is unclear because no data of NO_2 vapor pressure has been proposed [162]. Thus, tentatively, a plausible situation is these nitrogen and oxygen containing compounds are fragments from our reddish materials.

4-3-5. LC-MS and LC-MS/MS analysis of the residue of the post-plasma-irradiated CH_3OH/H_2O ice

The analysis of the colorless liquid residue obtained at room temperature supports the idea that nitrogen-containing and unsaturated organic compounds could have caused the reddish coloration. After heating the post-plasma-irradiated CH_3OH/H_2O ice to room temperature, the residue was analyzed by LC–MS and further mass spectroscopy (LC–MS/MS). Total ion chromatograph with three peaks was obtained by LC-MS analysis at different retention times (t_R) as shown in Fig. 4.15. For each peak, further MS or MS/MS analyses were performed to investigate chemical structures of the substances. Synthesis of various organic compounds with larger masses than the original CH_3OH/H_2O ice, such as glycols, carboxylic acids, amines, and amides, were identified as shown in Fig. 4.16 and Fig. 4.17. Some of these compounds contain C=C and C=N bonds that absorb UV and visible radiation in the conjugated system, thus giving rise to a colored appearance. In terms of astrobiology, such structures and functional groups are essential building blocks of prebiotic organic molecules such as proteins [37, 38] and genetic materials [163]. This implies that the observed reddish color is closely related to the possible existence of prebiotic organic compounds

[141], and especially prebiotic substances that can be stable only at cryogenic environments in the outer solar system. Note that it is not clear whether the chemical compounds detected in the residue was synthesized during the cryoplasma irradiation or during the heating of the post-plasma-irradiated ice.

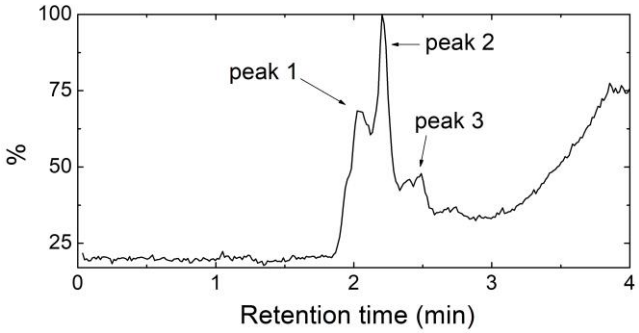

Figure 4.16 Total ion chromatogram by the liquid chromatography of the sample residue at room temperature. Further mass spectroscopy was performed for the peaks of different retention times, i.e., peak 1 at t_R = 2.02 minutes, peak 2 at t_R = 2.21 minutes, and peak 3 at t_R = 2.39 minutes.

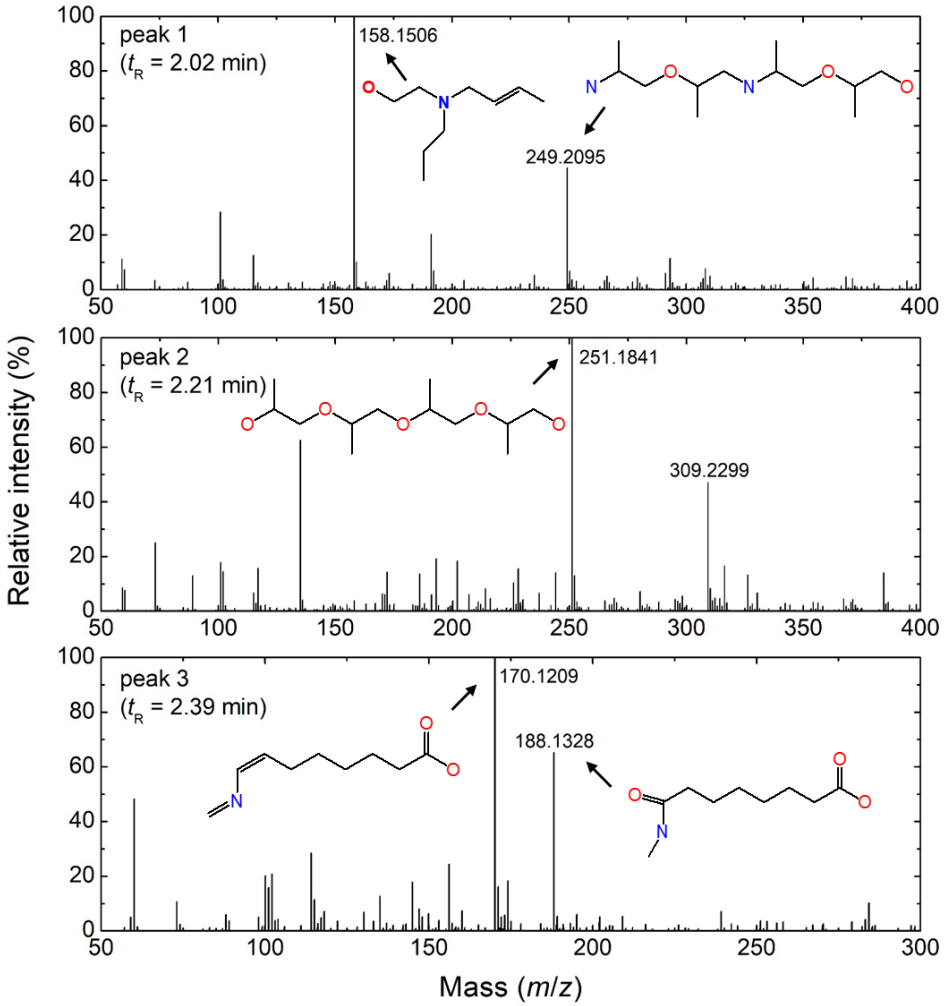

Figure 4.15 LC–MS spectra of the residue of the plasma-irradiated CH_3OH/H_2O ice at room temperature, corresponding to different retention times of total ion chromatogram shown in Fig. 4.14. The chemical structures of notable peaks identified by MS/MS analysis (Fig. 4. 15) are also depicted.

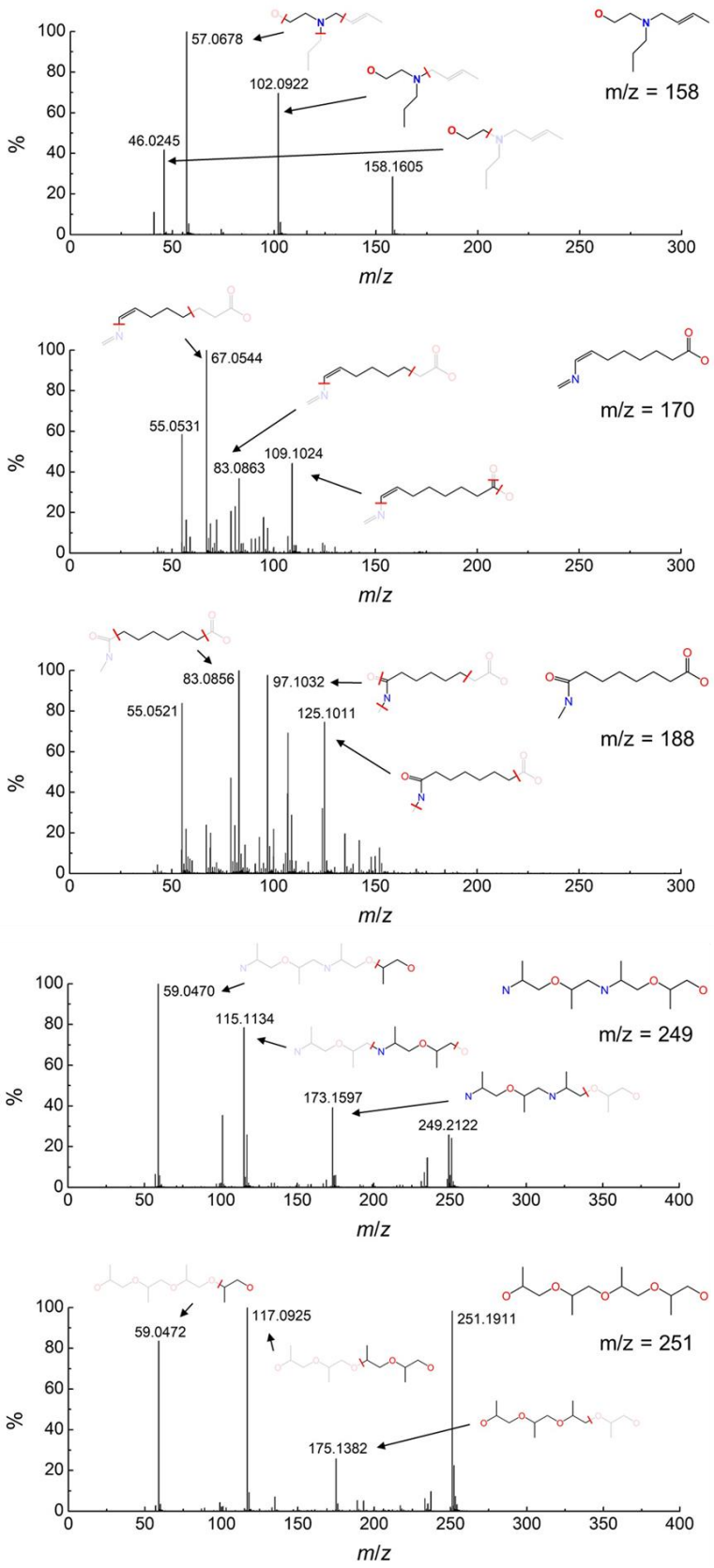

Figure 4.17 LC–MS/MS spectra of the peaks at *m*/*z* = 158, 170, 188, 249, and 251 in the LC–MS spectra in Fig. 4.15. MS/MS analysis was carried out to estimate chemical structures of the peaks by monitoring the fragments from the substance of the target *m*/*z* peak. The chemical structures of fragments estimated for the observed MS–MS spectra peaks are also depicted.

4-4. Discussion

4-4-1. Comparison of the obtained reddish color to previously reported ones

In the outer solar system, reddish colors have been explained by complex organic tholins, which contain delocalized electrons in the conjugated unsaturated bonds of aliphatic and aromatic hydrocarbons with some amounts of substituted nitrogen [143, 144]. Excitation of delocalized electrons is accompanied by absorption at UV and visible wavelengths, which correspond to the reddish color. The reddish materials in this study can also be attributed to complex organic materials, considering the absorption at UV and visible wavelengths and the nitrogen-containing unsaturated fragments. However, the temperature-dependent behavior at cryogenic temperatures in this study has not been observed in previously reported reddish coloration of refractory tholins. This might imply a significant contribution of smaller and more volatile colorants to the appearance of cold surfaces in the outer solar system.

4-4-2. New explanation for the color diversity of outer solar system objects

The color diversity of icy objects in the outer solar system, especially the absence of ultra-red coloration closer to the Sun, has been previously explained by the variation of compositions depending on the body environment [135, 147–149], with considering reddish organic tholins and colorless volatile species [143]. However, the explanation is not straightforward and still debatable because the well-known organic tholins are nonvolatile even when warming to room temperature. Here, the formation of the cryogenic-specific reddish coloration could offer a new possible explanation to the reddish color distribution in the outer solar system. The cryogenic-specific reddish materials disappear by sublimation or conversion to other colorless compounds at warmer cryogenic temperatures, as an icy body travels from the trans-Neptunian region to the inner solar system, such as Centaurs and thence the Jupiter-family region (see also Fig. 4.18). This scenario implies that the body coloration and its diversity might be able to serve as a probe of current temperature and/or temperature history. The concept of reddish materials that are stable only at cryogenic temperatures is potentially useful for further investigation of color diversity observed in the outer solar system, including many reddish objects, and would contribute to the further understanding of the nature and formation of the solar system.

To place our results in context with observational data of the color distribution of bodies in the outer solar system, we considered the color distribution of several Centaurs [164, 165] as a function of perihelion distance (Fig. 4.19). From this figure, we see that the ultra-red object closest to the Sun is in the 5–10 AU range, with 31824 Elatus having the closest perihelion distance of 7.3 AU [165]. No ultra-red objects have been found at distances less than 5–10 AU [134]. At such perihelion distances between the orbits of Jupiter and Saturn, the surface temperature of the bodies can reach to 120–150 K [75, 157]. This corresponds to the temperature range at which the reddish coloration faded and disappeared in our study. Therefore, our results and proposed scenario that reddish coloration of icy objects in the outer solar system could be explained by the presence of materials that are stable only at cryogenic temperatures are consistent with the observational data.

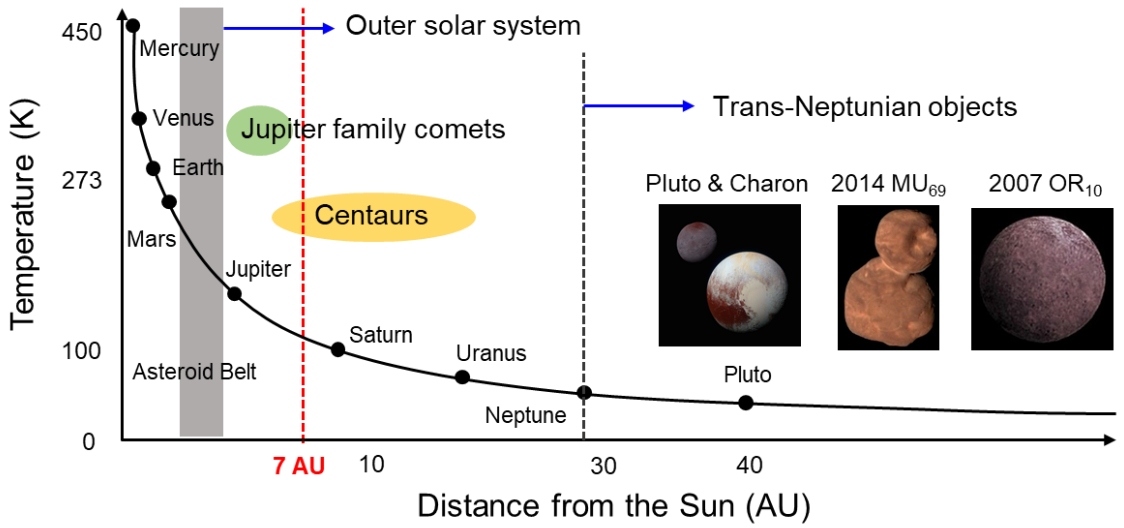

Figure 4.19 Temperature distribution in the solar system with the distance from the Sun. Outer solar system is defined as the outer region of Asteroid belt, which is in icy cryogenic conditions below the melting point of water. The positions of Jupiter family comets, Centaurs and Trans-Neptunian objects are also illustrated. The images inserted in this figure show typical ultra-red objects in the Trans-Neptunian region, taken by the New Horizons spacecraft [90, 137].

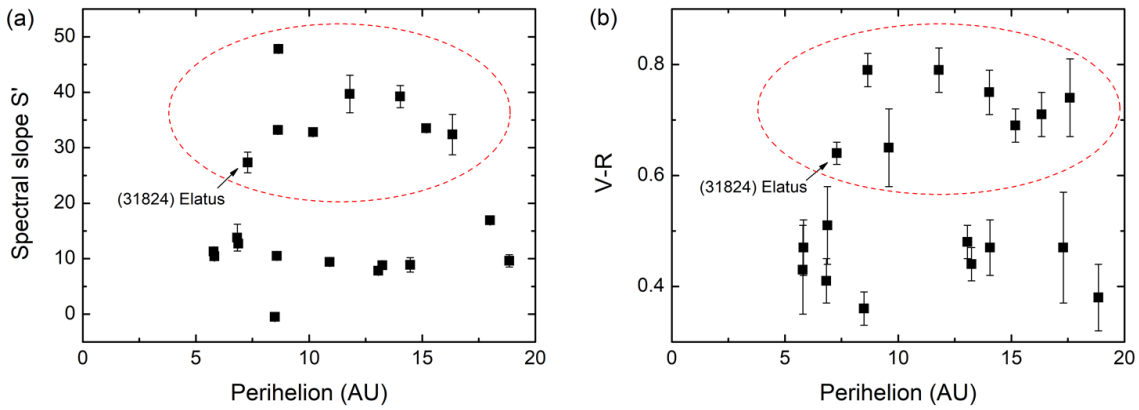

Figure 4.18 Color distribution of Centaurs at different perihelion distances. (a) Spectral slope (S') vs. perihelion distances. The presented data were taken from [165]. (b) $V-R$ color index vs. perihelion distances. The presented data were taken from [164]. The red dashed circles indicate ultra-red objects with $S' > 27$ or $V-R > 0.6$, respectively.

4-5. Summary and perspective

In this chapter, we demonstrated reddish coloration that is stable only at cryogenic temperatures by irradiating methanol- and water-containing ice with nitrogen-containing cryoplasma at 85 K. The reddish color visually faded and disappeared at 120–150 K as the ice was heated, unlike well-known refractory organic tholins that are stable even when heated to room temperature. By TPD analysis with isotopically labeled ices and LC–MS/MS analysis of the residue, the reddish material was suggested to be nitrogen-containing organic compounds. The temperature dependence of reddish coloration under cryogenic conditions could provide a new possible explanation for the absence of ultra-red coloration closer to the Sun in the outer solar system. Our result implies that a reddish material specific to cryogenic environments could be useful for the investigation of color diversity and formation mechanism of the outer solar system. Moreover, it is worthwhile to mention that cryoplasma was demonstrated to be a novel technology for accelerating the investigation of chemistry and materials science in cryogenic space environments including the outer solar system.

Although the peculiar temperature dependence of the reddish coloration and its implication to the astrophysical environment were investigated, chemical structure and kinetics of the reddish material were not identified. They are significant to apply the results in laboratory simulation to astrophysical environments. To further analyze the chemical structure and kinetics of cryogenic-specific reddish material, infrared spectroscopy (IR) is the most common analysis tool, because it enables in-situ analysis of the chemical structure nondestructively. IR has been employed in other previous studies of astrochemistry, and database of IR spectra and optical constants are also found to quantify products [32]. In addition, further investigation of the synthesis of reddish coloration with changing temperature and chemical compositions of ice and cryoplasma should also be performed to elucidate the kinetics and mechanism of the reddish coloration. By combining IR with other analysis techniques such as mass spectroscopy, Raman spectroscopy, and UV-vis spectroscopy, and by changing the parameters of the simulating experiment, the origin of the cryogenic-specific reddish coloration is expected to be further understood.

Chapter.5 Development of plasma-assisted freeze templating

To further explore the potential of plasma-ice interfacial reaction field, a possible application was developed in the engineering point of view. To investigate advantages of plasma-ice interfacial reaction field as a promising scheme for materials design, we focused on self-assembling structures accompanied by freezing of aqueous solution or colloidal dispersion. In this chapter, a smart synthesis of a self-standing gold nanoparticle (AuNP) film was performed at plasma-ice interface, for which the process was termed as plasma-assisted freeze templating (PFT).

PFT is a novel scheme of materials processing at the plasma–ice interface that is proposed in this study for the first time, in which the focus is on a highly concentrated thin liquid layer on ice as a size-tunable micro- or nanoscale plasma-assisted reactor. When an aqueous solution freezes in one direction, solutes are expelled from the growing ice body along the temperature gradient and a highly concentrated micro- or nanoscale thin liquid layer is formed on the ice body, as described in chapter 1.2. The concentration of the thin liquid layer is determined thermodynamically, implying that the thickness of the thin liquid layer can be tuned by controlling the temperature or concentration of the aqueous solution. The thin liquid layer is attractive as a template for the synthesis of self-standing thin-film materials, because it is thermodynamically stable and the ice body can be removed easily by melting or freeze-drying. Meanwhile, chemical reactions can be initiated in the thin liquid layer by introducing reactive species from plasma, as investigated in many recent studies. For example, plasma-induced chemical reactions in aqueous solutions are useful for the simple synthesis of metal nanoparticles, where short- and long-lived reactive species such as solvated electrons, H radicals, and H_2O_2 formed by OH radicals complementarily promote the chemical reduction of metal ions in aqueous solutions.

In this chapter, as a first demonstration of the concept, the synthesis of self-standing AuNP films with porous structure was performed, thorough which a thermodynamically size-tunable template and material design at the plasma–ice interface by PFT was confirmed. Nanostructured gold materials, such as nanoporous gold are promising in the recently developing trend of sustainable development and energy management in harmony with the environment for catalysts [166–169], biosensors [170, 171], electrodes for batteries and capacitors [172, 173], and stretchable transparent conductors [174], owing to their desirable features of both gold bulk and size-enhanced effect in the nanoscale.

5-1. Experimental approach

5-1-1. Setup for cryoplasma jet

Cryoplasma jet was utilized for the reduction of the auric ions at the interface with the frozen solution. The schematic of the experimental setup is illustrated in Fig. 5.1. The cryoplasma jet was generated with a dielectric barrier discharge (DBD) configuration at an atmospheric ambient environment without any high vacuum system. The electrode consisted of a quartz tube (inner diameter: 1.1 mm, outer diameter: 1.5 mm) covered with a copper mesh as a grounded electrode and a copper wire (50 μm diameter) located at the center of the tube as a powered electrode. Helium gas (purity >99.99%) was introduced into the quartz tube at a flow rate of 300 sccm for the generation of discharge plasma, and nitrogen gas (purity >99.9999%) was passed at 200 sccm on the outside of the tube to alleviate the adhesion of frost. Helium gas was cooled in advance by passing it through a liquid nitrogen bath. A sinusoidal AC voltage of 1.5 kV_{pp} was applied to the powered electrode at 25 kHz with a high-voltage amplifier (HVA4321, NF) to generate and sustain the cryoplasma jet. The cryoplasma jet had a diameter of less than 500 μm. The gas temperature during the generation of the cryoplasma jet was measured to be approximately −5 °C with a K-type thermocouple at a distance of 1.5 mm from the exit of the quartz tube, i.e., the position of the surface of the frozen solution that will be described later. The plasma gas temperature was also confirmed by the estimation of the rotational temperature of nitrogen molecules at the second positive system by optical emission spectroscopy. The rotational temperature is generally used as an approximation of the gas temperature in plasma [11, 114]. The rotational temperature was deduced from the optical emission of second positive system ($C^3\Pi \rightarrow B^3\Pi$)

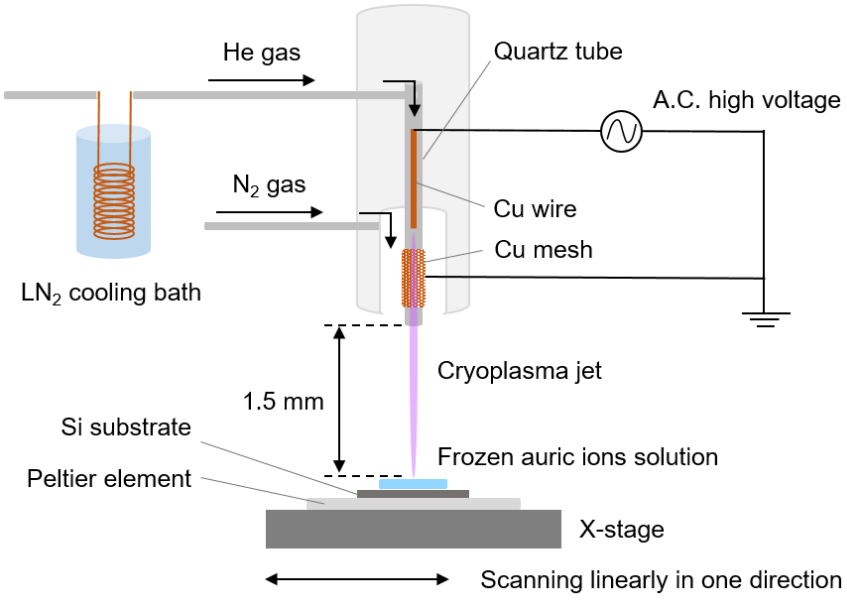

Figure 5.1 Schematic illustration of the experimental setup for the synthesis of AuNP film by PFT. Cryoplasma jet was generated by the DBD configuration by introducing helium (He) gas cooled with liquid nitrogen (LN_2) cooling bath and was irradiated onto the frozen solution of auric ions on a Si wafer cooled by a Peltier element from the bottom side. The linear scanning irradiation of the cryoplasma jet was conducted by moving the frozen solution using a one-dimensional stage.

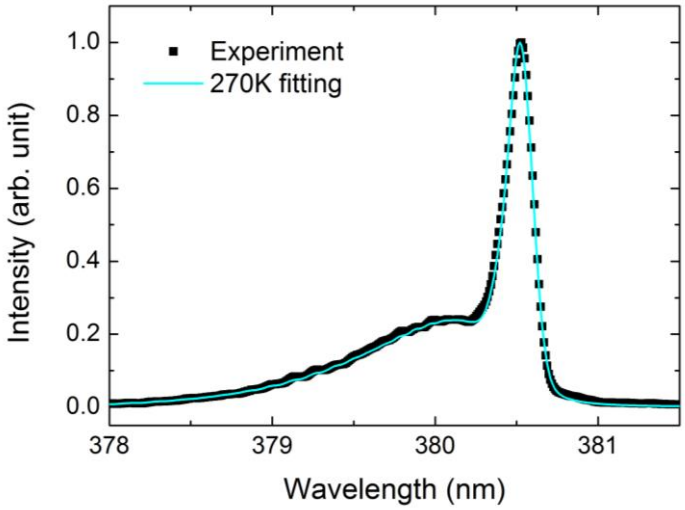

Figure 5.2 Optical emission spectrum of the second positive system of the nitrogen molecules at 380.49 nm. Blue solid line shows a calculated spectrum in the assumption of 270 K rotational temperature.

at 380.49 nm (v', v'' = 0, 2). The optical emission of the nitrogen second positive system was obtained from the helium cryoplasma jet during the PFT process with a spectrometer (iHR320, HORIBA), as shown in Fig. 5.2. The optical emission spectrum was fitted with the changing rotational temperature of nitrogen molecules, and the best fit was found to be between 260 and 280 K. Therefore, the gas temperature of −5 °C (268 K), as measured by a thermocouple, was in good agreement with that derived from the spectroscopic result.

5-1-2. Synthesis and characterization of AuNP film

Hydrogen tetrachloroaurate(III) trihydrate ($HAuCl_4 \cdot 3H_2O$, Wako Pure Chemical), and purified water (Wako Pure Chemical) were used as pur chased without further purification. Ten μL of aqueous $HAuCl_4 \cdot 3H_2O$ solution was dropped on a Si wafer (<0.02 Ωcm, p-type, Nilaco), which was set on a Peltier element (2MP04-096-1505, Nippon Tecmo). The Peltier element was driven by a DC power source (PMC18-2A, Kikusui Electronics) to freeze the solution of auric ions, and the bottom side was cooled by a water-circulating cooling system for stable operation.

The procedures of the synthesis of AuNP film is shown in Fig. 5.3. At first, the solution of auric ions was frozen in one direction from the bottom side by a Peltier element, to form a thin liquid layer concentrated with auric ions at the top of the frozen solution. In this study, the concentration was estimated to be approximately 1000 times approximately, assuming a typical binary phase diagram, as shown later. Subsequently, the cryoplasma jet was irradiated onto the surface of the frozen solution at a distance of 1.5 mm between the ice surface and the exit of the quartz tube, to synthesize AuNP film in the thin liquid layer by reducing auric ions to form gold nanoparticles by reactive species from the plasma such as electrons, atomic H radicals, and H_2O_2, followed by the formation of a AuNP film in the thin liquid layer owing to the agglomeration and interconnection of gold nanoparticles. The irradiated position was scanned

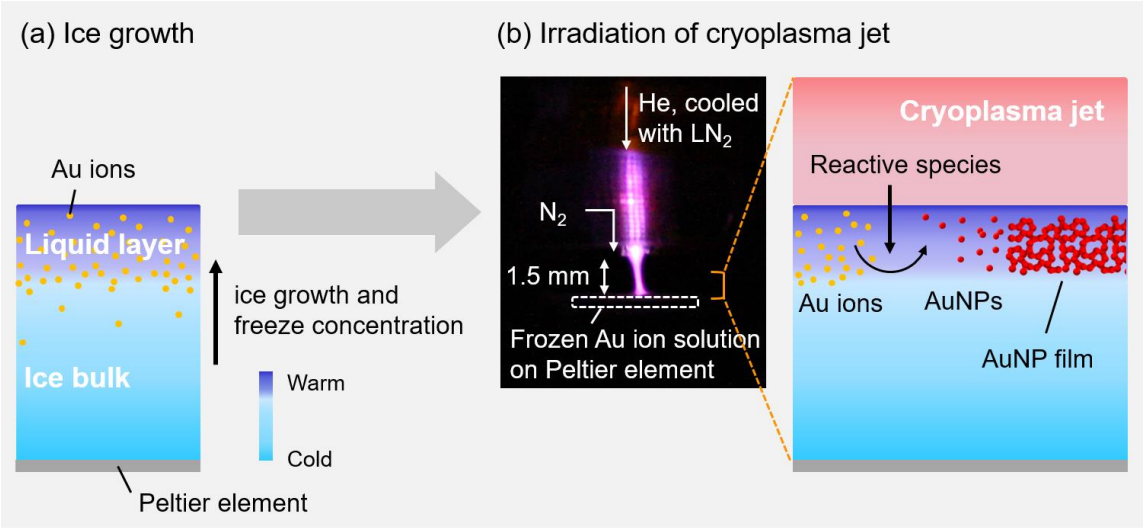

Figure 5.3 Schematic illustration of AuNP film synthesis at the plasma–ice interface by PFT. (a) formation of thin liquid layer on the frozen solution, by freezing in one direction. (b) Subsequent synthesis of AuNP film in the thin liquid layer at the plasma-ice interface by cryoplasma jet irradiation. The inset photograph shows the cryoplasma jet irradiation of the frozen solution.

linearly from one side to the other at 50 μm/s for four times. Considering the diameter of the cryoplasma jet of 500 μm, the total nominal growth time of the AuNP film at the center of the track was approximately 40 s. As shown in later, the results indicate that this growth time is sufficient to obtain the AuNP film whose thickness is limited by the thickness of the thin liquid layer on the frozen solution.

Scanning electron microscopy (SEM) and energy-dispersive X-ray spectroscopy (EDS) analyses were conducted using a scanning electron microscope (JSM-6060LV, JEOL) with an energy dispersive X-ray analysis station (JED-2300). Higher resolution SEM was performed using a Schottky field emission scanning electron microscope (JSM-7900F, JEOL). Transmission electron microscopy (TEM) images and electron diffraction patterns were recorded with a transmission electron microscope (JEM-2100, JEOL) at a 200 kV operation. A laser microscope (VK-8510, Keyence) was utilized for measuring the thickness of the synthesized AuNP film. For the investigation of the catalytic ability of the AuNP film, *p*-nitrophenol (Wako Pure Chemical) was used as purchased without further purification.

5-2. Results and discussion

5-2-1. Characterization of AuNP film by PFT

A AuNP film of porous structure was synthesized by PFT, as illustrated schematically as described above. The AuNP film in the following description of this section was synthesized using a 25 mM solution of auric ions, which was frozen at −10 °C at the bottom side of the frozen solution.

Figure 5.4(a) exhibits a line-shaped AuNP film synthesized on the frozen solution. The line width of the AuNP film was measured to be 400–500 μm (Fig. 5.4(b)) and was approximately the same as the diameter of the cryoplasma jet. Therefore, the AuNP film was synthesized area-selectively by the reduction of auric ions only where the cryoplasma jet was irradiated. Furthermore, the ice body of the frozen solution served as a template for the synthesis of thin films; consequently, the synthesized AuNP film was self-standing. This allowed them to be removed easily by melting the ice body of the frozen solution and cleaning them with purified water for further characterization.

As shown in Fig. 5.4(b–d), the AuNP film exhibited a self-assembled hierarchical porous structure with micro- or nanoscale interconnections of AuNPs. The constituent element of the structure was confirmed as gold by EDS (Fig. 5.5). The lattice structure of the AuNPs that composed the film was confirmed to be fcc gold with randomly oriented crystallites by the diffraction pattern from TEM observation (Fig. 5.6), which was similar to that of the gold nanoparticles synthesized by plasmas in aqueous solutions [58]. Higher and lower density porous structures were observed in the AuNP film line (Fig. 5.4(b)) with densely packed interconnected nanoparticles with porous structure at the center (Fig. 5.4(c)) and a hierarchical mesh structure around it (Fig. 5.4(d)). This difference in structure is attributable to the radial distribution of the

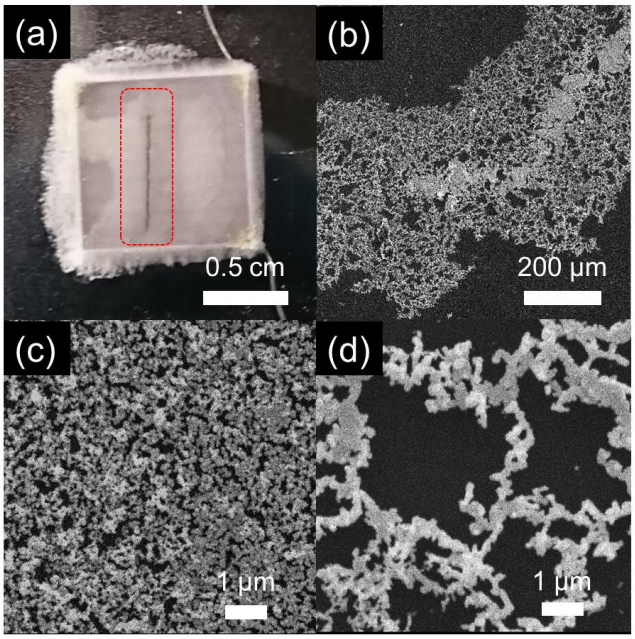

Figure 5.4 Top-view of AuNP film synthesized by PFT. (a) Photograph of the line-shaped self-standing AuNP film formed on the frozen solution. (b) SEM image of AuNP film, and the detailed images of (c) the center and (d) edges.

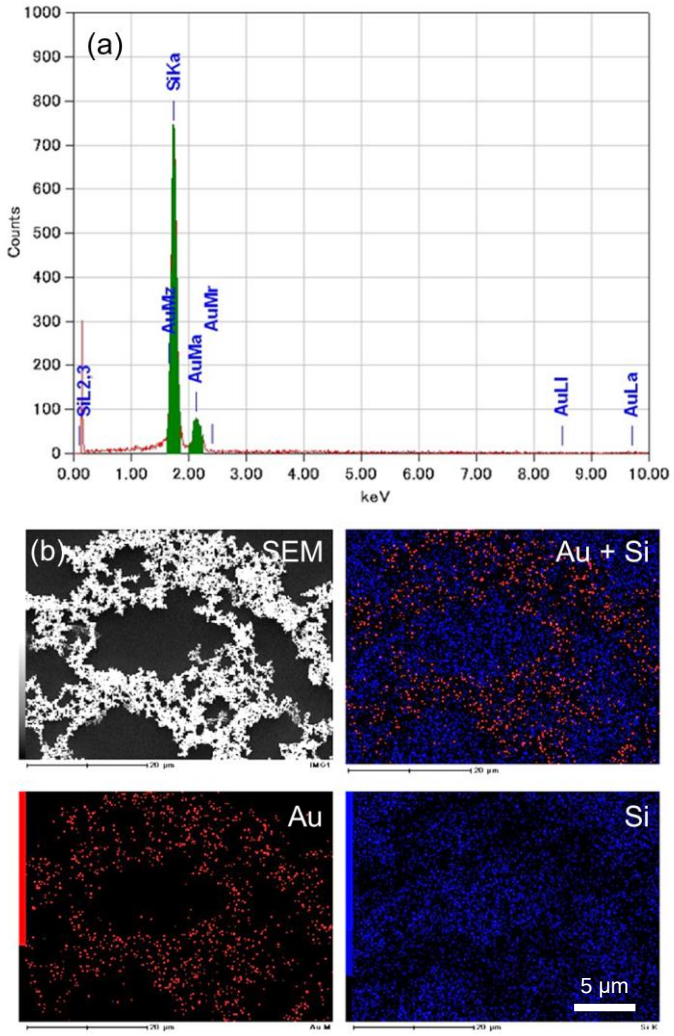

Figure 5.6 (a) EDS spectra of AuNP film, and (b) mapping of each atomic element.

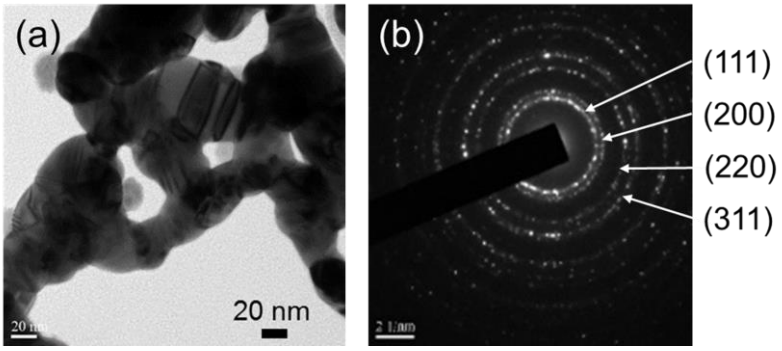

Figure 5.5 (a) TEM image and (b) diffraction pattern of AuNP film. The ring patterns indexed from (111), (200), (220) and (311) reflections are exhibited, which indicate the existence of gold atoms in fcc crystal lattice.

cryoplasma jet, i.e., the higher electron density and reactive species at the center resulted in the higher synthetic rate of AuNPs. The size distribution of the AuNPs in the film was measured from the higher-resolution SEM image, as shown in Fig. 5.7. The distribution was well represented by a Gaussian

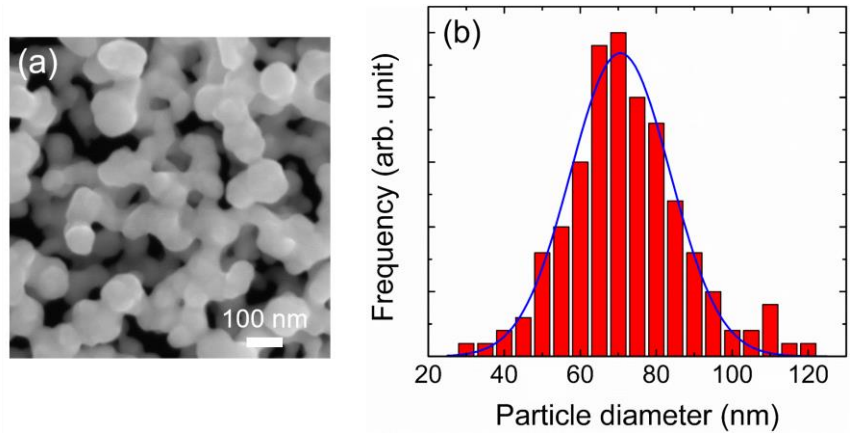

Figure 5.7 (a) Higher resolution SEM image of Fig. 5.4(c) and (b) AuNP size distribution of AuNP film. The experimental distribution of AuNPs (red bar) was fitted by a Gaussian profile (blue solid line), with a mean diameter of 71 nm and a standard deviation of 13 nm.

distribution with an average diameter of 71 nm and the standard deviation of 13 nm, as represented by a blue solid line in Fig. 5.7. The measured size of the AuNPs in the film was larger than that of AuNPs synthesized by plasmas in liquid without surfactants [55]. This can be explained by the longer residence time of the AuNPs in liquid influenced by plasma owing to the spatially confined thin liquid layer on the frozen solution that resulted in the further growth and interconnection of AuNPs. Moreover, the effect of short-lived species such as solvated electrons and atomic H radicals could be dominant in the thin liquid layer at the plasma–ice interface because the thickness of the liquid layer is comparable or not excessively large compared with the diffusion length of the short-lived species. For example, the thickness of the thin liquid layer was approximately 1 μm in this study, as described in the following sections, whereas the diffusion length of the solvated electrons at plasma–liquid interface is 10–100 nm [53, 175]. Therefore, the abundant short-lived species confined in the thin liquid layer may also initiate the growth and interconnection of AuNPs. The observed hierarchical structure of the AuNP film has been widely reported in a seed-mediated self-assembly synthesis of nanostructured gold thin films [167, 172, 176]. The formation mechanism of the self-assembled hierarchical structure is typically explained by diffusion limited aggregation (DLA) [172, 177, 178] in which particles adhere once they collide to each other. In our case, the mechanism of the AuNP film synthesis can also be explained based on the DLA process as follows: AuNPs formed from the auric ions in solution by cryoplasma irradiation were agglomerated to form the hierarchically assembled structures accompanied by the DLA model, and the agglomerated AuNPs were interconnected to each other owing to the further reduction of auric ions by the cryoplasma.

A cross-sectional observation using SEM confirmed the thickness of the AuNP film. As shown in Fig. 5.8, the thickness was approximately 1 μm at the highly dense areas of the AuNP film. Meanwhile, the thickness of the thin liquid layer is considered to be in the order of 0.1–10 μm in the experimental conditions, based on the phase diagram of the aqueous solution systems, when assuming the phase diagram of KCl aqueous solution as a typical example [44, 179]. This implies that the AuNP film was formed in the thin liquid layer on the frozen solution, which is the concept of PFT. The details are discussed in the next section.

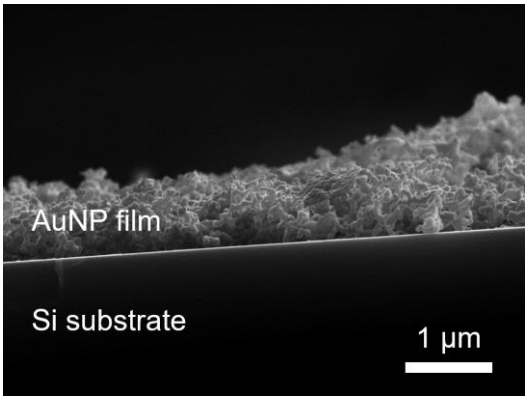

Figure 5.8 Cross-sectional SEM image of the AuNP film.

It is noteworthy that the synthesis of the AuNP film by PFT was performed without any surfactants or additional templates; only cryoplasma jet was irradiated onto the frozen solution using the ice body of the frozen solution as a substrate for the synthesis of the AuNP film in the thin liquid layer. For the chemical synthesis of nanostructured gold such as nanoporous gold, many techniques have been reported previously, such as dealloying [173, 180], templating [181], seed-mediated self-assembly [167, 172, 176], etc. These chemical methods are potentially susceptible to the effects of impurities, because surfactants or templates are required for the fabrication of nanostructures. In contrast, PFT is a simple technique that enables the impurity-free and area-selective synthesis of AuNP films with porous structure. Therefore, PFT can be an attractive method for the synthesis of nanostructured self-standing thin films.

5-2-2. Catalytic ability of the AuNP film synthesized by PFT

AuNP films such as nanoporous gold are a promising catalytic material for various oxidation and reduction reactions because of their large specific surface areas arising from their nanostructured configurations [166]. To investigate the catalytic ability of the AuNP film synthesized by PFT, we conducted the reduction of *p*-nitrophenol as a representative example [167]. In this case, 45 mg of $NaBH_4$ was added as a reduction agent to 3 mL of 0.085 mM *p*-nitrophenol solution under stirring. When three pieces of 10 mm long AuNP film line, which was synthesized from a 25 mM frozen solution of auric ions at −10 °C, were added to the solution, the yellow color of the *p*-nitrophenol solution disappeared within 10 min. The color of the solution did not change even after 1 day in the absence of a AuNP film. The reduction of *p*-nitrophenol was confirmed by the absorption spectra, as shown in Fig. 5.9. The absorption of *p*-nitrophenol at 400 nm disappeared and that of *p*-aminophenol around 300 nm appeared with AuNP film; meanwhile, the absorption of *p*-nitrophenol remained in the absence of AuNP film. The exhibited catalytic ability of the AuNP film synthesized by PFT was comparable to that of nanoporous gold thin film reported previously [167]. Therefore, the AuNP film synthesized by PFT demonstrated catalytic ability comparable to nanoporous gold synthesized by conventional chemical methods.

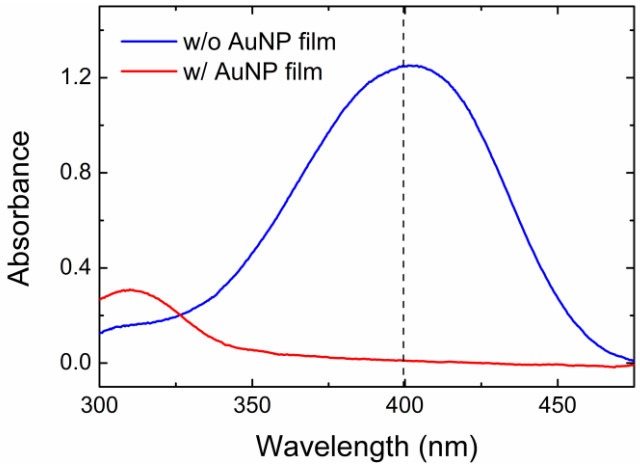

Figure 5.9 Spectral change in *p*-nitrophenol owing to the catalytic activity of AuNP film. The dashed line at 400 nm indicates the position of the absorption of *p*-nitrophenol.

5-2-3. Temperature and concentration dependence of PFT

In the PFT method, we focus on the thin liquid layer at the top of the frozen solution as a small-scale plasma-assisted reactor, exploiting the freeze concentration. To confirm the concept of PFT or the usage of the thin liquid layer as a plasma-assisted reaction field, we measured the thickness of the synthesized AuNP film using a laser microscope, while varying either the temperature at the bottom side of the frozen solutions or the initial concentration of the solution of auric ions before freezing. Figure 5.10 represents the thickness of the AuNP film as a function of temperature and concentration. The thickness of the AuNP film was approximately 1 μm at the lower temperature and concentration, and it increased to a maximum of 7 μm with increasing temperature and concentration.

This temperature and concentration dependence of the AuNP film thickness was attributed to the variation in the thickness of the thin liquid layer on the ice body of the frozen solution. To investigate the temperature and concentration dependence of the AuNP film thickness, the relationship between the thickness of the thin liquid layer on the frozen solution of auric ions and the temperature and concentration was investigated, based on the mass balance of auric ions. The mass balance of the auric ions before and after freezing the solution of auric ions can be described as follows, assuming a homogeneous concentration of auric ions in both the liquid and solid phases

$$C_0 t_0 = C_l t_l + C_s(\alpha t_0 - t_l) = C_l t_l + kC_l(\alpha t_0 - t_l)$$
$$= C_l(1-k)t_l + \alpha k C_l t_0 \qquad (5.1),$$

Where C_0 and t_0 are the concentration and thickness of the initial solution of auric ions before freezing, respectively; C_s is the concentration of auric ions trapped in the solid phase; C_l and t_l are the concentration and thickness of the thin liquid layer on the frozen solution of auric ions, respectively; k is the partition coefficient defined as the ratio of auric ion concentration that are trapped in the solid (C_s) to the concentration of the thin liquid layer on the frozen solution of auric ions (C_l); and α is the expansion coefficient when liquid water freezes to ice. The left side of the equation is the area density of the auric ions before freezing, while the right side represents a total area density of auric ions after freezing, with the first

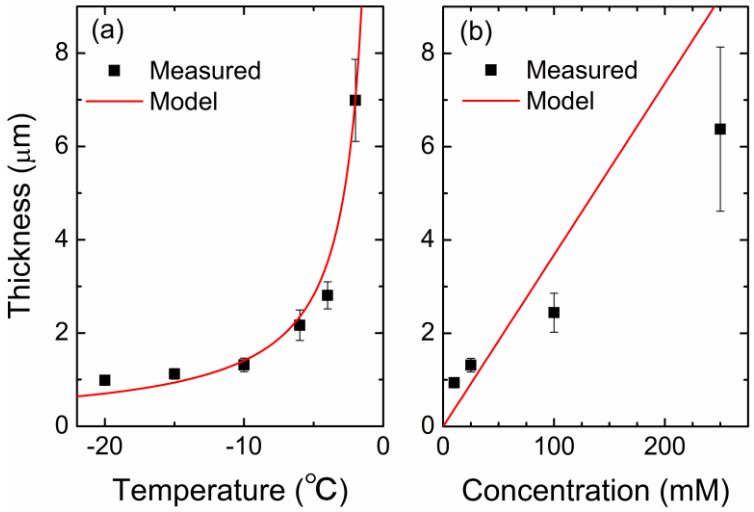

Figure 5.10 Variation in the AuNP film thickness with respect to the (a) temperature at the bottom side of the frozen solution with the 25 mM initial concentration of the solution of auric ions and (b) initial concentration of the solution of auric ions before freezing the bottom side of the solution at −10 °C. The black squares indicate the measured thickness of the AuNP film; the solid red lines indicate the numerical fittings calculated from Eq. (5.6) based on the mass balance model of the thin liquid layer on the ice body of the frozen solution.

term representing the area density of auric ions in the thin liquid layer on the frozen solution of auric ions and the second term representing the area density of auric ions trapped in the solid phase. From Eq. (5.1), t_l is expressed as follows,

$$t_l = \frac{(C_0 - \alpha k C_l)}{C_l(1-k)} t_0 \qquad (5.2).$$

The concentration of the thin liquid layer (C_l) is determined thermodynamically when the temperature of the frozen solution (T) is given in °C, as can be seen in a phase diagram of the aqueous solutions (Fig. 5.11). When the liquidus between the liquid phase and the ice and liquid phase is assumed as a linear curve, C_l can be expressed as a function of T as follows,

$$C_l = -bT \qquad (5.3),$$

where $-b$ is the slope of the liquid phase line. When T is changed with fixing C_0, t_l can be expressed as

$$t_l = \frac{C_0 t_0}{1-k}\frac{1}{C_l} - \frac{\alpha t_0}{\frac{1}{k}(1-k)} = -\frac{C_0 t_0}{b(1-k)}\frac{1}{T} - \frac{\alpha t_0}{\frac{1}{k}(1-k)} \approx -\frac{C_0 t_0}{b}\frac{1}{T} \quad (k << 1) \qquad (5.4).$$

On the other hand, when C_0 is changed with fixing T, t_l can be expressed as

$$t_l = \frac{t_0}{C_l(1-k)} C_0 - \frac{\alpha k C_l t_0}{C_l(1-k)} \approx \frac{t_0}{C_l} C_0 \quad (k << 1) \qquad (5.5).$$

Here, as can be seen in the phase diagram of binary system in Fig 5.11, it should be noted that the solid phase line is overlapped on the vertical axis at $C = 0$ because the partition coefficient in aqueous systems k is generally very low in the order of 10^{-3}–10^{-2} [182]. Therefore, the partition coefficient k was assumed to be very small in this calculation. From Eq. (5.4) and Eq. (5.5), the following relationships between t_l and T or t_l and C_0 can be derived,

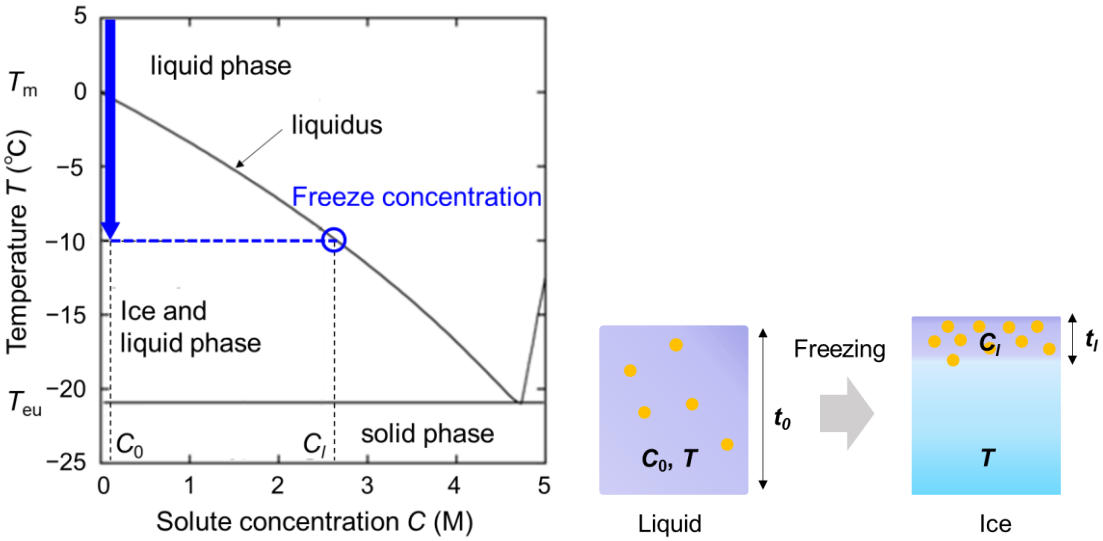

Figure 5.11 The phase diagram of aqueous KCl solution [44, 179], as a typical example of the aqueous solutions. The freeze concentration is easily understood by the phase diagram. When cooling the aqueous solutions with initial concentration (C_0) below the melting point of water (T_m), freeze concentration appeared at temperatures below the liquidus and above the eutectic point (T_{eu}), where the concentration of the liquid layer (C_l) is determined by the value on the liquidus.

$$t_l = \frac{C_0}{C_l} t_0 \propto -\frac{1}{T} \ (for\ fixed\ C_0)$$
$$\propto C_0 \ (for\ fixed\ T) \qquad (5.6)$$

Therefore, the thin liquid layer thickness (t_l) is proportional to the initial concentration of the solution of auric ions (C_0) or inversely proportional to the negative temperature of the frozen solution of auric ions ($-T$). The same temperature and concentration dependences were observed in terms of the thickness of AuNP films synthesized by PFT, although in the temperature dependence, we assumed the temperature differences in the frozen solution to be negligible compared with the range of interest. As shown in Fig. 5.10, the thickness of the AuNP film was inversely proportional to the negative temperature of the frozen solution at the bottom side (Fig. 5.10(a)) and directly proportional to the initial concentration of the solution of auric ions (Fig. 5.10(b)), both of which were guided by the inverse proportional and proportional fittings, respectively, based on the temperature and concentration dependences of the thin liquid layer. This result suggests that the thin liquid layer on the frozen solution of auric ions served as a plasma-assisted reaction field in the PFT method for the synthesis of AuNP films. In other words, PFT provided a thermodynamically size-tunable interfacial reaction field at the plasma–ice interface and can be controlled by temperature and solution concentration. This concept can significantly affect the design of micro- or nanoscale materials for energy conversion and storage, biosensors, biocompatible electronic device, etc.

5-2-4. Development of PFT with colloidal dispersion

One of the largest advantage of freezing phenomenon is self-assembling structure of ice accompanyed

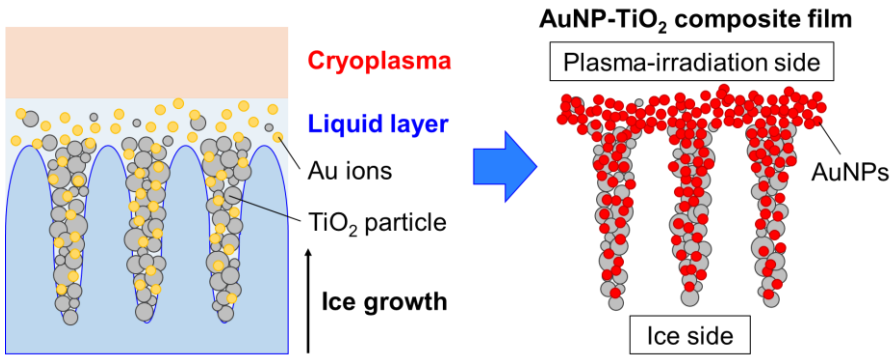

Figure 5.12 Temperature dependence of the arithmetic mean height of AuNP-TiO_2 thin film.

by freezing [47]. When colloidal dispersion is frozen, not only concentrated liquid phase but also lamellar structure of ice bulk are formed in the freezing direction. Recently, the self-assembling structure has been widely developed as a path to build complex composite materials, and the technique is termed as freeze casting [15, 48]. By superposing chemical reactions by plasma onto the lamellar structure by freezing, further development of a materials design method by PFT can be anticipated. Here, TiO_2 particles were added to the AuNP film synthesis by PFT, to demonstrate the concept as shown in Fig. 5.12.

Experimental setup and procedures are basically the same as the case of the synthesis of AuNP film by PFT as described above, instead of the addition of TiO_2 particles to the solution of auric ions. 20 mM auric ions solution including 1 vol% TiO_2 nanoparticles (anatase, 100 nm of average diameter, Wako chemical industries) was frozen in one direction from the bottom side, and cryoplasma jet was radiated onto the ice to synthesize AuNP-TiO_2 composite film. The synthesized film was washed by purified water for subsequent analysis.

Figure 5.13 shows SEM images of the AuNP-TiO_2 composite film synthesized by PFT at −5, −10, and −15 ℃ at the bottom side of frozen solution. Images of both plasma-irradiation side and ice side are displayed for each temperature. Basically, the film shows same morphology as the AuNP film synthesized by PFT, i.e. porous structure interconnected by nanoparticles. The noticeable difference is the deposition of

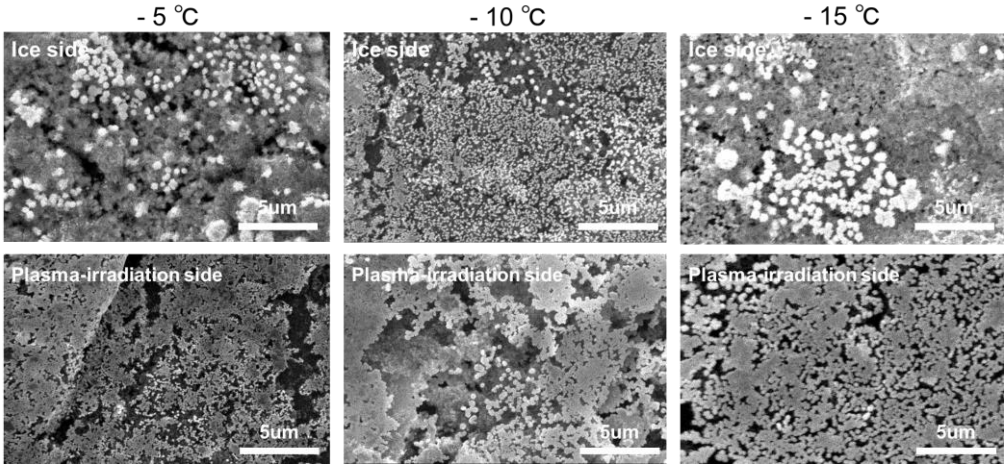

Figure 5.13 SEM images of AuNP-TiO_2 composite film. The top panel shows the ice side, whereas the bottom panel shows the plasma-irradiation side.

particles with approximately 1 μm diameter on the porous structure, observed only on the ice side, observed at all temperature conditions. This could be attributed to the self-assembling lamellar structure of ice due to the addition of TiO_2 particles. To further investigate this result, EDS spectrum, EDS mapping images, and Raman spectrum were obtained, as shown in Fig. 5.14. The film was composed of both AuNPs and TiO_2 particles as shown in EDS spectra. The inclusion of TiO_2 particles in the synthesized film was also evident from the Raman spectra, which shows the same spectra as anatase-type TiO_2. Furthermore, the AuNPs and TiO_2 particles were uniformly distributed in the AuNP-TiO_2 composite film, as shown in the EDS mapping images. Therefore, TiO_2 nanoparticles were considered to be incorporated into the composite film during the binding of AuNPs, resulting in the formation of the composite film.

To analyze the effect of TiO_2 to the composite film structure, the surface roughness of the AuNP-TiO_2 composite film was evaluated, by measuring the arithmetic mean height of the film with a confocal microscope. The arithmetic mean height is a parameter that represents surface roughness, expressed by the average of the absolute value of the difference in height of each point with respect to the average height of the surface. Fig. 5.15 shows the temperature dependence of the arithmetic mean height of the composite film on plasma-irradiation side and ice side, and that of AuNP film on the ice side. The surface roughness became larger by the addition of TiO_2 particles that has larger diameter than that of AuNP, when comparing the surface roughness of the composite film to that of AuNP film. Furthermore, when comparing the surface roughness of the composite film on each side, the surface roughness on the ice side was larger than that on the plasma-irradiation side, which cannot be explained only by the addition of TiO_2 particles. Although further investigation is necessary, one possible explanation is that the composite film might be synthesized along the self-assembling lamellar structure of the ice formed by the one-directional growth of the TiO_2 colloidal dispersion. This is a promising result for further development of PFT as a novel scheme of materials design, while the interpretation of the result remains speculation at present.

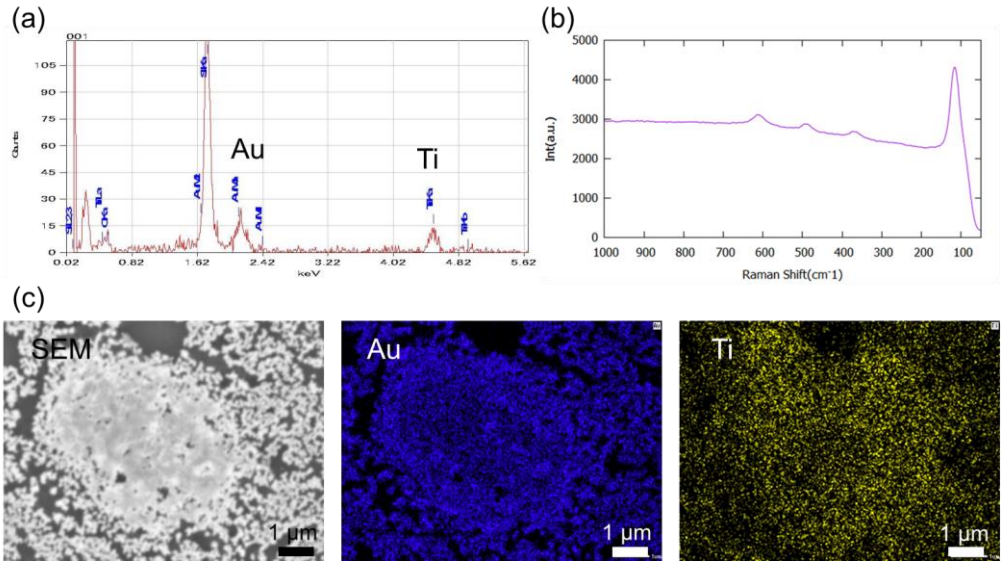

Figure 5.14 EDS and Raman measurements of the AuNP-TiO_2 composite film. (a) EDS spectrum, (b) Raman spectrum, and (c) EDS mapping images. All data were obtained for the ice side of the composite film.

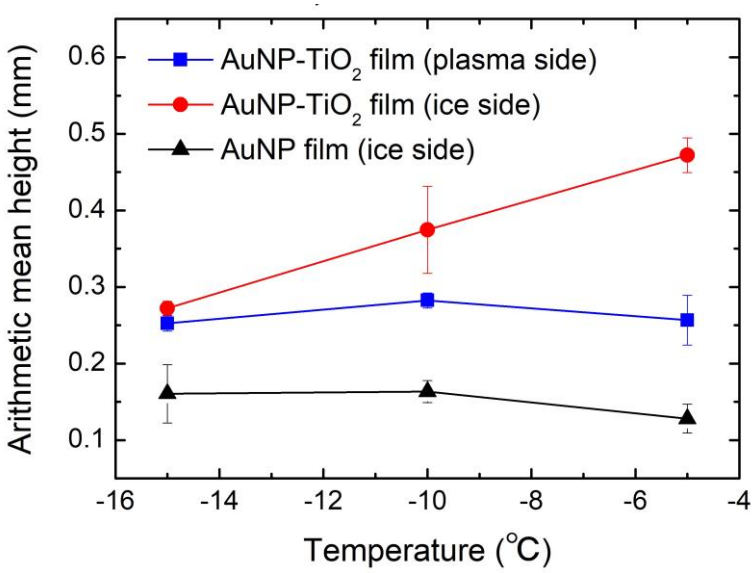

Figure 5.15 Temperature dependence of the arithmetic mean height of AuNP-TiO_2 thin film.

5-4. Summary

In this chapter, we proposed a PFT method for materials processing, in which a new type of interfacial reaction field was used, i.e., the plasma–ice interface. As an example of PFT for materials processing, self-standing AuNP films with porous structure were synthesized by PFT in which cryoplasma was irradiated onto the thin liquid layer formed on the ice body of the frozen solution of auric ions. PFT was revealed to inherently allow for a surfactant-free and area-selective processing for the synthesis of AuNP films; thus, PFT is an attractive method for the synthesis of nanostructured self-standing thin films. As a novel characteristics of PFT, simple tuning of the AuNP film thickness was demonstrated by changing the temperature of the frozen solution and the initial concentration of the solution of auric ions, exploiting the thickness control of the thin liquid layer at plasma-ice interface by thermodynamic parameters. In addition to the synthesis of the self-standing AuNP film, PFT is a concept that could be applied to design other types of materials such as functional self-standing thin films. For example, synthesis of Au-TiO_2 composite film which has nano- or micro-structure transferred by the self-assembling lamellar structure with freezing, was investigated in this chapter, while the interpretation of the result remains speculation at present. PFT is anticipated to be a novel plasma materials processing that can significantly affect material design, such as catalysts for energy conversion and storage, biosensors in the medical field, and biocompatible electronic devices.

Chapter.6 Conclusion

In this dissertation, generation and application of plasma-ice interfacial reaction field was studied to explore a novel cryogenic reaction field. Although reaction rates should be lower at lower temperatures, novel reaction field could be formed at plasma-ice interface, by the combination of the high reactivity of cryoplasma with the ice surface as a predominant chemical reaction field at low temperatures. The idea of the plasma-ice interfacial reaction field was initially motivated as a new approach for the investigation of chemical processes at cryogenic astrophysical environments, such as the synthesis of prebiotic organic molecules, because chemical reactions initiated by primary energetic radiation and secondary produced radials might be simulated by plasma-ice interfacial reaction field. I have also expected plasma-ice interfacial reaction field as a new approach for materials design, with using self-assembling structure by freezing of aqueous solution and colloidal dispersion. However, there has been no study on plasma-ice interfacial reaction field, as far as I know. Therefore, I had to establish generation of plasma-ice interfacial reaction field with a good controllability, as well as to investigate such attractive concepts. The most significant point of this study is continuous temperature control of plasma-ice interfacial reaction field at low and cryogenic temperatures, for both generation and application of it. Here, the continuous controllability of gas temperature in cryoplasma is advantageous to investigate plasma-ice interfacial reaction field.

Prior to the investigation of plasma-ice interface, at first, temperature dependence of gas phase chemical reactions in cryoplasma was studied by laser measurements. Near-infrared laser heterodyne interferometry enabled non-contact evaluation of the temporal variation of gas temperature in cryoplasma, and laser absorption spectroscopy allowed non-contact evaluation of the density and lifetime of metastable helium atoms. Based on these results, gas temperature dependence of the mechanism of quenching reactions of metastable helium atoms was revealed quantitatively, which was attributed to both the longer lifetime of metastable helium atoms at lower temperatures and the variation of the concentration of impurity species by the temperature change. The temperature dependence of reactions in cryoplasma could have a large influence on chemical reactions at plasma-ice interface, therefore temperature control is significant for the generation and application of plasma-ice interfacial reaction field.

Plasma-ice interfacial reaction field was generated with a good temperature control with using the H_2O-ice DBD configuration. H_2O-ice DBD was generated with a continuous temperature control below the melting point of water down to 6.5 K, by exploiting the gas temperature controllability of cryoplama. The temperature control of H_2O-ice DBD was confirmed by the same temperature dependence of its optical emission spectra and current-voltage characteristics as the previously established helium cryoplasma. The drastic change in power consumption of H_2O-ice DBD according to the solid-liquid phase transition around the melting point of water was observed, which was also an evidence of the good temperature controllability of H_2O-ice DBD. This is the first study on gas temperature-controlled generation of plasma coexistent with ice, with focusing on gas temperature as a control parameter. Through this, reproducible generation of plasma-ice interfacial reaction field with a continuous temperature control was established.

As for application of plasma-ice interfacial reaction field, two kinds of applications were explored in this dissertation. One is laboratory simulation of cryogenic astrophysical environments from the scientific point of view, while the other is the development of a novel technique for thin film fabrication in terms of engineering.

In the laboratory simulation of cryogenic astrophysical environments by plasma-ice interfacial reaction field, the purpose was to perform further precise experimental simulation of temperature environment of icy bodies in outer solar system. By 3% nitrogen-containing helium cryoplasma irradiation of CH_3OH/H_2O ice at 85 K, reddish coloration of the ice, which was similar to the color of the surface of some outer solar system objects, was observed. The peculiar point is that the reddish coloration was disappeared when heating to 120–150 K. The temperature dependence of the reddish coloration at cryogenic temperatures is distinct from previously reported reddish material produced by laboratory simulation experiments using non-equilibrium plasma, which is non-volatile organic compounds and stable even at room temperature. The temperature-responsive behavior of reddish coloration could add on a new explanation for the absence of ultra-red coloration closer to the Sun in the outer solar system; the cryogenic-specific reddish materials sublimate or convert to other colorless compounds at higher cryogenic temperatures, as an icy body travels from the Trans-Neptunian region to the inner solar system. Thus, our result implies that a reddish material specific to cryogenic environments might be a promising clue for the investigation of color diversity and formation mechanism of the outer solar system. Moreover, cryoplasma was expected as a novel modern technology for accelerating the investigation of chemistry and materials science in cryogenic space environments including the outer solar system.

In the development of a novel technique for thin film fabrication by plasma-ice interfacial reaction field, self-assembling structures formed by freezing at plasma-ice interface were exploited, and plasma-assisted freeze templating (PFT) was developed. When using aqueous solution, highly concentrated liquid layer on ice surface can be used as a nano- or micro-reactor enhanced by plasma. The advantage of the usage of the liquid layer as a reactor is its size tunability by thermodynamic parameters. The concept of PFT was experimentally demonstrated by the synthesis of AuNP film as the first example. On the other hand, when using colloidal dispersion, lamellar structure of ice can be used as a template for the synthesis of structural thin films. Although this has not been developed and evidenced fully, a promising result was obtained by the synthesis of AuNP-TiO_2 composite thin film. Thus, plasma-ice interface reaction field was revealed to be a unique and attractive approach for thin film synthesis and other materials design.

As described above, plasma-ice interfacial reaction field was generated, and was revealed to hold significant potentials for both scientific and engineering applications. Therefore, a platform of the new research area “plasma-ice interfacial reaction field” can be said to be established for its further development and applications. Although the promising applications of plasma-ice interfacial reaction field was developed, further studies are indispensable for the understanding of the reaction mechanism and additional advantageous properties, especially at the plasma-ice “interface”. I hope that the plasma-ice interfacial reaction field would contribute to enrich our lives, through the elucidation of the nature of natural phenomena and the development of innovative materials.

Bibliography

[1] V. M. Donnelly, and A. Kornblit, *J. Vac. Sci. Technol. A* **31** (2013) 050825.

[2] S. De Wolf, A. Descoeudres, Z. C. Holman, and C. Ballif, *Green* **2** (2012) 7.

[3] N. Liu, J. R. Dwyer, H. C. Stenbaek-Nielsen, and M. G. McHarg, *Nat. Commun.* **6** (2015) 7540.

[4] N. Liu, B. Kosar, S. Sadighi, J. R. Dwyer, and H. K. Rassoul. *Phys. Rev. Lett.* **109** (2012) 025002.

[5] M. C. Kelley, *The Earth's Ionosphere: Plasma Physics and Electrodynamics*, (Academic Press, Elsevier, 1989).

[6] A. V. Artemyev, V. Angelopoulos, and J. M. McTiernan, *JGR Space Phys.* **123** (2018) 9955.

[7] P. J. Bruggeman, F. Iza, and R. Brandenburg, *Plasma Sources Sci. Technol.* **26** (2017) 123002.

[8] P. J. Bruggeman *et al., Plasma Sources Sci. Technol.* **25** (2016) 053002.

[9] S. Stauss, H. Muneoka, K. Urabe, and K. Terashima, Phys. Plasmas **22** (2015) 057103.

[10] S. Stauss, H. Muneoka, and K. Terashima, *Plasma Sources Sci. Technol.* **27** (2018) 023003.

[11] Y. Noma, J. H. Choi, S. Stauss, T. Tomai, and K. Terashima, *Appl. Phys. Express* **1** (2008) 046001.

[12] D. Ishihara, Y. Noma, S. Stauss, M. Sai, T. Tomai, and K. Terashima, *Plasma Sources Sci. Technol.* **17** (2008) 035008.

[13] Y. Noma, J. H. Choi, T. Tomai, and K. Terashima, *Appl. Phys. Lett.* **93** (2008) 101503.

[14] M. J. Molina, T. L. Tso, L. T. Molina, and F. C. Y. Wang, *Science* **238** (1987) 1253.

[15] Q. Cheng, C. Huang, and A. P. Tomsia, *Adv. Mater.* **29** (2017) 1703155.

[16] A. Fridman, *Plasma Chemistry* (Cambridge University Press, New York, 2012).

[17] S. Lanier, I. Shkurenkov, I. V. Adamovich, and W. R. Lempert, *Plasma Sources Sci. Technol.* **24** (2015) 025005.

[18] T. Nozaki, Y. Miyazaki, Y. Unno, and K. Okazaki, *J. Phys. D: Appl. Phys.* **34** (2001) 3383.

[19] N. L. Aleksandrov, S. V. Kindysheva, M. M. Nudnova, and A. Y. Starikovskiy, *J. Phys. D: Appl. Phys.* **43** (2010) 255201.

[20] J. H. Choi, Y. Noma, T. Tomai, and K. Terashima, *Appl. Phys. Lett.* **93**, (2008) 081504.

[21] S. Stauss, H. Muneoka, N. Ebato, F. Oshima, D. Z. Pai, and K. Terashima, *Plasma Sources Sci. Technol.* **22**, (2013) 025021.

[22] E. Stoffels, A. J. Flikweert, W. W. Stoffels, and G. M. W. Kroesen, *Plasma Sources Sci. Technol.* **11** (2002) 383.

[23] E. Stoffels, Y. Sakiyama, and D. B. Graves, *IEEE Trans. Plasma Sci.* **36** (2008) 1441.

[24] R. Dussart, T. Tillocher, P. Lefaucheux, and M. Boufnichel, *J. Phys. D: Appl. Phys.* **47** (2014) 123001.

[25] F. Iacopi, J. H. Choi, K. Terashima, P. M. Rice, and G. Dubois, *Phys. Chem. Chem. Phys.* **13** (2011) 3634.

[26] S. Stauss, S. Mori, H. Muneoka, K. Terashima, and F. Iacopi, *J. Vac. Sci. Technol. B* **31** (2013) 061202.

[27] J. H. Choi, Y. Noma, and K. Terashima, *Plasma Sources Sci. Technol.* **18**, (2009) 025023.

[28] J. H. Choi, Y. Noma, M. Sano, and K. Terashima, *J. Phys. D: Appl. Phys.* **43**, (2010) 072001.

[29] H. Muneoka, K. Urabe, J. H. Choi, S. Stauss, and K. Terashima, *Plasma Sources Sci. Technol.* **23** (2014) 065038.

[30] K. Urabe, H. Muneoka. S. Stauss, O. Sakai, and K. Terashima, *Jpn. J. Appl. Phys.* **54** (2015) 106101.

[31] D. J. Burke, and W. A. Brown, *Phys. Chem. Chem. Phys.* **12** (2010) 5947.

[32] K. I. Oberg, *Chem Rev.* **116** (2016) 9631.

[33] H. Kang, *Acc. Chem. Res.* **38**, (2005) 893.

[34] K. Kuwahata, T. Hama, A. Kouchi, and N. Watanabe, *Phys. Rev. Lett.* **115** (2015) 133201.

[35] Y. Oba, N. Watanabe, Y. Osamura, and A. Kouchi, *Chem. Phys. Lett.* **634** (2014) 53.

[36] Y. Oba, N. Watanabe, T. Hama, K. Kuwahata, H. Hidaka, and A. Kouchi, *Astrophys. J.* **749** (2012) 67.

[37] M. P. Bernstein, J. P. Dworkin, S. A. Sandford, G. W. Cooper, and L. J. Allamandola, *Nature* **416** (2002) 401.

[38] G. M. M. Caro, U. J. Meierhenrich, W. A. Schutte, B. Barbier, A. A. Segovia, H. Rosenbauer, W. H. P. Thiemann, A. Brack, and J. M. Greenberg, Nature **416** (2002) 403.

[39] C. Meinert, I. Myrgorodska, P. de Marcellus, T. Buhse, L. Nahon, S. V. Hoffmann, L. L. S. d'Hendecourt, and U. J. Meierhenrich, *Science* **352** (2016) 208.

[40] Y. Oba, Y. Takano, H. Naraoka, N. Watanabe, and A. Kouchi, *Nat. Commun.* **10** (2019) 4413.

[41] Y. Li, and G. A. Somorjai, *J. Phys. Chem. C* **111** (2007) 9631.

[42] T. Bartels-Rausch *et al., Atmos. Chem. Phys.* **14** (2014) 1587.

[43] S. C. Park, E. -S. Moon, and H. Kang, *Phys. Chem. Chem. Phys.* **12** (2010) 12000.

[44] K. -H. Jung, S. -C. Park, J. -H. Kim, and H. Kang, *J. Chem. Phys.* **121** (2004) 2758.

[45] A. Inagawa, M. Harada, and T. Okada, *Sci. Rep.* **5** (2015) 17308.

[46] T. Okada, Chem. Rec. **17** (2017) 417.

[47] S. Deville, E. Maire, G. Bernard-Granger, A. Lasalle, A. Bogner, C. Gauthier, J. Leloup, and C. Guizard, *Nat. Mater.* **8** (2009) 966.

[48] S. Deville, E. Saiz, R. K. Nalla, and A. P. Tomsia, *Science* **311** (2006) 515.

[49] S. Deville, *Adv. Eng. Mater.* **10** (2008) 155.

[50] I. Y. Choi, J. Lee, H. Ahn, J. Lee, H. C. Choi, and M. J. Park, *Angew. Chem. Int. Ed.* **54** (2015) 10497.

[51] K. Kim, and M. J. Park, *Nanoscale* **12** (2020) 14320.

[52] O. Takai, *J. Photopolym. Sci. Technol.* **27** (2014) 379.

[53] P. Rumbach, D. M. Bartels, R. M. Sankaran, and D. B. Go, *Nat. Commun.* **6** (2015) 7248.

[54] Q. Chen, J. Li, and Y. Li, *J. Phys. D: Appl. Phys.* **48** (2015) 424005.

[55] J. Patel, L. Nemocova, P. Maguire, W. G. Graham, and D. Mariotti, *Nanotechnology* **24** (2013) 245604.

[56] N. Shirai, S. Uchida, and F. Tochikubo, *Japan Jpn. Appl. Phys.* **53** (2014) 046202.

[57] J. Hieda, N. Saito, and O. Takai, *J. Vac. Sci. Technol. A* **26** (2008) 854.

[58] S. -P. Cho, M. A. Bratescu, N. Saito, and O. Takai, *Nanotechnology* **22** (2011) 455701.

[59] T. Shirafuji, Y. Noguchi, T. Yamamoto, J. Hieda, N. Saito, O. Takai, A. Tsuchimoto, K. Nojima, and Y. Okabe, *Jpn. J. Appl. Phys.* **52** (2013) 125101.

[60] K. Inoue, T. Goto, M. Iida, T. Ito, Y. Shimizu, Y. Hakuta, and K. Terashima, *J. Phys. D: Appl. Phys.* **53** (2020) 42LT01.

[61] K. Takaki, *J. Plasma Fusion Res.* **90** (2014) 531.

[62] M. Sato, T. Ohgiyama, and J. S. Clements, *IEEE Trans. Ind. Appl.* **32** (1996) 106.

[63] G. Fridman, G. Friedman, A. Gutsol, A. B. Shekhter, V. N. Vasilets, and A. Fridman, *Plasma Process. Polym.*

5 (2008) 503.

[64] M. G. Kong, G. Kroesen, G. Morfill, T. Nosenko, T. Shimizu, J. V. Dijk, and J. L. Zimmermann, *New J. Phys.* **11** (2009) 115012.

[65] M. Shigeta, and A.B. Murphy, *J. Phys D: Appl. Phys.* **44** (2011) 174025.

[66] M. Tsumaki, Y. Shimizu, and T. Ito, *Mater. Lett.* **116** (2016) 81.

[67] M. Tsumaki, K. Nitta, S. Jeon, K. Terashima, and T. Ito, *J. Phys. D: Appl. Phys.* **51** (2018) 30LT01.

[68] E. F. van Dishoeck, in *Astrochemistry VII*: *Through the Cosmos from Galaxies to Planets*, eds. M. Cunningham et al., (Cambridge University Press, Cambridge, 2018) p.3.

[69] P. Ehrenfreund, and S. B. Charnley, *Annu. Rev. Astron. Astrophys.* **38** (2000) 427.

[70] E. Herbst, *Chem. Soc. Rev.* **30** (2001) 168.

[71] P. Bruston, M. Khlifi, Y. Benilan, and F. Raulin, *J. Geophys. Res. Planets* **99** (1994) 19047.

[72] M. L. Cable, S. H. Horst, R. Hodyss, P. M. Beauchamp, M. A. Smith, and P. A. Willis, *Chem. Rev.* **112** (2012) 1882.

[73] D. P. Cruikshank, in *From Stardust to Planetesimals*, eds. Y. J. Pendleton and A. Tielens, (Astronomical 380 Society of the Pacific, San Francisco, 1997) p. 315.

[74] H. Cottin, M. C. Gazeau, and F. Raulin, *Planet. Space Sci.* **47** (1999) 1141.

[75] C. J. Bennett, C. Pirim, and T. M. Orlando, *Chem. Rev.* **113** (2013) 9086.

[76] P. Coll, D. Coscia, M. C. Gazeau, E. de Vanssay, J. C. Guillemin, and F. Raulin, *Adv. Space Res.* **16** (1995) 93.

[77] T. W. Scattergood, *Adv. Space Res.* **7** (1987) 99.

[78] C. J. Bennett, S. -H. Chen, B. -J. Sun, A. H. H. Chang, and R. I. Kaiser, *Astrophys. J.* **660** (2007) 1588.

[79] C. S. Jamieson, A. M. Mebel, and R. I. Kaiser, *Astrophys. J. Sppul. Ser.* **163** (2006) 184.

[80] P. A. Gerakines, M. H. Moore, and R. L. Hudson, Icarus **170** (2004) 202.

[81] Y. Takano, T. Tsuboi, T. Kaneko, K. Kobayashi, and K. Marumo, *B. Chem. Soc. Jpn.* **77** (2004) 779.

[82] V. Mennella, G. A. Baratta, A. Esposito, G. Ferini, and Y. J. Pendleton, *Astrophys. J.* **587** (2003) 727.

[83] C. R. Arumainayagam, R. T. Garrod, M. C. Boyer, A. K. Hay, S. T. Bao, J. S. Campbell, J. Wang, C. M. Nowak, M. R. Arumainayagama, and P. J. Hodge, *Chem. Soc. Rev.* **48** (2019) 2293.

[84] K. K. Sullivan, M. D. Boamah, K. E. Shulenberger, S. Chapman, K. E. Atkinson, M. C. Boyer, and C. R. Arumainayagam, *Mon. Not. R. Astron. Soc.* **460** (2016) 664.

[85] M. C. Boyer, N. Rivas, A. A. Tran, C. A. Verish, and C. R. Arumainayagam, *Surf. Sci.* **652**, (2016) 26.

[86] C. Szopa, G. Cernogora, L. Boufendi, J. J. Correia, and P. Coll, *Planet. Space Sci.* **54** (2006) 394.

[87] Z. Martins et al., *Space Sci. Rev.* **209** (2017) 43.

[88] P. Coll, R. Navarro-Gonzalez, C. Szopa, O. Poch, S. I. Ramirez, D. Coscia, F. Raulin, M. Cabane, A. Buch, and G. Israel, *Planet. Space Sci.* **77** (2013) 91.

[89] I. C. F. Mueller-Wodarg, D. F. Strobel, J. I. Moses, J. H. Waie, J. Crovisier, R. V. Yelle, S. W. Bougher, and R. G. Roble, *Space Sci. Rev.* **139** (2008) 191.

[90] S. A. Stern *et al., Science* **350** (2015) aad1815.

[91] N. Fray, and B. Schmitt, *Planet. Space Sci.* **57** (2009) 2053.

[92] A. Mahjoub, N. Carrasco, P. -R. Dahoo, B. Fleury, T. Gautier, and G. Cernogora, *Plasma Process. Polym.* **11**

(2014) 409.

[93] O. Poch, P. Coll, A. Buch, S. I. Ramirez, and F. Raulin, *Planet. Space Sci.* **61** (2012) 114.

[94] S. I. Ramirez, P. Coll, A. Buch, C. Brasse, O. Poch, and F. Raulin, *Faraday Discuss.* **147** (2010) 419.

[95] G. D. McDonald, L. J.Whited, C. DeRuiter, B. N. Khare, A. Patnaik, and C. Sagan, *Icarus* **122** (1996) 107.

[96] K. Urabe, H. Muneoka, S. Stauss, and K. Terashima, *Appl. Phys. Express* **6** (2013) 126101.

[97] K. Urabe, H. Muneoka, S. Stauss, and K. Terashima, *Plasma Sources. Sci. Technol.* **23** (2014) 064007.

[98] B. N. Ganguly, W. R. Lempert, K. Akhtar, J. E. Scharer, F. Leipold, C.O. Laux, R. N. Zare, and A.P. Yalin, *Non-Equilibrium Air Plasmas at Atmospheric Pressure*, ed. K. H. Becker, U. Kogelschats, K. H. Schoenbach and R. J. Barker (IOP Publishing, Bristol, U. K., 2005).

[99] F. Leipold, R. H. Stark, A. E. Habachi, and K. H. Schoenbach, *J. Phys. D: Appl. Phys.* **33** (2000) 2268.

[100] J. Y. Choi, N. Takano, K. Urabe, and K. Tachibana, *Plasma Sources Sci. Technol.* **18** (2009) 035013.

[101] K. Urabe, O. Sakai, and K. Tachibana, *J. Phys. D: Appl. Phys.* **44** (2011) 115203.

[102] C. W. Allen, *Astrophysical Quantities* (The Athlon Press, London, 1973) Chap. 5, p. 92.

[103] E. Lemmon, M. McLinden, and D. Friend, *NIST Standard Reference Database 23: Reference Fluid Thermodynamic and Transport Properties–REFPROP* Version 9.0 (2012) National Institute of Standards and Technology, Standard Reference Data Program, Gaithersburf.

[104] A. Kramida, Y. Ralchenko, J. Reader, and NIST ASD Team, NIST Atomic Spectra Database (version 5.2, 2014), http://physics.nist.gov/asd.

[105] K. Urabe, T. Morita, K. Tachibana, and B. N. Ganguly, *J. Phys. D: Appl. Phys.* **43** (2010) 095201.

[106] R. K. Paul, *Rev. Sci. Instrum.* **78** (2007) 093701.

[107] A. Koymen, F. C. Tang, X. Zhao, F. B. Dunning, and G. K. Walters, *Chem. Phys. Lett.* **168** (1990) 405.

[108] K. Niemi, J. Waskoenig, N. Sadeghi, T. Gans, and D. O'Connell, *Plasma Sources Sci. Technol.* **20** (2011) 055005.

[109] Y. B. Golubovskii, V. A. Maiorov, J. Behnke, and J. F. Behnke, *J. Phys. D: Appl. Phys.* **36** (2003) 39.

[110] R. J. Vidmar, and K. R. Stalder, *Final Performance Report Prepared for Air Force Office of Scientific Research, Computations of the power to sustain plasma in air with relevance to aerospace technology*, (2004).

[111] J. S. Chang, R. M. Hobson, Y. Ichikawa, and T. Kaneda, *Atomic and Molecular Process in Ionized Gas* (Tokyo Denki University Press, Tokyo, 1982). [in Japanese]

[112] M. Peyrard, *Nanolinearity* **17** (2004) R1.

[113] D. Georlette, V. Blaise, T. Collins, S. D'Amico, E. Gratia, A. Hoyoux, J. C. Marx, G. Sonan, G. Feller and C. Gerday, *FEMS Microbiol. Rev.* **28** (2004) 25.

[114] P. J. Bruggeman, N. Sadeghi, D. C. Schram, and V. Linss, *Plasma Sources Sci. Technol.* **23** (2014) 023001.

[115] D. Mariotti, Y. Shimizu, T. Sasaki, and N. Koshizaki, *J. Appl. Phys.* **101** (2007) 013307.

[116] K. B. Chai, and P. M. Bellan, *Geog. Res. Lett.* **40** (2013) 6258.

[117] S. Shimizu, B. Klumov, T. Shimizu, H. Rothermel, O. Havnes, H. M. Thomas, and G. E. Morfill, *J. Geophys. Res.* **115** (2010) D18205.

[118] Y. Noma, J. H. Choi, H. Muneoka, and K. Terashima, *J. Appl. Phys.* **109**, (2011) 053303.

[119] F. Massines, and G. Gouda, *J. Phys. D: Appl. Phys.* **31** (1998) 3411.

[120] D. Z. Pai, S. Stauss, and K. Terashima, *Plasma Sources Sci. Technol.* **23** (2014) 025019.

[121] F. Massinses, N. Gherardi, N. Naude, and P. Segur, *Plasma Phys. Control. Fusion* **47** (2005) B577.

[122] I. Radu, R. Bartnikas, G. Czeremuszkin, and M. R. Wertheimer, *IEEE Trans. Plasma Sci.* **31** (2003) 411.

[123] R. Brandenburg, Z. Navratil, J. Jansky, P. St'ahel, D. Trunec, and H. E. Wagner, *J. Phys. D: Appl. Phys.* **42** (2009) 085208.

[124] D. Ishihara, Y. Noma, S. Stauss, M. Sai, T. Tomai, and K. Terashima, *Plasma Sources Sci. Technol.* **17** (2008) 035008.

[125] S. A. J. A. Amin, and J. Lucas, *J. Phys. D: Appl. Phys.* **20**, (1987) 1590.

[126] H. B. Milloy, and R. W. Crompton, *Phys. Rev. A* **15**, (1977) 1847.

[127] A. Fabbri, T. F. Chong, and O. Coussy, *Cold Reg. Sci. Technol.* **44** (2006) 52.

[128] V. I. Gaiduk, and D. S. F. Crothers, *J. Phys. Chem. A* **110** (2006) 9361.

[129] J. L. Aragones, L. G. MacDowell, and C. Vega, *J. Phys. Chem. A* **115** (2011) 5745.

[130] V. F. Petrenko, and I. A. Ryzhkin, *J. Phys. Chem. B* **101** (1997) 6285.

[131] X. M. Zhu, and M. G. Kong, *J. Appl. Phys.* **97** (2005) 083301.

[132] A. K. Srivastava, M. K. Garg, K. S. G. Prasad, V. Kumar, M. B. Chowdhuri, and R. Prakash, *IEEE Trans. Plasma Sci.* **35** (2007) 1135.

[133] Yu. B. Golubovskii, V. A. Maiorov, J. Behnke, and J. F. Behnke, *J. Phys. D: Appl. Phys.* **36** (2003) 39.

[134] D. C. Jewitt, *Astron. J.* **123** (2002) 1039.

[135] S. S. Sheppard, *Astron. J.* **139** (2010) 1394.

[136] H. A. Weaver *et al., Science* **351** (2016) aae0030.

[137] S. A. Stern *et al., Science* **364** (2019) eaaw9771.

[138] J. Luu, and D. Jewitt, *Astron. J.* **112** (1996) 2310.

[139] M. J. Duncan, and H. F. Levison, *Science* **276** (1997) 1670.

[140] S. Lowry, A. Fitzsimmons, P. Lamy, and P. Weissman, *Kuiper belt objects in the planetary region: The Jupiter-family comets.* In: A. Barucci, H. Boehnhardt, D. Cruikshank, A. Morbidelli (Eds.), *The solar system beyond Neptune.* Univ. of Arizona Press, Tucson (2008) pp. 397–410.

[141] D. P. Cruikshank *et al., Astrobio.* **19** (2019) 831.

[142] B. N. Khare, C. Sagan, H. Ogino, B. Nagy, C. Er, K. H. Schram, and E. T. Arakawa, *Icarus.* **68** (1986) 176.

[143] D. P. Cruikshank, H. Imanaka, and C. M. Dalle Ore, *Adv. Space Res.* **36** (2005) 178–183.

[144] H. Imanaka, B. N. Khare, J. E. Elsila, E. L. O. Bakes, C. P. McKay, D. P. Cruiksank, S. Sugita, T. Matsui, and R. N. Zare, *Icarus* **168** (2004) 344–366.

[145] C. K. Materese, D. P. Cruikshank, S. A. Sandford, H. Imanaka, and M. Nuevo, *Astrophys. J.* **812** (2015) 150.

[146] C. K. Materese, D. P. Cruikshank, S. A. Sandford, H. Imanaka, M. Nuevo, and D. W. White, *Astrophys. J.* **788** (2014) 111.

[147] W. M. Grundy, *Icarus.* **199** (2009) 560.

[148] M. E. Brown, E. L. Schaller, and W. C. Fraser, *Astrophys. J. Lett.* **739** (2011) L60.

[149] D. Jewitt, *Astron. J.* **150** (2002) 201.

[150] C. M. Dalle Ore *et al., Astron. Astrophys.* **533** (2011) A98.

[151] W. R. Thompson, T. J. Henry, J. M. Schwartz, B. N. Khare, and C. Sagan, *Icarus.* **90** (1991) 57.

[152] R. Brunetto, M. A. Barucci, E. Dotto, and G. Strazzulla, *Astrophys. J.* **644** (2006) 646.

[153] F. Bagenal *et al., Science* **351** (2016) aad9045.

[154] J. F. Cooper, E. R. Christian, J. D. Richardson, and C. Wang, *Proton Irradiation of Centaur, Kuiper Belt, and Oort Cloud Objects at Plasma to Cosmic Ray Energy.* In: *The First Decadal Review of the Edgeworth-Kuiper Belt*, Springer, (2004) pp. 261–277.

[155] W. M. Grundy *et al., Icarus* **314** (2018) 232.

[156] J. S. Lewis, *Space Sci. Rev.* **14** (1973) 401.

[157] D. G. Gilmore, *Spacecraft Thermal Control Handbook, Volume I: Fundamental Technologies* 2nd ed. (California: The Aerospace Press, 2002) p.50.

[158] C. M. Dalle Ore, M. A. Barucci, J. P. Emery, D. P. Cruikshank, C. de Bergh, T. L. Roush, D. Perna, F. Merlin, and L. V. Dalle Ore, *Icarus* **252** (2015) 311.

[159] M. D. Boamah, K. K. Sullivan, K. E. Shulenberger, C. M. Soe, L. M. Jacob, F. C. Yhee, K. E. Atkinson, M. C. Boyer, D. R. Hainesa, and C. R. Arumainayagam, *Faraday Discuss.* **168** (2014) 249.

[160] S. Esmaili, A. D. Bass, P. Cloutier, L. Sanche, and M. A. Huels, *J. Chem. Phys.* **148** (2018) 164702.

[161] G. A. Miller and D. K. Carpenter, *J. Chem. Eng. Data* **9** (1964) 371.

[162] N Fray, and B Schmitt, *Planet. Space Sci.* **57** (2009) 2053.

[163] C. Meinert, I. Myrgorodska, P. Marcellus, T. Buhse, L. Nahon, S. V. Hoffmann, L. L. S. d'Hendecourt, and U. J. Meierhenrich, *Science* **352** (2016) 208.

[164] N. Peixinho, A. Doressoundiram, A. Delsanti, H. Boehnhardt, M. A. Barucci, and I. Belskaya, *Astron. Astrophys.* **410** (2003) L29.

[165] R. Duffard, N. Pinilla-Alonso, P. Santos-Sanz, E. Vilenius, J. L. Ortiz, T. Mueller, S. Fornasier, E. Lellouch, M. Mommert, A. Pal, C. Kiss, M. Mueller, J. Stansberry, A. Delsanti, N. Peixinho, and D. Trilling, Astron. Astrophys. **564** (2014) A92.

[166] J. Biener, M. M. Biener, R. J. Madix, and C. M. Friend, *ACS Catal.* **5** (2015) 6263.

[167] Y. Xia, X. Deng, S. Yan, C. Gao, C. Ma, and L. Jin, *Dalton. Trans.* 44 (2015) 11929.

[168] M. M. Biener, J. Biener, A. Wichmann, A. Wittstock, T. F. Baumann, M. Baumer, and A. V. Hamza, *Nano Lett.* **11** (2011) 3085.

[169] H. Min, J. Zhou, X. Bai, L. Li, K. Zhang, T. Wang, X. Zhang, Y. Li, Y. Jiao, X. Qi, and Y. Fu, *Langmuir* **33** (2017) 6732.

[170] Z. Matharu, P. Daggumati, L. Wang, T. S. Dorofeeva, Z. Li, and E. Seker, *ACS Appl. Mater. Interfaces* **9** (2017) 12959.

[171] P. Daggumati, Z. Matharu, and E. Seker, *Anal. Chem.* **87** (2015) 8149.

[172] M. U. -B. Christiansen, N. Seselj, C. Engelbrekt, M. Wagner, F. N. Stappen, and J. Zhang, *J. Mater. Chem. A* **6** (2018) 556.

[173] Z. Qi, and J. Weissmuller, *ACS Nano* **7** (2013) 5948.

[174] M. D. Ho, Y. Liu, D. Dong, Y. Zhao, and W. Cheng, *Nano Lett.* **18** (2018) 3593.

[175] R. Gopalakrishnan, E. Kawamura, A. J. Lichtenberg, M. A. Lieberman, and D. B. Graves, *J. Phys. D: Appl. Phys.* **49** (2016) 295205.

[176] M. Kim, G. H. Jeong, K. Y. Lee, K. Kwon, and S. W. Han, *J. Mater. Chem.* **18** (2008) 2208.

[177] P. Meakin, *Phys. Rev. Lett.* **51** (1983) 1119.

[178] B. Viswanath, S. Patra, N. Munichandraiah, and N. Ravishankar, *Langmuir* **25** (2009) 3115.

[179] R. R Cohen-Adad, and J. W. Lorimer, Eds., *Alkali Metal and Ammonium Chlorides in Water and Heavy Water (Binary Systems),* IUPAC Solubility Data Series, Pergamon **47** (1991) p225.

[180] T. Fujita, P. Guan, K. McKenna, X. Lang, A. Hirata, L. Zhang, T. Tokunaga, S. Arai, Y. Yamamoto, N. Tanaka, Y. Ishikawa, N. Asao, Y. Yamamoto, J. Erlebacher, and M. Chen, *Nat. Mater.* **11** (2012) 775.

[181] D. Walsh, L. Arcelli, T. Ikoma, J. Tanaka, and S. Mann, *Nat. Mater.* **2** (2003) 386.

[182] R. G. Seidensticker, *J. Chem. Phys.* **56** (1972) 2853.

Acknowledgements

本博士論文研究は、東京大学新領域創成科学研究科物質系専攻の寺嶋・伊藤研究室にて行われました。本研究の遂行にあたり、多くの方々にお世話になるとともに、多大なるご指導とご協力を賜りました。この場を借りて感謝申し上げます。

寺嶋和夫教授には、学部 4 年生の研究室配属時から現在に至るまで、研究室の指導教員として長期に渡り研究の全てにおいてご指導いただきました。実際の研究・実験の進め方に加え、研究の計画・構築方法についても特にご指導いただいたとともに、いかなる（従来は本研究室は分野外であった）アイデアに対しても研究の遂行を快諾していただけたことに、大変感謝しております。改めて感謝申し上げます。

伊藤剛仁准教授には、博士課程進学後を中心に、研究室の指導教員として、研究全般において細部に渡ってご指導いただきました。伊藤先生のご指導なしにはどの投稿論文も完成しませんでした。

本博士論文の審査にあたり、複雑理工学専攻の吉川一朗教授、先端エネルギー工学専攻の小野亮教授、物質系専攻の内藤昌信准教授、産業技術総合研究所分析計測標準研究部門の三浦永祐上級主任研究員には、大変お世話になりました。大変有意義なご指導をいただき、本論文の質を格段に向上させることができました。

滋賀県立大学の酒井道教授には、レーザー診断計測を中心にご指導いただくと同時に、学会においても大変お世話になりました。

研究室 OB の占部継一郎博士、宗岡均博士、松林康仁博士、安井涼馬さんには、クライオプラズマを中心に研究の計画、遂行、解析、論文執筆等の全般に渡ってご指導いただきました。

研究室 OB の岩瀬謙吾さん、研究室メンバーの Phua Yu Yu さん、小池健さんには、プラズマ／氷界面反応場の応用の研究遂行において大変お世話になりました。

研究室秘書の伊藤希和さんには、事務手続きやその他様々なことに関して大変お世話になりました。伊藤希和さんのご協力なしには本博士論文は完成しませんでした。

現研究室メンバーの後藤拓博士には、博士課程学生の先輩として、研究の相談から雑談に至るまで研究生活の全てにおいて頼りにさせていただきました。後藤さんのおかげで快適な研究生活を送れました。

関わってきた全ての研究室 OB 及び研究室メンバーに、研究生活において大変お世話になりました。

サークルの同期・後輩の大出千恵氏、森田峻平氏には、私が専門知識を全く持ち合わせていなかった化学に関する実験結果の解釈において、多くの相談・議論をさせていただきました。そのおかげで自信をもって研究を進めることができました。

博士課程進学という普通でない道に対し、最初は反対もありましたが、最終的には理解して応援してくれた両親と今は亡き愛猫に感謝いたします。

また、本研究の一部は日本学術振興会、特別研究員 DC2 として遂行いたしました。

Achievements

Publication

1. Yu Yu Phua, Noritaka Sakakibara, Tsuyohito Ito, and Kazuo Terashima, "Low temperature plasma for astrochemistry: toward a further understanding with continuous and precise temperature control", *Plasma and Fusion Research*, in press.
2. Noritaka Sakakibara, Yu Yu Phua, Tsuyohito Ito, and Kazuo Terashima, "Cryogenic-specific reddish coloration by cryoplasma: New explanation for color diversity of outer solar system objects", *The Astrophysical Journal Letters* **891** (2020) L44. [Press release from the University of Tokyo]
3. Kenichi Inoue, Shion Takahashi, Noritaka Sakakibara, Susumu Toko, Tsuyohito Ito, and Kazuo Terashima, "Spatiotemporal optical emission spectroscopy to estimate electron density and temperature of plasmas in solution", *Journal of Physics D: Applied Physics* **53** (2020) 235202.
4. Noritaka Sakakibara, Tsuyohito Ito, and Kazuo Terashima, "Plasma-ice interface as thermodynamically size-tunable reaction field: development of plasma-assisted freeze templating", *Langmuir* **35** (2019) 3013–3019.
5. Noritaka Sakakibara, Yasuhito Matsubayashi, Tsuyohito Ito, and Kazuo Terashima, "Formation of pseudo-microgravity environment for dusty plasmas in supercritical carbon dioxide", *Physics of Plasmas* **25** (2018) 010704.
6. Noritaka Sakakibara, and Kazuo Terashima, "Generation of H_2O-ice dielectric barrier discharge for the development of novel cryogenic reaction fields", *Journal of Physics D: Applied Physics* **50** (2017) 22LT01.
7. Noritaka Sakakibara, Hitoshi Muneoka, Keiichiro Urabe, Ryoma Yasui, Osamu Sakai, and Kazuo Terashima, "Laser diagnostics on atmospheric pressure discharge plasmas, including cryoplasmas, in environments around room and cryogenic temperature", *Journal of Physics D: Applied Physics* **50** (2017) 165201.

Chapter

1. Yasuhito Matsubayashi, Noritaka Sakakibara, Tsuyohito Ito, and Kazuo Terashima, "Dusty plasmas in supercritical carbon dioxide", *Progress in Fine Particle Plasmas*, ISBN: 978-1-83880-471-8, DOI: 10.5772/intechopen.88768 (2019 年 8 月).
2. 榊原教貴, 伊藤剛仁, 寺嶋和夫 "マルチフェーズプラズマ反応場－革新的な材料プロセス創製に向けて－（Multiphase Plasma Reaction Field: Toward Innovative Materials Processing）", プラズマ・核融合学会誌 Vol.94, No.9 (2018) 441-448.

International conference

1. ○Noritaka Sakakibara, Yu Yu Phua, Tsuyohito Ito, Kazuo Terashima, “Laboratory demonstration of cryogenic-specific reddish coloration with cryoplasma”, JpGU-AGU Joint Meeting 2020, PPS01-P10, Virtual Meeting, Japan, Jul. 12–16, 2020 [Poster].
2. ○Noritaka Sakakibara, Tsuyohito Ito, and Kazuo Terashima, “Size control of plasma-activated liquid layer on ice surface by thermodynamic parameters”, 72nd Annual Gaseous Electronics Conference, LW3.00002, College Station, TX, USA, Oct.28-Nov.1, 2019 [Oral] [selected as Student Excellent Award Finalist]
3. ○Noritaka Sakakibara, Yasuhito Matsubayashi, Tsuyohito Ito, and Kazuo Terashima, “Effect of buoyancy on dusty plasmas in high-density carbon dioxide”, XXXIV ICPIG & ICRP-10, PO18PM-048, Sapporo, Japan, July 14-19, 2019 [Poster] [received “Student Poster Prize”]
4. ○Noritaka Sakakibara, Makoto Tanaka, Hiroyuki Toyokawa, Tsuyohito Ito, Kazuo Terashima, Yukiya Hakuta, Eisuke Miura, “Time-resolved observation of femtosecond laser-induced plasmas in water”, 10th International Workshop on Microplasmas, O-38, Kyoto, Japan, May 20-24, 2019 [Oral]
5. ○Noritaka Sakakibara, Tsuyohito Ito, and Kazuo Terashima, “Nanoporous gold thin film synthesis by plasma-assisted freeze templating: irradiation of cryoplasma onto frozen solution”, 71nd Annual Gaseous Electronics Conference, QR4.00010, Portland, OR, USA, November 5-9, 2018 [Oral]
6. Kazuo Terashima, ○Noritaka Sakakibara, and Tsuyohito Ito, “Plasma in cryogenic conditions”, 2018 Asia-Pacific Conference on Plasma and Terahertz Science, I-11, Xi’an, China, August 15-18, 2018 [Oral][invited]
7. ○Noritaka Sakakibara, Tsuyohito Ito, and Kazuo Terashima, “Development of ice dielectric barrier discharge for the novel reaction field in cryogenic environments”, 70th Annual Gaseous Electronics Conference, RR2.00001, Pittsburgh, PA, USA, November 6-10, 2017 [Oral]
8. ○Noritaka Sakakibara, and Kazuo Terashima, “Generation of H_2O ice dielectric barrier discharge as a promising unique reaction field at cryogenic environments”, ISPlasma 2017 / IC-PLANTS 2017, 03aB02O, Aichi, Japan, March 1-5, 2017 [Oral] [received ‘Best Presentation Award’]
9. ○Noritaka Sakakibara, Hitoshi Munoeka, Keiichiro Urabe, Ryoma Yasui, and Kazuo Terashima, “Laser diagnostics on atmospheric-pressure low-temperature helium pulsed plasmas in room- and cryogenic- temperature environments”, 68th Annual Gaseous Electronics Conference/9th International Conference on Reactive Plasmas/33rd Symposium on Plasma Processing, LW1.00066, Honolulu, USA, October 12-16, 2015 [Poster]

Domestic conference

1. ○榊原教貴, ポアユーユー, 伊藤剛仁, 寺嶋和夫,「クライオプラズマにより生成した天文関連赤色物質がもたらす、外太陽系氷天体に見られる色分布への説明可能性」, 第 81 回応用物理学会秋季学術講演会, 11p-Z05-2, オンライン開催, 2020 年 9 月 8 日－11 日（口頭発表）[注目講演に選出] [発表予定]
2. ○榊原教貴, ポアユーユー, 伊藤剛仁, 寺嶋和夫,「クライオプラズマによる極低温環境に特有な赤色物質の生成（I）：プラズマ宇宙物質科学への展開」, 第 67 回応用物理学会春季学術講

演会, 15p-A304-3, 上智大学四谷キャンパス, 2020 年 3 月 12 日－15 日（口頭発表）[コロナウイルスにより中止]

3. ○榊原教貴, 伊藤剛仁, 寺嶋和夫, 伯田幸也, 三浦永祐,「フェムト秒レーザー誘起液中生成プラズマに伴う水和電子の生成、消滅挙動」, 第 67 回応用物理学会春季学術講演会, 12p-A302-1, 上智大学四谷キャンパス, 2020 年 3 月 12 日－15 日（口頭発表）[講演奨励賞受賞記念講演][コロナウイルスにより中止]
4. ○榊原教貴, 伊藤剛仁, 寺嶋和夫, 伯田幸也, 三浦永祐,「フェムト秒レーザー誘起液中プラズマ反応場における水和電子生成、消滅挙動の時空間分解計測」, 第 80 回応用物理学会秋季学術講演会, 20a-B11-8, 北大札幌キャンパス, 2019 年 9 月 18 日－21 日（口頭発表）[注目講演に選出][講演奨励賞を受賞]
5. ○榊原教貴, 伊藤剛仁, 寺嶋和夫, 「プラズマー氷界面を用いたプラズマ支援テンプレート法の開発」, 第 66 回応用物理学会春季学術講演会, 11p-W323-6, 東工大大岡山キャンパス, 2019 年 3 月 9 日－12 日（口頭発表）
6. ○榊原教貴, 高橋史音, 井上健一, 後藤拓, 伊藤剛仁, 赤田圭史, 宮脇淳, 原田慈久, 伯田幸也, 寺嶋和夫, 「プラズマ改質カーボンナノチューブ分散溶液の軟 X 線分光測定（Soft X-ray Spectroscopy of Plasma-treated Carbon Nanotubes Dispersed in Solution）」, 第 28 回日本 MRS 年次大会, C3-O19-006, 北九州国際会議場, 2018 年 12 月 18 日-20 日（口頭発表）[奨励賞を受賞]
7. ○榊原教貴, 伊藤剛仁, 寺嶋和夫, 「凍結溶液表面へのクライオプラズマジェット照射による金属配線の創製」, 第 65 回応用物理学会春季学術講演会, 17p-C201-19, 早稲田, 2018 年 3 月 17 日－20 日（口頭発表）
8. ○榊原教貴, 松林康仁, 寺嶋和夫, 「超臨界流体を用いた擬似微小重力環境ダストプラズマの創製（Ⅱ）」, 第 64 回応用物理学会春季学術講演会, 17p-313-14, 横浜, 2017 年 3 月 14 日-17 日（口頭発表）
9. ○Noritaka Sakakibara, Monica Morales Masis, Mihai Gabureac, Christophe Ballif, and Thomas Nelis “Plasma Treatment of TCO with the objective to modify the electrical conductivity”, ALPS Day 5th edition, No. 12, Burgdorf, Switzerland, January 2017 [Oral]
10. ○榊原教貴, 宗岡均, 占部継一郎, 安井涼馬, 寺嶋和夫, 「室温・氷点下における大気圧ヘリウムパルス放電プラズマのレーザー診断」, 第 76 回応用物理学会秋季学術講演会, 15p-2V-18, 名古屋, 2015 年 9 月 13 日-16 日（口頭発表）

Awards

1. 第 47 回（2019 年秋期）応用物理学会「講演奨励賞」　2019 年 12 月
2. XXXIV ICPIG & ICRP-10 Student Poster Prize　2019 年 7 月
3. 第 28 回日本 MRS 年次大会 奨励賞,　2018 年 12 月
4. ISPlasma 2017 / IC-PLANTS 2017　“Best Presentation Award”,　2017 年 3 月
5. 第 23 回日本金属学会・日本鉄鋼協会奨学賞（東京大学工学部マテリアル工学科学修最優秀）, 2015 年 3 月

Others

1. プレスリリース(東京大学),「極寒でしか存在できない赤色が外太陽系氷天体の謎を紐解く」 2020 年 3 月 17 日
2. 新聞報道, 日本経済新聞電子版「東大、クライオプラズマを氷表面に照射することで外太陽系に存在する氷天体と類似した赤色を呈することを発見」 2020 年 3 月 17 日
3. 記事掲載, 天文情報ポータルサイト AstroArts「極寒でのみ存在する赤色が解き明かす外太陽系氷天体の謎」 2020 年 3 月 23 日